MODELING TRANSIENTS AND DESIGNING A PASSIVE SAFETY SYSTEM FOR A NUCLEAR THERMAL ROCKET USING RELAP5

A Dissertation
Presented in Partial Fulfillment of the Requirements for the
Degree of Doctor of Philosophy
with a
Major in Nuclear Engineering
in the
College of Graduate Studies
University of Idaho
by

Jivan Khatry

Major Professor: Fatih Aydogan, Ph.D.

Committee Members: Richard Christensen, Ph.D.; Fred Gunnerson, Ph.D.; Stephen Herring, Ph.D.;

Department Administrator: Richard Christensen, Ph.D.

August 2017

AUTHORIZATION TO SUBMIT DISSERTATION

This dissertation of Jivan Khatry, submitted for the degree of Doctor of Philosophy with a Major in Nuclear Engineering and titled "MODELING TRANSIENTS AND DESIGNING A PASSIVE SAFETY SYSTEM FOR A NUCLEAR THERMAL ROCKET USING RELAP5," has been reviewed in final form. Permission, as indicated by the signatures and dates below, is now granted to submit final copies to the College of Graduate Studies for approval.

Major Professor: _____ Date: _____
Fatih Aydogan, Ph.D.

Committee Members: _____ Date: _____
Richard Christensen, Ph.D.

_____ Date: _____
Fred Gunnerson, Ph.D.

_____ Date: _____
Stephen Herring, Ph.D.

Department Administrator: _____ Date: _____
Richard Christensen, Ph. D.

ABSTRACT

Long-term high payload missions necessitate the need for nuclear space propulsion. Several nuclear reactor types were investigated by the Nuclear Engine for Rocket Vehicle Application (NERVA) program of National Aeronautics and Space Administration (NASA). Study of planned/unplanned transients on nuclear thermal rockets is important due to the need for long-term missions. A NERVA design known as the Pewee I was selected for this purpose. The following transients were run: (i) modeling of corrosion-induced blockages on the peripheral fuel element coolant channels and their impact on radiation heat transfer in the core, and (ii) modeling of loss-of-flow-accidents (LOFAs) and their impact on radiation heat transfer in the core. For part (i), the radiation heat transfer rate of blocked channels increases while their neighbors' decreases. For part (ii), the core radiation heat transfer rate increases while the flow rate through the rocket system is decreased. However, the radiation heat transfer decreased while there was a complete LOFA. In this situation, the peripheral fuel element coolant channels handle the majority of the radiation heat transfer. Recognizing the LOFA as the most severe design basis accident, a passive safety system was designed in order to respond to such a transient. This design utilizes the already existing tie rod tubes and connects them to a radiator in a closed loop. Hence, this is basically a secondary loop. The size of the core is unchanged. During normal steady-state operation, this secondary loop keeps the moderator cool. Results show that the safety system is able to remove the decay heat and prevent the fuel elements from melting, in response to a LOFA and subsequent SCRAM.

ACKNOWLEDGEMENTS

I would like to thank Dr Fatih Aydogan for his advice and support during this research. This work was funded by the NASA Idaho EPSCOR grant. I would like to thank Dr Richard Christensen for offering me a research assistantship position during the 2016-2017 school year. In addition, thanks to the Center for Space Nuclear Research (CSNR) of the Universities Space Research Association (USRA), based in Idaho Falls, for providing helpful documentation concerning the Pewee I Test Reactor. Thanks to Dr Stephen Herring of CSNR for offering me a research fellowship during Summer 2016. Thanks to Dr Steven Aumeier, former director of the Center for Advanced Energy Studies, for offering me a scholarship to attend the Modeling, Experimentation, and Validation Summer School at the Argonne National Laboratory. I give thanks to Dr Muhammad Ilyas, professor of nuclear engineering at the Pakistan Institute of Engineering and Applied Sciences (PIEAS), for sharing his RELAP5 expertise with me. I worked with Dr Ilyas for a year when he arrived at University of Idaho as a visiting professor/researcher. He and Dr Aydogan guided me in defining my dissertation topic. Although no longer associated with my graduate school career, thanks to my former advisor, Dr Akira Tokuhiro, for getting me started in the PhD program at University of Idaho. I thank Dr Tokuhiro for the initial projects he had me work on and for offering me research/teaching assistantships along the way.

DEDICATION

I would like to dedicate this to my parents and extended family back home, whose prayers and well wishes have kept me going. I appreciate their patience as they have had to cope with my absence throughout this journey. In addition, I also dedicate this to my paternal relatives based in the United States, and thank them for their love and support, which has encouraged me to work on my PhD.

TABLE OF CONTENTS

LIST OF FIGURES

LIST OF TABLES

LIST OF ABBREVIATIONS

ACRONYMS

Parameter	Explanation
BM-PeBR	Bimodal Pellet Bed Reactor
CBC	Closed Brayton Cycle
FSOR	Flexible Solar Optical Reflector
HCC	Hot Coolant Channels
HS	RELAP Heat Structure
HV	RELAP Hydrodynamic Volume
HTSA	Heat Transfer Surface Area
ISNPS	Institute for Space Nuclear Power Studies
ICC	Inner Coolant Channels
MLI	Multilayer Insulation
NASA	National Aeronautics and Space Administration
ND	Not Dated
NERVA	Nuclear Engine Rocket Vehicle Application
NTR	Nuclear Thermal Rocket
PeBR	Pellet Bed Reactor
PCC	Peripheral Coolant Channels
PVA	Photovoltaic Array
RELAP	Reactor Excursion Leak Analysis Program
SCDAP	Severe Core Damage Analysis Program
SOFI	Spray-On Foam Insulation
Stdy-st	Steady-state problem type declaration in RELAP
TDJ	Time Dependent Junction
TDV	Time Dependent Volume
TREAT	Transient Reactor Test Facility
VCHP	Variable Conductance Heat Pipe
WANL	Westinghouse Astronuclear Laboratory
ZBO	Zero-Boiloff

SYMBOLS

Parameter	Explanation
a	speed of sound
A	area of coolant channel's graphite or ZrC/NbC coating
A_{out}	flow area of the nozzle exit
α_d	payload ratio of rocket

A_t	flow area of the nozzle throat
β_s	structural ratio of rocket
c_p	specific heat capacity of fluid at constant pressure
c_v	specific heat capacity of fluid at constant volume
ΔP_{acc}	pressure loss due to acceleration
ΔP_{form}	pressure loss due to pipe form
ΔP_{fric}	pressure loss due to friction
ΔP_{total}	total pressure loss
Δu	change in rocket velocity
D_h	hydraulic diameter of the pipe
E	activation energy
ε	emissivity
f	friction factor
F	area factor
FeO	iron(II) oxide
Fe_2O_3	iron(III) oxide
θ_1	incident angle of air in Figure 3.1
θ_2	incident angle of oxide in Figure 3.1
θ_3	incident angle of metal in Figure 3.1
F_{th}	rocket thrust
g	acceleration due to gravity
γ	ratio of specific heats
h	oxide film thickness in Figure 3.1
Isp	specific impulse
Isp_{chem}	specific impulse of chemical rocket
Isp_{nuke}	specific impulse of nuclear rocket
J	radiosity
K	reaction rate
K_{cont}	contraction coefficient of nozzle
L	length of the pipe
λ	wavelength
m_d	payload mass of rocket
$\dot{m}$	mass flow rate of propellant

m_e	empty mass of rocket
M_e	Mach number of fluid
m_f	full mass of rocket
M_{molar}	molar mass
m_p	propellant mass of rocket
MR	propellant mass ratio
MR_{chem}	propellant mass ratio of chemical rocket
MR_{nuke}	propellant mass ratio of nuclear rocket
m_s	structural mass of rocket
M_{wt}	molecular weight
N	total number of sets
n_1	refractive index of air in Figure 3.1
$\tilde{n}_2$	complex optical refractive index of oxide in Figure 3.1
$\tilde{n}_3$	complex optical refractive index of metal in Figure 3.1
NbC	niobium carbide
Λ_A	coolant exposure ratio
P	pressure (Pa) in Figure 2.1
P	time-dependent power
P_{in}	exit pressure of the propellant from the rocket core/combustion chamber
P_{out}	propellant pressure at the nozzle exit
P_{amb}	ambient pressure
q	power per area
Q	power
R	universal gas constant
ρ	density of coolant
ρ_e	electrical resistivity
ρ_s	reflectivity of the perpendicular electric vector in Figure 3.1
ρ_p	reflectivity of the parallel electric vector in Figure 3.1
R_{spec}	specific gas constant
S	surface area
σ	Stefan-Boltzmann constant ($\mathbf{5.67 \times 10^{-8} W/m^2 K^4}$)
t	time
T	temperature (K) in Figure 2.1

T	temperature of fluid
t_0	reactor operation time prior to shutdown
T_{cold}	cold surface temperature
T_{hot}	hot surface temperature
TiH_2	titanium hydride
t_s	time elapsed since shutdown
u	rocket speed
V	radiation heat transfer view factor
v	fluid velocity
v_{pipe}	fluid velocity in pipe
v_{in}	fluid velocity exiting core/combustion chamber
v_{out}	fluid velocity exiting the nozzle of the rocket
v_{eq}	equivalent exhaust velocity
W	mass flow rate (kg/s) in Figure 2.1
ZrC	zirconium carbide
ZrH	zirconium hydride
ZrH_2	zirconium(II) hydride

SUBSCRIPT

Parameter	**Explanation**
c	coating
cc	corroded coating (thermally and hydrogen exposed)
g	graphite
cg	corroded graphite
RHT	radiation heat transfer
BB	black-body
i	index number of surfaces receiving radiation
j	index number of fuel element surfaces

INTRODUCTION

A nuclear thermal rocket (NTR) is a vehicle launched into space for long-term space missions. These propulsion rockets have a propellant tank full of coolant, which is pumped to a high temperature nuclear fission reactor core. The idea is for the reactor core to heat the coolant (also known as propellant or working fluid) and expel the coolant at an exhaust pressure. NTRs have a neutron reflector and core support structure. In contrast to nuclear power plants, NTRs have control drums to control the reactivity. Compared to chemical propulsion rockets, the reactor core serves as the combustion engine/combustion chamber. Aside from NTRs, nuclear electric fission rockets (NEFRs) have also been devised. NEFRs, while distinct from NTRs, have similar fundamentals to nuclear power plants, for example, a reactor core, an energy conversion system, and a heat rejection system. The following NEFRs have operated in space: (i) the BUK and TOPAZ reactors of Russia, and (ii) the SNAP-10A reactor of the United States. However, NTR designs have not operated in space (Summerer & Stephenson, 2011). Nuclear reactors for space exploration have design criteria that share some similarities and differences with those of terrestrial nuclear reactors. According to De Grandis et al (2004) and Finzi, Lombardi, and Summerer (2007), nuclear reactors for space exploration have the following design criteria: (i) produce required electrical power (most relevant for NEFRs), (ii) need to last for the required time period sans human intervention and refueling, (iii) limited mass and volume of design due to payload, (iv) meet safety requirements of the terrestrial nuclear reactors, (v) less maintenance and repair procedures than terrestrial reactors, and (vi) prevent leakage of fluids and possess safety systems to address these. Summerer and Stephenson (2011) list the following design criteria: (i) sufficient efficiency concerning heat removal in space and launch environments, (ii) very small and compact reactor cores, (iii) very high enrichment ratios, (iv) high core temperatures, and (v) low core power densities to enable long usage times.

NTRs have utilized different kinds of coolants. The Los Alamos Scientific Laboratory (LASL) utilized ammonia for their KIWI reactors. The Lawrence Livermore Laboratories used nitrogen for the Tory reactors. The Rocketdyne Division of North American Aviation conducted nuclear rocket studies for US Air Force. Their studies showed that liquid hydrogen is a more suitable propellant than ammonia and nitrogen (Gunn, 2001).

NTRs need less fuel per payload than chemical combustion rockets. In addition, they are preferred over chemical propulsion rockets because they have the capability to minimize travel time and risks to near-earth objects and Mars (Akyuzlu, 2015). NASA believes NTRs can reduce the travel time to Mars by 50% (Russon, 2015). Studies of NTRs are also beneficial in helping design

and test nuclear safety systems for current and future nuclear power plants. Lessons learnt from nuclear propulsion can be utilized in this area.

The NERVA program of NASA investigated several NTR designs from 1959 to 1973. The first NTR design developed was the KIWI B4D in 1964. The last NTR design developed was the Nuclear Furnace-1. Aside from these, prototype designs of NTRs include NRX, Phoebus, Pewee, and XE Prime. Out of these designs, the Pewee had the highest operating temperature of greater than 2500 K and the Nuclear Furnace-1 had the longest reactor operation time of approximately 160 minutes (Houts, 2014).

Several transients, whether intended or unintended, have been experimented/simulated on nuclear space reactors. In the following paragraphs, we present some examples of transients that have been done.

Robbins and Finger (1991) reported about the tests performed on the KIWI, Phoebus, and the NERVA reactors. From these tests, it was demonstrated that an NTR start-up method known as "bootstrap" was possible using the stored heat energy of the nozzle and reflector. Bootstrap is a start-up means by which a fraction of the flow goes to the turbine-side of the turbopump, to generate enough torque to accelerate the pump.

Buden (1970) defined the start-up transient in detail by dividing it into two stages: (a) preconditioning stage (period where a start-up condition is determined to satisfy both performance and time) and (b) thrust-buildup (where temperature ramp rates as high as 27.78 K/s are possible).

Peoples (1970) computationally studied transients of the following: (a) control drum run-in, (b) decrease of coolant flow, (c) decrease of coolant inlet temperature, and (d) a loss of coolant accident (LOCA) on a lithium-cooled space power fast-spectrum reactor. In particular, computer programs such as FORE and the Continuous System Modeling Program (CSMP) were used for the reactivity and flow rate transients, respectively. For part (a), the reactivity insertion accident due to run-in of the control drums isn't a major issue as long as the reactivity insertion rates are restricted to a safety margin less than \$0.097/s. For part (b), the reactor can operate at a lithium flow rate 90% less than the standard steady-state flow rate as long as the fuel element temperature doesn't reach/exceed 1388.89 K. For part (c), a safety margin of 40 seconds is necessary to respond to a transient where the lithium inlet temperature is 116.67 K less than the normal steady-state conditions. For part (d), a large emergency lithium supply is needed to remove the decay heat and prevent meltdown of the core.

Turney, Kieffer, and Petrik (1971) computationally studied reactivity insertion transients, primary coolant (lithium) flow rate transients, and secondary coolant (argon) flow rate transients on a conceptual nuclear Brayton space power plant. From their work, they discovered that the reactor

takes about 275 seconds to reach steady-state after a reactivity insertion of $0.30. However, step change in lithium flow-rate had minimum impact on the reactor's response. An increase in the argon flow rate by 15% corresponded to an increase in reactor power by 17 %.

According to Kruger (1992), experiments such as a burst transient, an irradiation transient, and a fuel flow transient were done at the Transient Reactor Test (TREAT) facility. This work demonstrated that cermet fuel, which consists of uranium dioxide embedded with a metal in a matrix, has favorable thermal and mechanical properties and can withstand severe transients.

Damerval and Durkee (1970) performed pressure and temperature transients on a nuclear rocket experimental engine known as XE-Prime. In addition to the experiment, they also ran computer simulations. This work showed that start-up can be monitored over a broad domain of initial conditions.

Akyuzlu (2015) developed a 1D mathematical model to simulate thermal-hydrodynamic transients in the cooling channels of a nuclear thermal propulsion engine. Akyuzlu and Coote (2013) developed a one-dimensional mathematical model to estimate the temperature and pressure transients inside the coolant channels of an NTR. For this work, an NTR engine from project Rover, which was part of NASA's NERVA program; was assumed. The following transients were assumed: (i) turbopump anomalies resulting in flow rate changes, and (ii) varying power output conditions. Overall, the one-dimensional model was successful in simulating the response due to these transients. The results showed in particular that the thermal response time to power excursion and mass flow rate transients is minimal. In addition, increases in coolant temperature due to power increases can be counteracted by increasing the flow rate through the system.

Schmidt, Lazareth, and Ludwig (1993) used a computer code known as KINETIC to study flow and heat transfer transients associated with an NTR, based on the Particle Bed Reactor (PBR) design. KINETIC code is based on the point reactor model and has nodes to describe fluid dynamics and heat transfer mechanisms. The broad range of the KINETIC code includes nucleonics, hydraulics, heat transfer, control rods, turbo-pump assemblies, valves, and nozzles. Schmidt, Lazareth, and Ludwig (1993) concluded that KINETIC is a suitable transient analysis algorithm to investigate start-up and shutdown profiles of the PBR-based NTR. In addition, KINETIC can be used to assess turbo-pump assembly start strategies, modify design of reactor for the purpose of reducing feedbacks, and assess engine shutdown strategies.

In this dissertation, the NTR of interest that has been selected for further study is the Pewee I Test Reactor. The following studies are presented in this dissertation: (i) modeling of the Pewee I in steady-state mode, (ii) modeling of the corrosion-induced blockages on Pewee core fuel elements and their impact of radiation heat transfer, (iii) modeling of LOFA and its impact on radiation heat

transfer in the Pewee core, and (iv) design and testing of a passive decay heat removal system for response to LOFA. In the chapters that follow, a description of rocket propulsion fundamentals will be provided. Next, a description of the Pewee I Test Reactor will be provided. This will be followed by a description on corrosion mechanisms as they relate to NTR fuel elements. Next, there will be a description of the RELAP5 model for the Pewee and an explanation of how the model was tuned and with some sample steady-state results. There will also be a presentation on incorporating the conduction models and also the radiation heat transfer models in the RELAP5 model. The first transient, which is about modeling of the corrosion-induced blockages on Pewee core fuel elements and their impact of radiation heat transfer, will be presented. The second transient, which is about modeling LOFA and its impact on radiation heat transfer in the Pewee core, will also be presented. Then, the design and testing of the passive safety system will be presented. A final conclusion will be provided to summarize the major findings in this dissertation.

CHAPTER 1: ROCKET PROPULSION FUNDAMENTALS

1.1 Introduction

This chapter presents the fundamental formulae associated with rocket propulsion, regardless of whether they be chemical or nuclear rockets. In addition, arguments are made as to why nuclear rockets are needed over chemical rockets.

1.2 Fundamental formulae associated with rockets

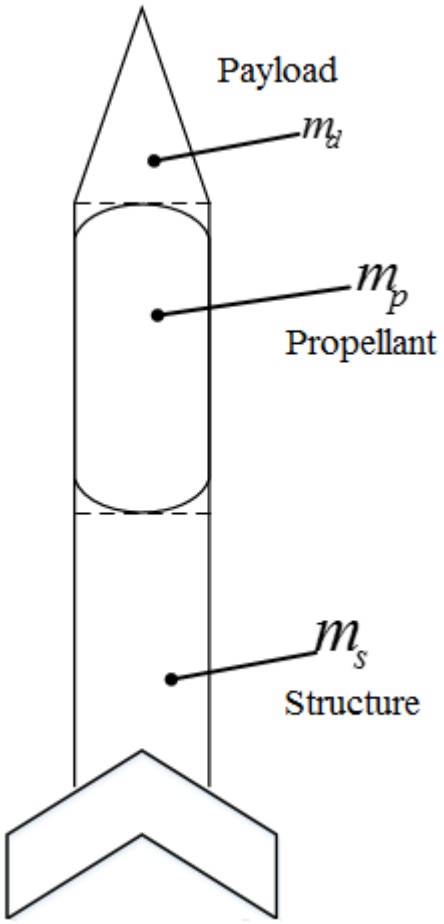

Figure 1.1 Diagram of rocket with various mass partitions

Here, we present some of the equations relevant to both chemical and nuclear rockets. These equations are taken from NASA (NASA, 2016). Figure 1.1 presents a simple drawing of a rocket with mass partitions. The payload is the mass of the cargo or civilians the rocket is carrying. It is also referred to as the mass of the rocket with the propellant and structure subtracted. The propellant as mentioned in the introduction is the working fluid of the rocket. The structure is the part of the rocket that includes the engine/booster system. The rocket is partitioned into three mass systems such as

payload mass m_d, propellant mass m_p, and structural mass m_s. The full mass of the rocket m_f is given by

$$m_f = m_d + m_p + m_s. \qquad (1.1)$$

The empty mass of the rocket m_e is given by

$$m_e = m_d + m_s. \qquad (1.2)$$

Notice that the empty mass is basically the mass of everything inside the rocket, excluding the propellant.

The payload ratio α_d is given by

$$\alpha_d = \frac{m_d}{m_f - m_d} = \frac{m_d}{m_p + m_s}. \quad (1.3)$$

The structural ratio β_s is given by

$$\beta_s = \frac{m_s}{m_s + m_p} = \frac{m_s}{m_f - m_d}. \quad (1.4)$$

The propellant mass ratio MR is given by

$$MR = \frac{m_f}{m_e} = 1 + \frac{m_p}{m_e} = \frac{1 + \alpha_d}{\beta_s + \alpha_d}. \quad (1.5)$$

In reality, a high α_d implies a large payload can be handled by a small amount of propellant. A low β_s indicates a good booster design. A high MR indicates a large increase in rocket velocity. All of these are desired for rockets in general, regardless of propulsion type.

The Mach number is the ratio of the speed of the gas to the speed of sound in gas. Mathematically, it is given by

$$M_e = \frac{v}{a} = \frac{v}{\sqrt{\gamma R_{spec} T}}, \qquad (1.6)$$

where

$$\gamma = \frac{c_p}{c_v} \tag{1.7}$$

is the ratio of specific heats,

$$R_{spec} = \frac{R}{M_{molar}} = c_p - c_v \tag{1.8}$$

is the specific gas constant, *R* is the molar gas constant, c_p is the specific heat capacity at constant pressure, c_v is the specific heat capacity at constant volume, M_{molar} is the molar mass, v is the speed of the fluid, T is the temperature of the fluid, and *a* is the speed of sound . For dry air, R_{spec} has the value of 287.058 J/KgK or 287.058 m^2/s^2K. The Mach number is very important since compressibility effects need to be considered when a fluid is passing through a duct with contracting/expanding flow area. Table 1.1 shows the various domains of the Mach number.

Table 1.1 Ranges of the Mach number

Mach # domain	Classification	Notes
M_e <1	Subsonic	-Compressibility is neglected -Happens at rocket nozzle inlet
M_e =1	Transonic	-Compressibility effects are significant -Happens at rocket nozzle throat
M_e >1	Supersonic	-Compressibility effects more significant -Happens at rocket nozzle exit

Figure 1.2 presents a small diagram of the rocket nozzle. Here, $\dot{m}$ is the mass flow rate of the propellant, v_{in} is the velocity from the core/combustion chamber, T_{in} is the exit temperature of the propellant from the core/combustion chamber, P_{in} is the exit pressure of the propellant from the core/combustion chamber, A_{out} is the flow area of the nozzle exit, A_t is the flow area of the nozzle throat, v_{out} is the exhaust velocity at the nozzle exit, T_{out} is the temperature of the propellant at the nozzle exit, P_{out} is the pressure of the propellant at the nozzle exit, and P_{amb} is the ambient pressure.

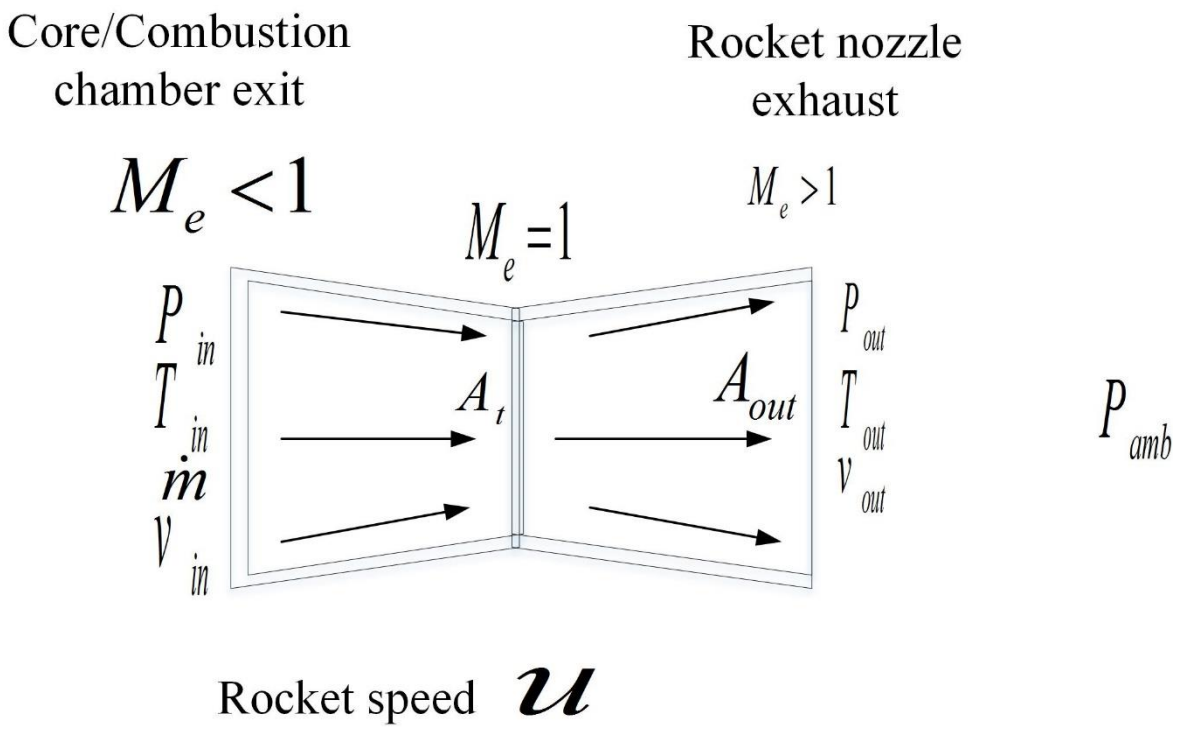

Figure 1.2 Diagram of the rocket nozzle with important variables

The mass flow rate through the rocket nozzle is given by

$$\dot{m} = \frac{A_t P_{in}}{\sqrt{T_{in}}} \sqrt{\frac{\gamma}{R_{spec}}} \left(\frac{\gamma+1}{2} \right)^{\frac{-(\gamma+1)}{2(\gamma-1)}}. \tag{1.9}$$

The ratios of the flow areas, A_{out} to A_t, is given by

$$\frac{A_{out}}{A_t} = \left(\frac{\gamma+1}{2} \right)^{\frac{-(\gamma+1)}{2(\gamma-1)}} \frac{\left(1 + \frac{\gamma-1}{2} M_e^{\,2} \right)^{\frac{\gamma+1}{2(\gamma-1)}}}{M_e}. \tag{1.10}$$

The exiting temperature is given by

$$\frac{T_{out}}{T_{in}} = \left(1 + \frac{\gamma-1}{2} M_e^{\,2} \right)^{-1} \tag{1.11}$$

and the exiting pressure is given by

$$\frac{P_{out}}{P_{in}} = \left(1 + \frac{\gamma-1}{2} M_e^{\,2} \right)^{-\frac{\gamma}{\gamma-1}}. \tag{1.12}$$

.

The exhaust velocity of the propellant is given by

$$v_{out} = M_e \sqrt{\gamma R_{spec} T_{out}} \ . \tag{1.13}$$

The thrust of the rocket is given by

$$F_{th} = \dot{m} v_{eq} = \dot{m} v_{out} + \left(P_{out} - P_{amb}\right) A_{out}, \tag{1.14}$$

where v_{eq} is the equivalent exhaust velocity.

The specific impulse is given by the total impulse divided by the weight of the propellant. Mathematically, we have the equation

$$Isp = \frac{\int F_{th} dt}{m_p g} = \frac{\dot{m} v_{eq}}{\dot{m} g} = \frac{v_{eq}}{g}. \tag{1.15}$$

The equivalent exhaust velocity v_{eq} is given by

$$v_{eq} = v_{out} + \frac{\left(P_{out} - P_{amb}\right) A_{out}}{\dot{m}} . \tag{1.16}$$

The Tsiolkovsky rocket equation, also known as the ideal rocket equation, is given by

$$\Delta u = v_{eq} \ln\left(\frac{m_f}{m_e}\right) = v_{eq} \ln\left(MR\right) = \left(Isp\right) g \ln MR . \tag{1.17}$$

The significance of Equation (1.17) is that a high change in the rocket velocity is needed to travel from the earth to the cosmos and beyond. This equation can be re-arranged to get

$$MR = e^{\frac{\Delta u}{(Isp) g}} \tag{1.18}$$

or

$$\frac{m_p}{m_e} = e^{\frac{\Delta u}{(Isp) g}} - 1. \tag{1.19}$$

Figure 1.3 shows a plot of the specific impulse for several types of rockets. From Figure 1.3, we can summarize the specific impulse ranges as shown in Table 1.2. As noticed, nuclear rockets have a higher specific impulse than chemical rockets. This is desired because a higher specific impulse implies a higher rocket equivalent exhaust velocity. If both the chemical rocket and nuclear rocket were to have the same propellant mass ratio (MR), the nuclear rocket would have the higher Δu . Of course, the higher the Δu , the greater the probability of exiting the earth's atmosphere and entering the cosmos.

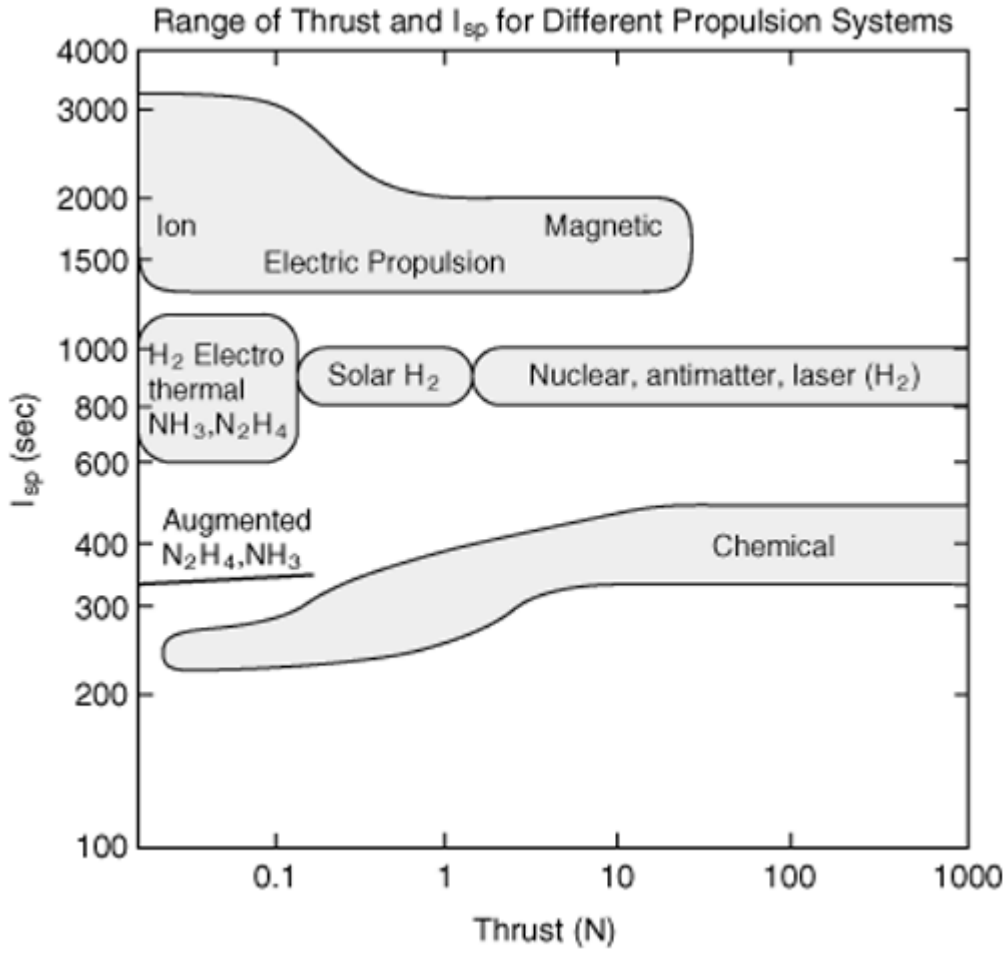

Figure 1.3 Graph of specific impulse compared with thrust for several propulsion systems (Source: NASA Jet Propulsion Laboratory, ND)

Table 1.2 Ranges of specific impulse for propulsion systems

Propulsion type	Isp range
Chemical	230-500
Augmented N_2H_4, NH_3	320-330
H2 Electrothermal NH_3, N_2H_4	600-1200
Solar H_2	800-1000
Nuclear, antimatter, laser (H_2)	800-1000
Electric propulsion	1400-3100

Let us do a comparison to see how the MR for the nuclear rocket compares to the MR for the chemical rocket, in order to achieve the same Δu .Starting with Equation (1.17), we have the following

$$Isp_{nuke}\, g \ln\left(MR_{nuke}\right) = Isp_{chem}\, g \ln\left(MR_{chem}\right), \qquad (1.20)$$

where Isp_{nuke} is the specific impulse of the nuclear rocket, Isp_{chem} is the specific impulse of the chemical rocket, MR_{nuke} is the propellant mass ratio of the nuclear rocket, and MR_{chem} is the propellant mass ratio of the chemical rocket. This equation can be re-arranged in order to get

$$MR_{nuke} = e^{\frac{Isp_{chem}}{Isp_{nuke}} \ln\left(MR_{chem}\right)} \qquad (1.21)$$

Alternatively, we can write

$$\left(\frac{m_p}{m_e}\right)_{nuke} = e^{\frac{Isp_{chem}}{Isp_{nuke}} \ln\left(\left(\frac{m_p}{m_e}\right)_{chem}+1\right)} - 1. \qquad (1.22)$$

Figures 1.4 shows a plot of MR_{nuke} vs MR_{chem}. Figure 1.5 shows a plot of $\left(\frac{m_p}{m_e}\right)_{nuke}$ vs $\left(\frac{m_p}{m_e}\right)_{chem}$.

Here, it is assumed that Isp_{chem} =365 s and Isp_{nuke} =900 s, in accordance with Table 1.2 and Figure 1.3.

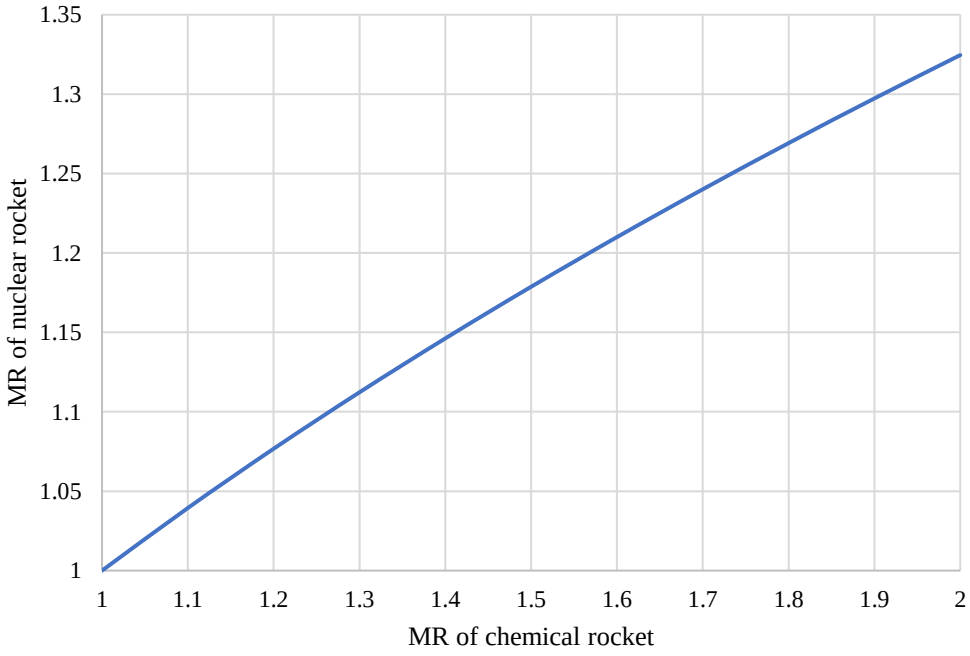

Figure 1.4 Comparison of MR for nuclear and chemical rockets to achieve same Δu

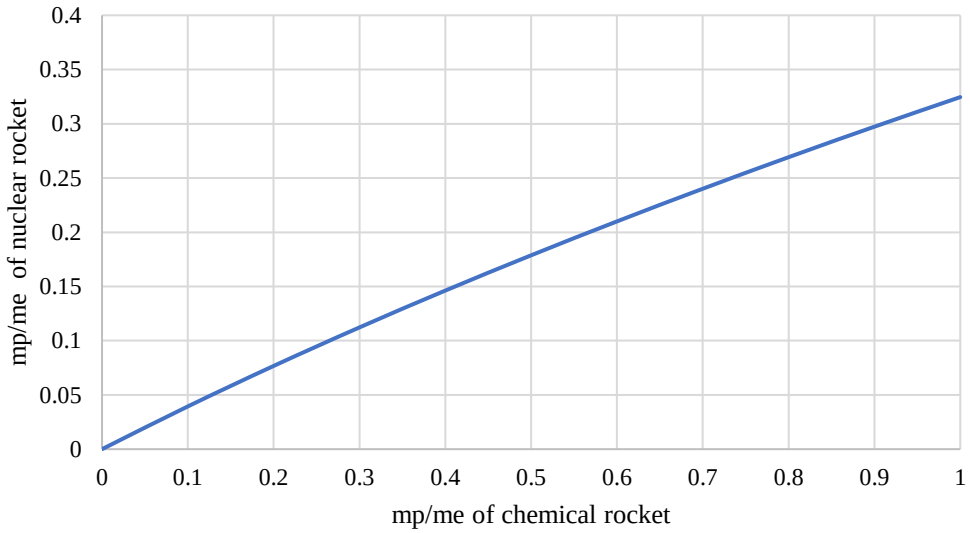

Figure 1.5 Comparison of $\frac{m_p}{m_e}$ for nuclear and chemical rockets to achieve same Δu

From Figures 1.4 and 1.5, show that the nuclear rocket needs a smaller MR and $\frac{m_p}{m_e}$ in order to match the same Δu as the chemical rocket. This, once again, shows that nuclear rockets are preferred over chemical rockets. In addition, nuclear rockets can utilize propellants with lower molecular weights compared to chemical rockets. Propellants with lower molecular weights increase the specific impulse as per the approximation

$$Isp \approx \sqrt{\frac{T_{in}}{M_{wt}}}, \qquad (1.23)$$

where M_{wt} is the molecular weight. Hence, this is why the work in this dissertation will focus on the RELAP5 modeling of NTRs rather than chemical rockets.

CHAPTER 2: DESCRIPTION OF THE PEWEE I TEST REACTOR

The Pewee I Test Reactor is a scaled-down version of the Phoebus design, built to test the fuel elements. The Phoebus design was a reactor under Project Rover, which was managed by three organizations: Atomic Energy Commission, Los Alamos Scientific Laboratory (LASL), and NASA. Pewee I had roughly 25% of the fuel elements in the Phoebus design. It was never operated in space (Finseth, 1991). The Copernicus Spacecraft, designated by NASA for missions to Mars in the 2030's, has been designed assuming three Pewee-type engines are utilized. Pewee-type engines each have a thrust of 111.21 KN (Borowski, McCurdy, & Packard, 2012).

The Pewee I (Figure 2.1) has a core diameter of 0.53 m and a ratio of support elements to fuel elements of 1:3. The reactor core has 402 uranium-loaded graphite fuel elements, each with a height of 1.32 m. Out of these fuel elements, 390 of these are 19-hole type and the rest are 12-hole type. Total uranium-inventory in the core is 36.42 kg (LASL, 1969). The reactor core is surrounded by an annulus and then by a beryllium reflector. The outer part of the reflector is manufactured from Phoebus type sectors and has control drums of 0.1 m diameters. The thickness of the reflector is 0.20 m. The aluminum support plate is 0.08 m thick. The reactor pressure vessel is fabricated from aluminum and has a nozzle throat diameter of 0.15 m. The nozzle exit has a diameter of 0.41 m.

Figure 2.1 shows the basic flow diagram of the Pewee I with the important parameters such as mass flow rate (W), pressure (P), and temperature (T). The propellant inlet is where the majority of the propellant enters into the main reactor system. From there, it travels through the 120 coolant tubes located within the rocket nozzle. Then, the propellant mixes with part of the propellant that enters via the nozzle bolt cooling passage. The mixed propellant continues through an annular expansion region and then into coolant holes of the beryllium reflector. Upon exiting the beryllium reflector, the propellant mixes with part of the propellant via the pressure vessel bolt cooling passage. Aside from the main propellant inlet, the rest of the propellant enters the reactor via the tie rod manifold. There is some flow that goes through the core and some that bypasses the core. The core region has 4 major coolant channels: the fuel elements (includes 19 and 12-hole fuel elements), which handles most of the flow; the "once-through" tie rods, which receive coolant directly via the tie rod manifolds and contain the zirconium hydride (ZrH) moderator sleeves; and the M1 elements, which are unloaded peripheral elements; and the slats, which are tubes with rectangular-like geometry. The annulus is located outside the core barrel and is surrounded by the reflector. The annulus receives flow that bypasses the core. From Figure 2.1, the flows through each of these channels add up to 18.59 kg/s. In addition, the resultant coolant temperature entering the nozzle inlet is 1755.23 K. The coolant flows downstream through the nozzle and is released into the atmosphere

as thrust.

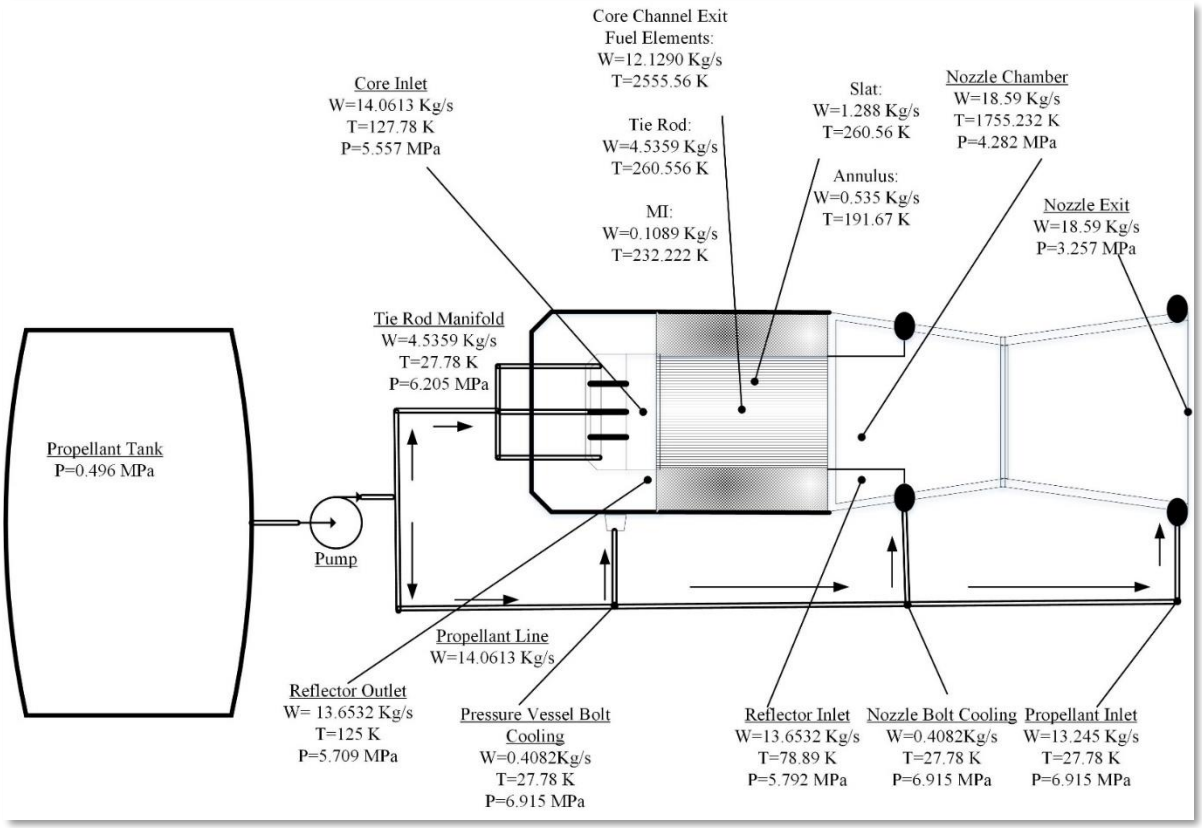

Figure 2.1 Pewee flow diagram

In Figure 2.1, the propellant is pumped from the propellant tank and enters the main rocket system via the main propellant line, nozzle bolt cooling, pressure vessel bolt cooling, and tie rod manifolds. Had the Pewee I operated in space, the pump and the propellant tank would most likely be located on the top of the pressure vessel dome. Although not shown in the diagram, the pressure vessel dome has 9 control drums and 3 support rod coolant manifolds located on top of it.

Figure 2.2 shows the top of the beryllium reflector. The inner beryllium cylinder, control drum, beryllium sector, and poison plate are also visible. The poison plate is used for long-term reactivity control. The unidentified holes are coolant channels through the reflector. In Figure 2.3, the pressure vessel dome has 9 control drums and 3 coolant support rod manifolds (also known as tie rod manifolds) are shown.

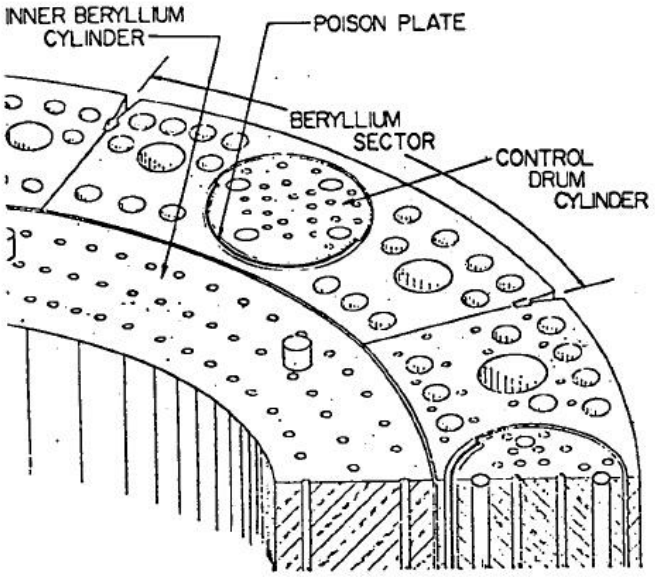

Figure 2.2 Quarter of top part of beryllium reflector (LASL, 1969)

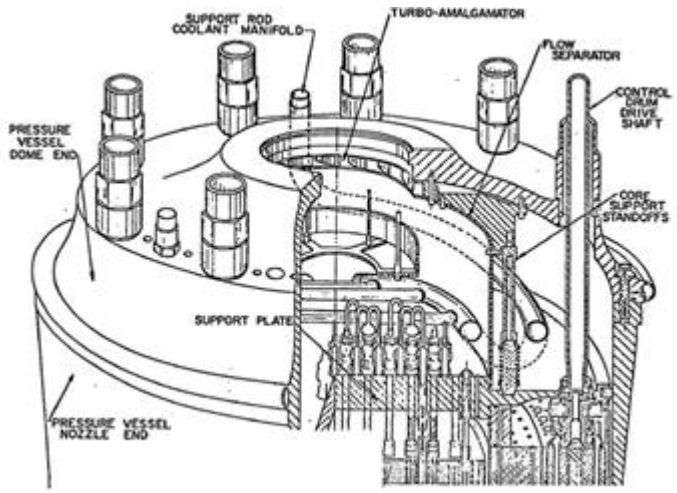

Figure 2.3 Top of pressure dome (LASL, 1969)

In Figure 2.4, a 19-hole fuel element is shown. The holes serve as passages for the hydrogen coolant to pass through the main core. Each of these holes has a diameter of 0.00279 m (LASL, 1969). The tie rod tubes have both an outer tube and an inner tube as shown in Figure 2.5. In the Pewee design, the coolant flows through both tubes in the same direction. Also, notice the layers of ZrH, ZrC, gap, and graphite. Figure 2.6 shows a 60° cutout of the core. The graphite slats are on the boundary of the core. There is an inner radius formed by the pyro strips. The pyro strips are fabricated from pyrographite and serve as insulation material. Within this radius of pyro strips are the uncooled filler elements, the hexagon-shaped M1 elements, tie rod tubes, and fuel elements (19-hole and 12-hole). This radius formed by pyro strips could be thought of as an inner core boundary.

There are 6 M1 elements in the core and these neighbor the uncooled filler elements, pyro strips, and 19-hole elements. There are 120 tie rods in the core.

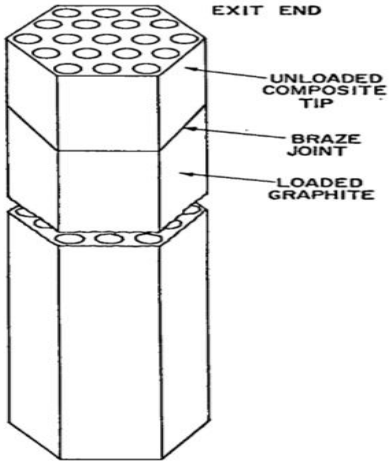

Figure 2.4 19-hole fuel element (LASL, 1969)

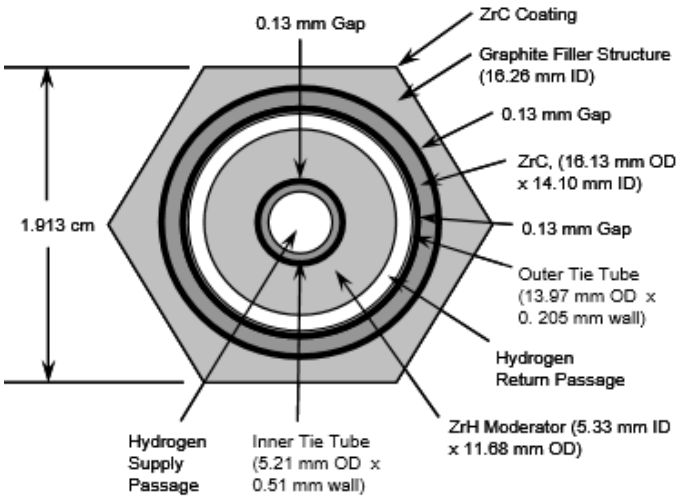

Figure 2.5 Tie rod tube top view (Fittje & Schnitzler, 2008)

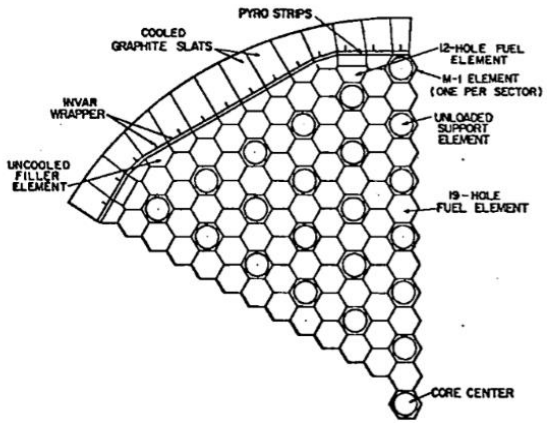

Figure 2.6 60°-degree cutout of core (LASL, 1969)

CHAPTER 3: MECHANISMS OF CORROSION ON NTR FUEL ELEMENTS

Corrosion is an electrochemical process that results in the metal departing to its initial thermodynamic state (i.e. the state at which it was prior to being refined). This process involves reforming the oxides and sulfides the metal had prior to refinement (Schweitzer, 2009). Corrosion results in the surface deterioration of metals.

The types of corrosion most commonly identified in nuclear power systems include intergranular corrosion, erosion, stress-corrosion cracking, mass-transfer corrosion, and hydrogen embrittlement (Glasstone & Sesonske, 1994). Intergranular corrosion affects the grain boundaries of the metal. In particular, the grain boundary with limited area serves as the anode and the larger areas of grain serve as cathodes. Hence, there is a transfer of energy from the anode to the cathode, therefore resulting in a swift attack that has a great depth of penetration. Erosion is the type of corrosion where the metal surface deteriorates due to an aqueous/gaseous corrodent flowing over it. Stress-corrosion cracking is when metals are exposed to surroundings with static tensile stress, hence leading to delayed failure in the form of cracking (Schweitzer, 2009). Mass-transfer corrosion is the type of corrosion where the content of a metal is detached by a working fluid. For example, in fast reactors, where molten sodium has estimated coolant temperatures of 723 K, the coolant may remove carbon from the ferritic steel (which has fairly high carbon content) and transfer it to a near-by austenitic steel (which has low carbon content) component, hence degrading both steels (Glasstone & Sesonske, 1994).

For the Pewee I, hydrogen embrittlement is the most relevant problem. Hydrogen embrittlement is where hydrogen enters the material via the corrosion process and due to extremely high pressures. Intergranular fracture is one of the main outcomes of hydrogen embrittlement; it is at a maximum at low strain rates (Was, 2007). The mechanisms in which hydrogen causes embrittlement include the decohesion mechanism and the pressure theory. The decohesion mechanism suggests that atomic hydrogen decreases the metal-metal bond strength. The pressure theory suggests that the precipitation of hydrogen gas at internal defects at the applied stress decreases the fracture stress. Blisters arise if the process transpires adjacent to the surface, hence deforming the thin layer of metal surrounding it. The hydrogen attack mechanism is another phenomenon that explains hydrogen embrittlement. Here, the reaction between hydrogen and carbon forms methane gas bubbles and results in de-carburization plus loss in metal strength (Was, 2007).

In addition to the previously mentioned mechanisms of hydrogen embrittlement, direct adsorption of hydrogen is said to decrease the surface energy needed to form a crack, hence causing the fracture stress to decline. When the hydrogen is in contact with zirconium or titanium alloys, a brittle hydride phase such as zirconium(II) hydride (ZrH_2) or titanium hydride (TiH_2) can increase embrittlement of the metal. The hydride has a greater specific volume than the metal it resides in. If the applied stress is perpendicular to the metal surface containing the hydride, the hydride will experience a high tensile stress. With zirconium alloys being used as cladding material in light water reactors, hydride platelets form on planes that are oriented in the radial direction and cause a high tensile stress in the metal due to the pressure (Was, 2007).

There are six major stages of corrosion (Schweitzer, 2009). In describing the six stages of corrosion, let us assume the metal undergoing corrosion is iron. The first stage of corrosion includes symptoms such as noticeable existence of rust. In addition, blistering is also another symptom. Blistering occurs either due to osmotic attack or because moisture has made the metal's coating more diluted.

The second stage of corrosion involves the formation of multiple rust spots beyond those formed in the first stage. The majority of the rusts in this stage are iron(III) oxide (Fe_2O_3), which is a red rust. Atmospheres where oxygen is limited develop black iron(II) oxide (FeO) rust. The third stage of corrosion involves the complete removal of the coating from the substrate, hence leaving the substrate vulnerable to the corrodents. Since the coating is unable to provide resistance to the corrodents, corrosion can transpire at a rapid rate. In the fourth stage of corrosion, pitting occurs where small holes are formed in the material.

The fifth stage of corrosion has pitting taking place to the extent that undercutting, flaking, and delamination of the substrate has occurred. The development of small holes leads to the electrolyte having access to the reverse side of the substrate-making corrosion occurring on both sides of substrate. In the sixth and final stage of corrosion, corrosion occurs at the most rapid rate and large holes evolve, hence resulting in structural damage.

Sophisticated corrosion models exist that incorporate layered structure of oxide and morphology. Radiation heat transfer models in the computer simulations are either extremely rough models and/or not sensitive to the change on the material's properties, such as corrosion, surface roughness, oxidbreaking scale spallation, small cracks, etc. Heat transfer models show that most of the codes are not integrated with materials codes, such as a fuel performance code, to observe the effects of oxidation and radiation on the materials. This is because constant values are used for the parameters (such as emissivity coefficient during each fuel cycle and even in lifetime of the power plant) of radiation heat transfer formula, as shown later.

Consider an opaque, gray, and diffuse surface (indexed using "i") that receives radiation from a fuel element surface (indexed using "j"), then the radiosity of the i-th surface is given by

$$J_i = \varepsilon_i \sigma T_i^4 + (1-\varepsilon_i)\sum_{j=1}^{N} V_{ij} J_j , \qquad (3.1)$$

where ε_i is the emissivity of the i-th surface, σ is the Stefan-Boltzmann constant, T_i is the temperature of the i-th surface, V_{ij} is the view factor from the i-th surface to the j-th surface, J_j is the radiosity of the j-th surface, and N is the number of the j-th surfaces.
The resulting heat transfer per area is given by

$$q = \frac{\varepsilon_i}{1-\varepsilon_i}\left(q_{BB,i} - J_i\right), \qquad (3.2)$$

where

$$q_{BB,i} = \sigma\, T_i^4 \qquad (3.3)$$

is the blackbody emissive power.

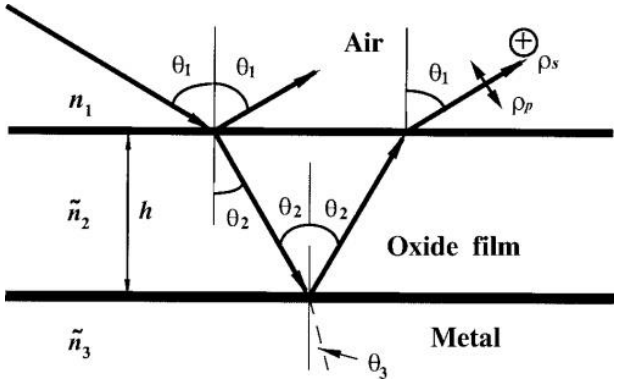

Figure 3.1 Emissivity model of oxide on a metal system (Iuchi, Furukawa, & Wada, 2003)

Emissivity is the material's physical property that defines its ability to release heat through radiation (Figure 3.1). It is determined by the interaction of the electromagnetic field with the material. The material's dielectric constant or refraction index is used to conveniently capture this interaction. Emissivity not only depends on the materials properties, but also on the radiation wavelength λ and direction with respect to the surface normal. In transparent material such as oxide, normal emissivity can be described by

$$\varepsilon_n(\lambda) = \frac{4n}{(n+1)^2}, (n = n_2/n_1), \qquad (3.4)$$

where n_1 and n_2 are refractive indices for oxide and air, which are functions of wavelength. From this relation, the emissivity is close to zero when optical refractive indices of both materials are equal to each other. In metals, normal emissivity can be approximated by the Hagen-Rubens relation given by

$$\varepsilon_n(\lambda) = 36.5\left(\frac{\rho_e}{\lambda}\right)^{1/2} - 464\frac{\rho_e}{\lambda}, \qquad (3.5)$$

where ρ_e is electrical resistivity in ohm-cm and λ is the wavelength in μm. In the case where the oxide layer is present on the surface of the metal, the emissivity is a combined contribution of the transparent layer and metal, which includes thickness of the oxide layer. Emissivity also depends on surface roughness and impurities. For example, pure polished material has the lowest emissivity and surface roughness results in higher emissivity. In addition, an increase in the oxide layer thickness also increases the emissivity, eventually reaching a maximum. Sophisticated models of emissivity exist and incorporate layered structure of oxide and morphology (Figure 3.2). On the other hand, corrosion models of various metal alloys in oxygen environment are available and can be combined to provide a unified time-dependent emissivity model. While the corrosion correlation in impure helium environments is not readily available for most candidate materials, there are a number of reports discussing the detrimental effect of carbon monoxide and methane on the protectiveness of oxide scales in various metal alloys under the concept of carbon dusting (Grabke, Krajak, & Muller-Lorenz, 1993).

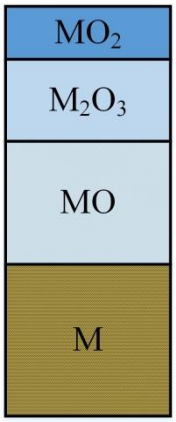

Figure 3.2 Multilayered microstructure of oxidation

The actual composition of oxide scale and kinetics are a function of temperature. Since the structure of oxide scale affects its optical properties, special care will be taken to access emissivity properties of samples with accelerated oxidation. Alloy 800H and type 316 stainless steel are

considered for core barrel. Both are expected to have similar oxidation behavior and form chromium oxide layers during air oxidation.

The Pewee I is an NTR design with fuel encapsulated in graphite. Graphite encapsulated fuel elements in particular are vulnerable to corrosion. Corrosion is caused by the hot coolant temperatures and can cause thermal, structural, or neutronic problems (LASL,1969) (Simmons, 1969) (Seo et al, 2009) (Pelaccio, El-Genk, & Butt, 1994). Thermal problems arise from the heat transfer from the corroded surfaces and also from enlarged coolant passages that counteract the required propellant temperatures for thrust. Structural problems arise from corroded web structures and turbulent flow-induced vibrations that result in cracks, fractures, and dislocation of broken fuel elements. A decrease in the mass of graphite leads to neutronic changes and ultimately a reduction in the minimum excess reactivity to achieve the required power density levels.

Finseth (1991) reports that despite attempts made to limit corrosion, there were still some shortcomings. Since the corrosion of graphite by hydrogen coolant is strongly temperature dependent, the minimum temperature for which noticeable reaction occurs is at temperatures of approximately 620 K. The Arrhenius equation is suitable for predicting the corrosion rate. The Arrhenius equation is given by

$$Ln(K) \propto \frac{E}{RT}, \qquad (3.6)$$

where K is the reaction rate, E is the activation energy, R is the universal gas constant, and T is the temperature.

The reaction of hydrogen and graphite in the NTR core forms methane or acetylene (Pelaccio, El-Genk, & Butt, 1994). The NbC or ZrC coatings are there to prevent the graphite enclosed elements from corrosion (Fishbine et al, 2014). A secondary coat of molybdenum can also be applied in addition to the NbC/ZrC coatings (LASL,1969). Chemical vapor deposition was used to apply the coatings on the Pewee rocket. This process had some disadvantages since the differences in the coefficient of thermal expansion (CTE) between the graphite matrix and NbC/ZrC results in microcracks where hydrogen interacts with the graphite. The coating materials of NbC and ZrC had CTE of 6.6 and 7.7 μm/mK, respectively. The graphite in the Pewee core had a CTE of approximately 3.3 μm/mK. The chemical vapor deposition process was done at high temperatures in order to counteract cracks from coating. Despite this, cracks evolved during cooldown and propagated during the cycling process.

The outcomes of the Pewee experiments showed that the fuel elements functioned adequately to the extent required. On the contrary, there were some issues of corrosion. The following are examples of corrosion suffered by the Pewee fuel elements (LASL, 1969): (i) mass loss per fuel

element was in the domain of 0.008-0.053 kg, resulting in an average of 0.020 kg; (ii) peripheral fuel elements were extremely corroded on the outer surface; and (iii) 46 out of 402 fuel elements were extremely corroded or cracked.

Corrosion levels of the Pewee fuel elements were categorized using three terms: (i) no damage, (ii) moderate corrosion, and (iii) heavy corrosion (LASL, 1969). For part (i), this involves minor cracking of the NbC/ZrC coating, at the very worst. For part (ii), this involves greater cracking of the NbC/ZrC coating, which eventually reaches, but does not impact, the neighboring bore(s). For part (iii), which is the most severe, this involves corrosion that can pervade from bore to bore. Figures 3.3 and 3.4 illustrate the extent of the corrosion on the fuel elements.

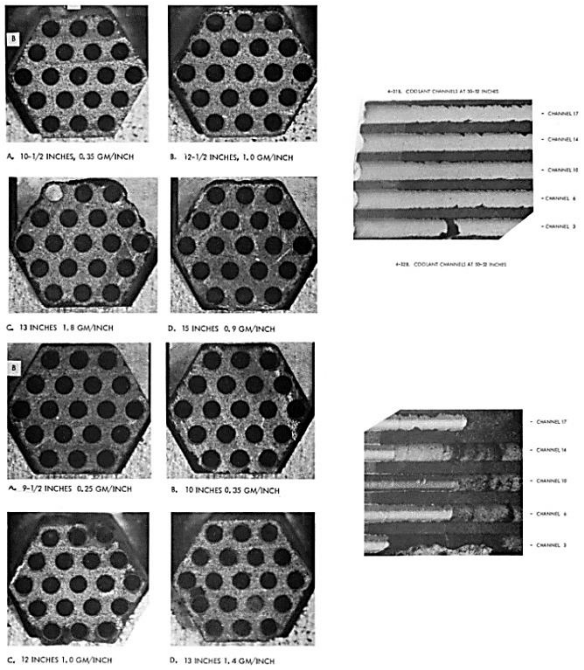

Figure 3.3 Fuel element corrosion along the axial length of channels and faces (Simmons, 1969)

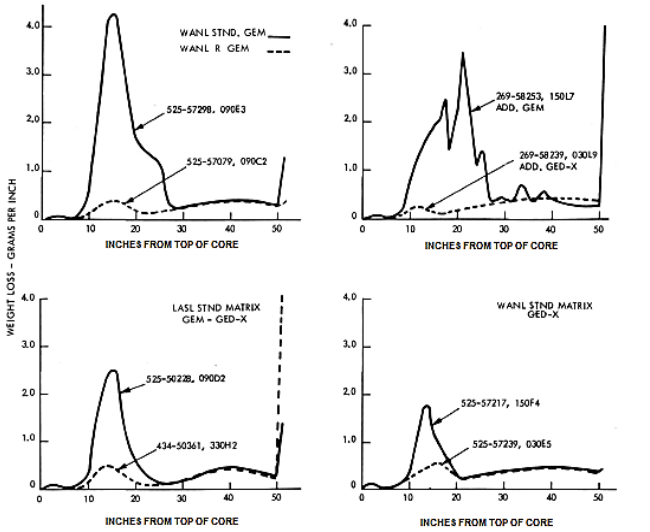

Figure 3.4 Incremental mass losses of some WANL and LASL Pewee fuel elements (Simmons, 1969)

Corrosion increases the emissivity of the material. In general, corroded surfaces have higher emissivity coefficients than fresh surfaces. Heath and Aydogan (2016) have identified some emissivity coefficients of the niobium carbide (NbC) and zirconium carbide (ZrC) coolant channels within the Pewee fuel elements. These emissivity coefficients are valid for temperatures greater than 1700 K. Table 3.1 presents some examples of emissivity coefficients.

Table 3.1 Emissivity coefficients of NbC and ZrC

	NbC	ZrC
Temperature range (K)	1700-2200	1700-2200
Polished surface	0.79	0.9
Rough surface	0.79	0.9
Thermal treatment	0.72	0.9
Hydrogen exposure	0.71	0.9

According to Heath and Aydogan (2016), a typical Pewee coolant channel has 40% NbC (or ZrC) and 60% graphite. Out of the 40% of NbC, some may be fresh and some may be corroded. The graphite part of the coolant channel will also have proportions of fresh and corroded emissivity coefficients. Table 3.2 presents the emissivity coefficients of the NbC and graphite portions.

Table 3.2 Emissivity coefficients of fresh and corroded materials

Material	Emissivity
Fresh NbC	0.79
Hydrogen exposed NbC	0.71
Uncorroded graphite	0.49
Corroded graphite	0.76

Heath and Aydogan (2016) came up with several emissivity coefficients of NbC and ZrC based channels with various fractions of fresh and corroded materials. Table 3.3 presents these emissivity coefficients. The subscripts c, cc, g, and cg correspond to surfaces for coating, corroded coating (thermally and hydrogen exposed), graphite, and corroded graphite, respectively. The overall emissivity coefficient in each case was calculated using the relation

$$\varepsilon = \Lambda_{A_c}\varepsilon_{A_c} + \Lambda_{A_{cc}}\varepsilon_{A_{cc}} + \Lambda_{A_g}\varepsilon_{A_g} + \Lambda_{A_{cg}}\varepsilon_{A_{cg}}, \quad (3.7)$$

where the Λ's are coolant exposure ratios. More specifically, these are ratios of a specific material's graphite/coating area that is exposed to hydrogen coolant to the total area of all materials exposed to hydrogen coolant.

The radiation heat transfer between a hot and cold surface is defined by

$$Q_{RHT} = \varepsilon\sigma S\left(T_{hot}^4 - T_{cold}^4\right), \quad (3.8)$$

where Q_{RHT} is the heat transfer rate from the surface to the surroundings, σ is the Stefan-Boltzmann constant ($5.67 \times 10^{-8} \mathrm{W/m^2K^4}$), S is the surface area, T_{hot} is the temperature of the hot surface, and T_{cold} is the temperature of the cold surface.

Table 3.3 Area weighted emissivity with various stages of corrosion

Λ_{A_c}	$\Lambda_{A_{cc}}$	Λ_{A_g}	$\Lambda_{A_{cg}}$	ε_{NbC}	ε_{ZrC}
0.06	0.04	0.52	0.38	0.62	0.63
0.17	0.03	0.25	0.55	0.7	0.72
0.08	0.3	0.33	0.29	0.66	0.72
0.43	0.08	0.39	0.1	0.66	0.73
0.38	0.1	0.36	0.16	0.67	0.73
0.41	0.03	0.33	0.23	0.68	0.73
0.04	0.48	0.26	0.22	0.66	0.76
0.05	0.51	0.28	0.16	0.66	0.76
0.5	0.01	0.2	0.29	0.72	0.78
0.25	0.34	0.21	0.2	0.69	0.79
0.19	0.24	0.09	0.48	0.73	0.8
0.05	0.56	0.19	0.19	0.68	0.79
0.41	0.17	0.14	0.28	0.73	0.8
0.54	0.1	0.17	0.19	0.73	0.8
0.05	0.68	0.23	0.04	0.67	0.8
0.45	0.35	0.16	0.04	0.71	0.83
0.18	0.39	0	0.43	0.75	0.84
0.05	0.67	0.04	0.24	0.72	0.85
0.37	0.45	0.03	0.15	0.74	0.87

CHAPTER 4: SYSTEM MODELING OF PEWEE I

4.1 Introduction

This chapter describes the development of the RELAP5 model of the Pewee I test reactor. RELAP nodalization diagrams and the baseline tuning of the temperature and pressure profile will be presented. There will also be a discussion concerning the incorporation of the RELAP5 radiation heat transfer models.

4.2 Nodalization diagrams and tuning of model

In order to model the radiation heat transfer in the Pewee core, we first need to assemble a RELAP5 input deck that models the major thermal hydraulic parameters of the rocket. As mentioned previously, RELAP was developed at the Idaho National Laboratory. Innovative Systems Software (ISS) improved the RELAP models to incorporate another systems code known as Severe Core Damage Analysis Program (SCDAP). While RELAP and SCDAP are used to model nuclear power plants, neither of them have been used to model nuclear reactors for space exploration. In this work, only RELAP5-3D is utilized to model the Pewee I. In Figures 4.1-4.3, the Pewee nodalization diagram is presented in three parts. Just like with most RELAP5 nodalization diagrams, most components are represented as pipes and volumes (including single volumes and time-dependent volumes) and assigned 3-digit numbers. In this particular example, the propellant inlet, nozzle bolt cooling, pressure vessel bolt cooling, and tie rod manifolds are represented as time-dependent volumes (TDV), each with time-dependent junctions (TDJ) connecting them to the main circuit. The major components are numbered and labeled in this diagram. The single junctions between the volumes are not numbered in Figures 4.1-4.2. In Figure 4.2, each of the various channels that go through or bypass the core are modeled, such as the fuel elements, slat, annulus, tie rod manifold, and M1. The coolant channels within the fuel elements were split up into 3 main RELAP5 pipes: hydrodynamic volume (HV) 430 for inner coolant channels (ICC), HV 432 for peripheral coolant channels (PCC), and HV 431 for the hot coolant channels (HCC) of the hot fuel element. Since the fuel elements in the core are scattered in a lattice such that they neighbor the tie rods, uncooled filler elements, and M1 elements, it became necessary to model the fuel elements as separate pipes with their own heat structures. In RELAP5, it is a common practice to model a hot fuel element, a cold fuel element, and average temperature fuel elements for light water reactors. The hot and cold fuel elements are modeled for the extreme situations. For the Pewee, which is a hydrogen-cooled design, we are modeling the hot fuel element for our extreme situations. There are 7554 coolant channels in the fuel elements (both 12-hole and 19-hole elements) and so HV 430 represents the 7175 ICC holes, HV 431 represents 19 HCC holes, and HV 432 represents the remaining 360 PCC holes. Note that

the core channels and reflector have heat structures (HS) attached to them. These are needed in order model heat generation in the fuel elements and to transfer the heat to the neighboring structures. Note that connections to the other parts of the circuit not shown in Figure 3.2 are indicated with component name, volume number, and face number in the form CCCVV000F (CCC for hydrodynamic volume (HV) number, VV for volume number, and F for face number ranging from 1-6) besides each circular node. For example, HV 430 has 12 volumes and is connected to HV 417 at the front and HV 465 at the rear. The pipe receives input from 417010002 (HV 417, volume 1, face 2) sends its output to 465010001 (HV 465, volume 1, face 1). In this work, face 1 of a pipe/single volume/time-dependent volume is used as the inlet and face 2 is used as the outlet.

Table 4.1 presents the pressures and temperatures set for the TDVs. These are our boundary conditions and are either set slightly higher or less than the required pressures. Table 4.2 presents the mass flows of the TDJs connected to the various TDVs.

Table 4.1 Record of pressures and temperatures for time-dependent volumes

HV #	Pressure (MPa)	Temperature (K)
110	7.0	28.78
210	7.0	28.78
310	7.0	28.78
510	6.3	28.78
495	3.15	28.78

Table 4.2 Record of mass flows from TDVs

Starting TDV HV#	Mass flow rate through TDJ (kg/s)
110	13.25
210	0.41
310	0.41
510	4.54

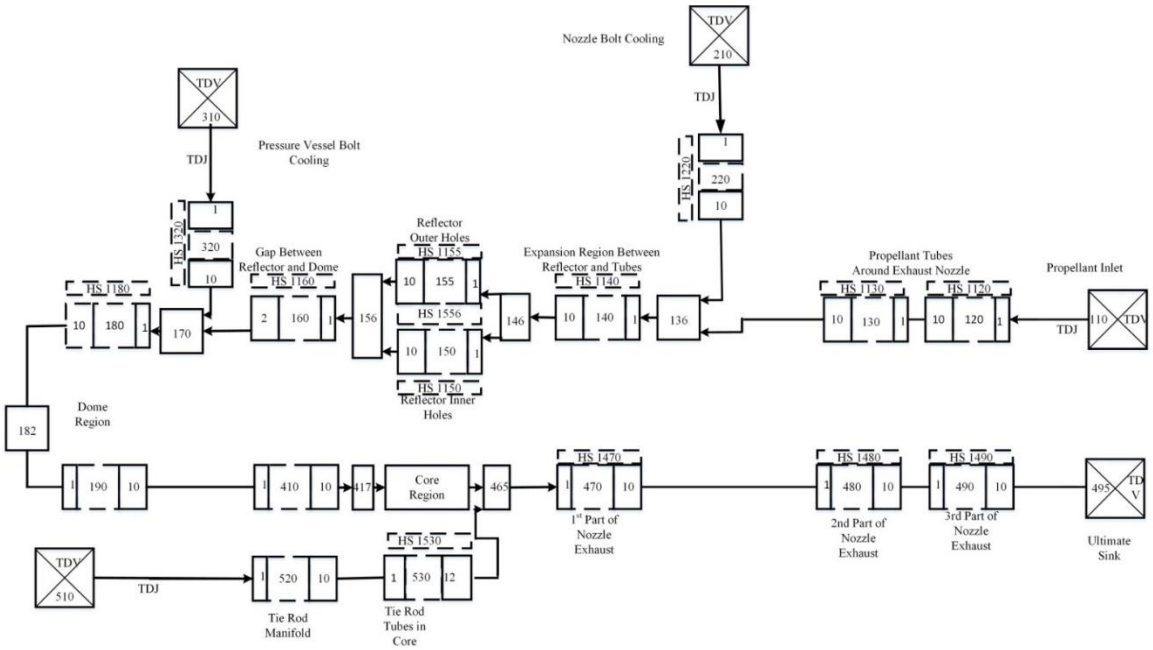

Figure 4.1 Overall RELAP5 nodalization diagram of the Pewee I

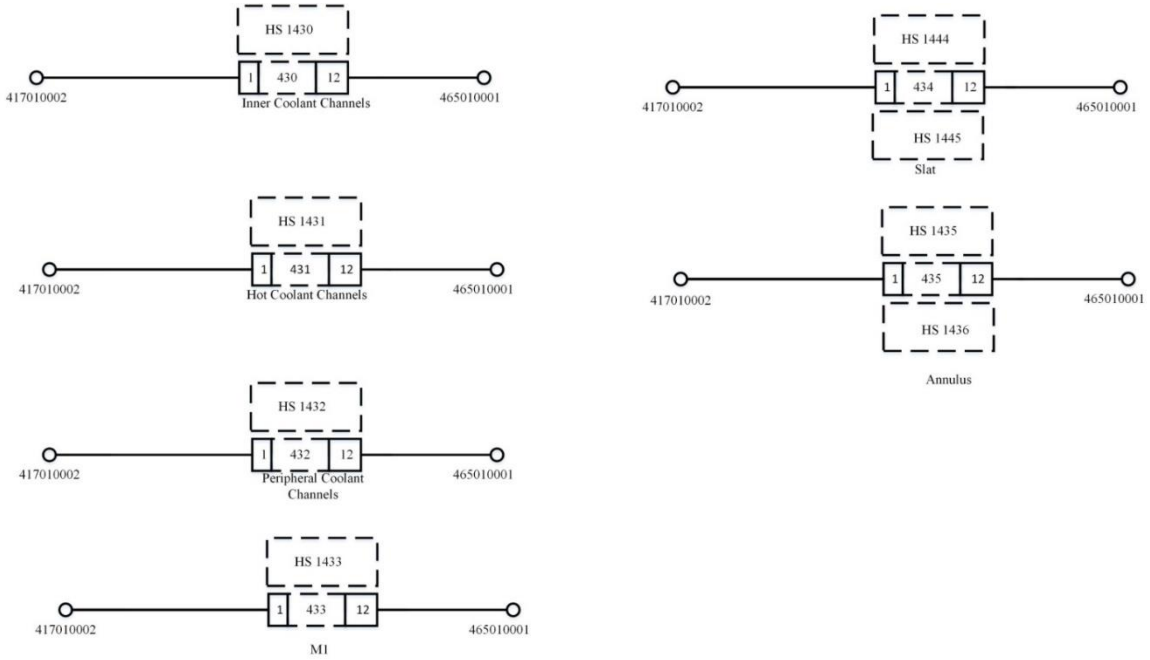

Figure 4.2 Pewee I detailed nodalization diagram of core/bypass components

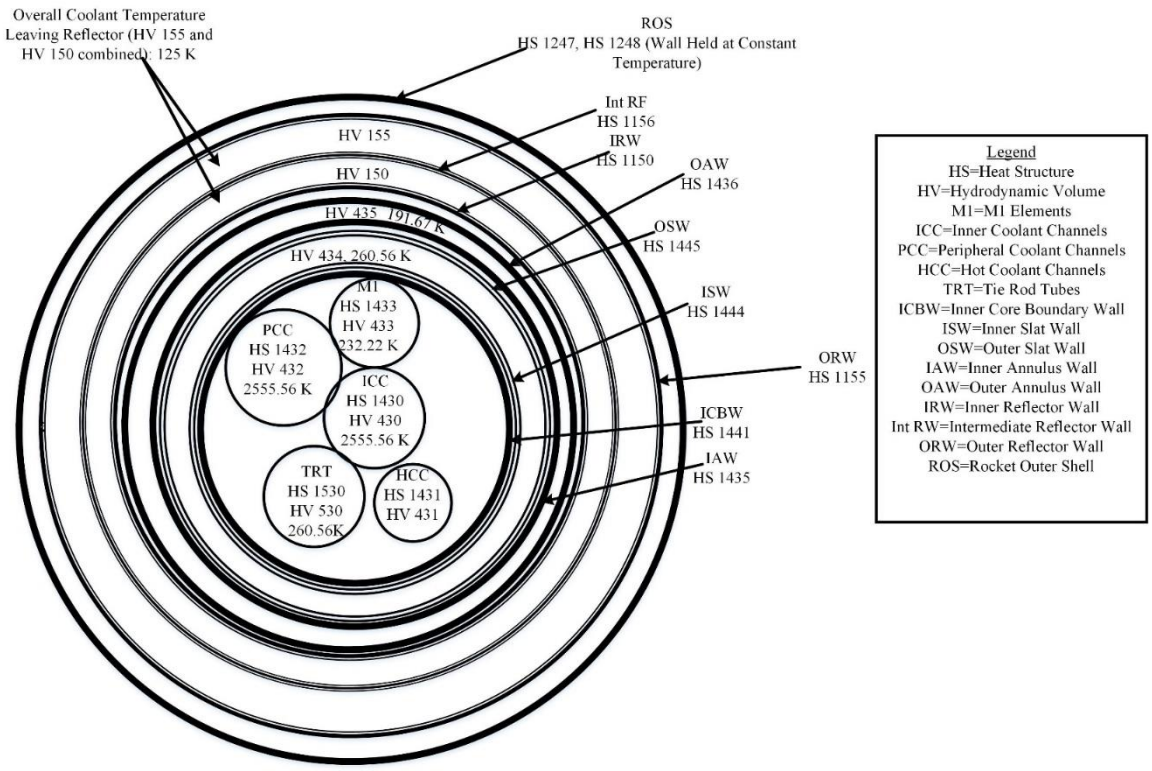

Figure 4.3 Pewee I radial nodalization diagram of core/reflector region

Figures 4.1-4.3 show several heat structures. In particular, heat structure (HS) 1430, 1431, and 1432 are generating heat; HS 1433, 1530, 1435, 1441, 1155, 1444, 1445, 1436, 1150, and 1156 are removing heat. For heat sinks, HS 1247 and 1248 are on the outer shell of the rocket. Adding a heat structure to a hydrodynamic volume basically means adding a wall of certain thickness and material in around the hydrodynamic volume. The outside environments/surroundings of HS 1247 and 1248 are held at space temperatures of 3 K. Note that heat is transferred radially, as the center of the core is the hottest and the temperature at the rocket shell is the coldest. To model the heat transfer from the rocket nozzle to the 120 propellant tubes and the expansion region, the following structures are designated for this: HS 1470, 1480, and 1490. For example, HS 1470 serves as a link between HV 140 and HV 470, HS 1480 serves as a link between HV 130 and HV 480, and HS 1490 serves as a link between HV 120 and HV 490.

RELAP5 heat structures require that material properties such as volumetric heat capacities and thermal heat conductivities be presented. By default, RELAP5 has the property tables for following materials: gap, carbon steel, stainless steel, uranium dioxide, and zircaloy. In our case, the volumetric heat capacities and thermal conductivities were used for uranium carbide, graphite, beryllium, zirconium hydride, zirconium carbide, aluminum, stainless steel, invar and gap. Wherever deemed necessary, the properties were extrapolated to cover a temperature range of 0 K to 5000 K.

In order to get the correct temperatures in the core and reflector region, we have applied the conduction model that comes with RELAP5. RELAP5 requires that two surfaces (represented by heat structures) in conduction follow the trivial relationship

$$C_1 S_1 F_1 = C_2 S_2 F_2 , \qquad (4.1)$$

where the *C's* represent conductances, *S's* represent surface areas, and *F*'s represent area factors and subscripts 1 and 2 denote surfaces 1 and 2. RELAP5 automatically calculates the surface area of each heat structure. The values of *C*'s and *F*'s need to be adjusted in order to get the desired temperatures. As for tuning the temperatures in the nozzle inlet and propellant inlet sections, the fouling factors of the heat structures were adjusted.

Figure 2.1 has most of the information required to do the pressure tuning. The pressure of 3.26 MPa leaving the nozzle exit wasn't provided in the original LASL report. For this case, we ended up estimating the pressure drop through the nozzle using the following pressure drop relation (Todreas & Kazimi, 2012)

$$\Delta P_{total} = \Delta P_{form} + \Delta P_{acc} + \Delta P_{fric} , \qquad (4.2)$$

where ΔP_{form} represents the losses due to form and is given by

$$\Delta P_{form} = K_{cont} \rho \frac{v_2^{\,2}}{2} , \qquad (4.3)$$

ΔP_{acc} represents the losses due to acceleration and is given by

$$\Delta P_{acc} = \rho \frac{v_2^{\,2} - v_1^{\,2}}{2} , \qquad (4.4)$$

and ΔP_{fric} represents the losses due to friction and is given by

$$\Delta P_{fric} = \frac{f \rho v_{pipe}^2 L}{2 D_h} . \qquad (4.5)$$

Also relevant to Equations (4.3)-(4.5), K_c is the contraction coefficient, ρ is the fluid density, v_1 is the fluid velocity upstream, v_2 is the fluid velocity downstream, f is the friction factor in the duct, L is the length of the pipe, v_{pipe} is the fluid velocity in the pipe, and D_h is the hydraulic diameter.

Upon using these relations, a pressure drop of 1.025 MPa was calculated. This means the pressure leaving the nozzle exit and entering into the atmosphere is 3.257 MPa. The pressure drops throughout the rocket were tuned by adjusting the roughness coefficients and the forward and reverse Reynolds loss coefficients. The hydraulic diameter of all pipes was calculated and was required in order to help tune the pressures.

4.3 Validation of the steady-state model

In order to achieve the steady-state results, the RELAP5 input deck was run on "stdy-st" mode for a defined problem time of 1000 seconds. The computer processing time for the simulation depends on the time-step that RELAP5 is able to handle for that particular input deck. In this case, the computer took 29.5 hours to run through the whole problem with a time-step size of 6.0E-5 seconds. In this section, we present our attempts to tune the RELAP5 model. Table 4.3 presents some sample tuned parameters and Figure 4.4 presents a plot of the temperatures reaching steady-state within 1000 seconds.

Table 4.3 Sample tuned parameters

Component	Mass flow rate (kg/s) **(designed value)**	Temperature (K) **(designed value)**	Pressure (MPa) **(designed value)**
Reflector exit	13.65 **(13.65)**	126.27 **(125.00)**	5.58 **(5.71)**
Core inlet	14.06 **(14.06)**	118.50 **(127.78)**	5.44 **(5.56)**
Nozzle exhaust inlet	18.60 **(18.59)**	1767.08 **(1755.23)**	4.19 **(4.28)**
Fuel element exit (includes ICC, HCC, PCC)	11.86 **(12.13)**	2619.53 **(2555.56)**	4.19 **(4.28)**

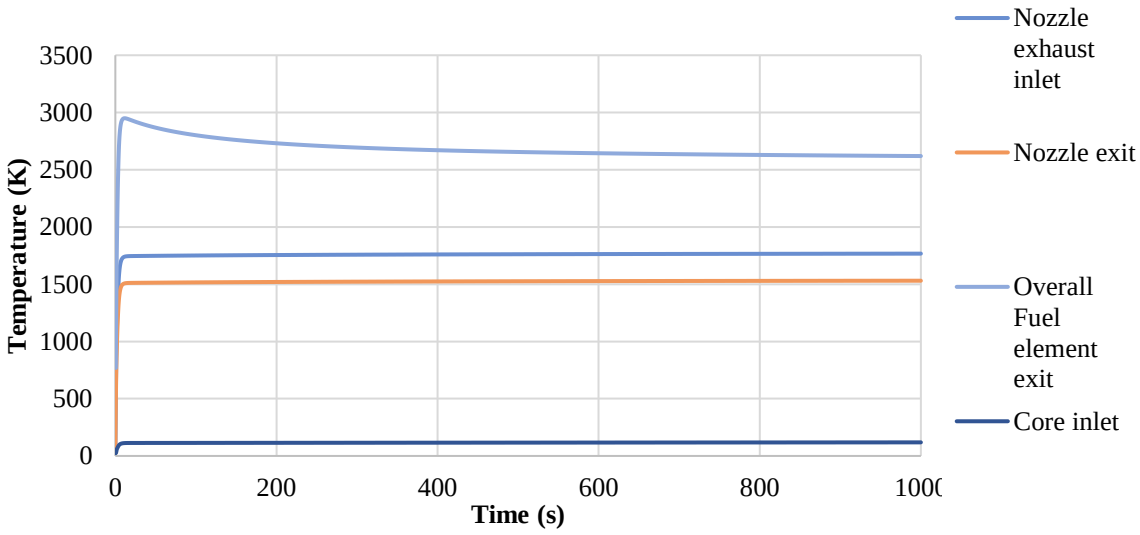

Figure 4.4 Temperatures in the Pewee steady-state model

4.4 Incorporation of radiation heat transfer modeling in Pewee I

As discussed in section 4, the temperature in the Pewee core was tuned by invoking the conduction models. The same input deck was taken and a radiation heat transfer model was incorporated in order to measure the impact of corrosion on radiation heat transfer. A fresh

emissivity coefficient for the fuel element coolant channels was defined. It was assumed that the weight fraction of the NbC is 40% and the weight fraction of the graphite is 60%. Using the fresh and uncorroded emissivity coefficients defined in Table 3.3 and utilizing Equation (3.7), the fresh emissivity of the coolant channel is given by

$$\varepsilon = (0.4)0.79 + (0.6)0.49 = 0.61.$$

Similar to Equation (4.1), the radiation heat transfer model in RELAP5 requires that

$$\varepsilon_1 S_1 V_1 = \varepsilon_2 S_2 V_2, \qquad (4.6)$$

where the ε terms represent emissivity, S terms represent surface areas, V terms represent view factors and numbers 1 and 2 denote surfaces 1 and 2. RELAP5 also requires that the view factors of each surface radiating on other surfaces sum up to 1.0.

4.5. Implementation of radiation heat transfer in Pewee I

In order to do the transient runs measure radiation heat transfer, we need to run steady-state input decks with both conduction and radiation heat transfer models. The selected emissivity coefficients were as follows: 0.61 (fresh case), 0.66 (1st corroded case from Table 3.3), and 0.75 (2nd corroded case from Table 3.3). Figure 4.5 presents some sample temperatures from these steady-state runs.

In each of these runs, the pressure and temperature profile of the Pewee core region were adjusted slightly different from the results presented in section 4.3, as a result of the emissivity coefficients. Table 4.4 presents the major temperatures, temperature rises, and pressure drops as a result of adding the radiation heat transfer models.

Table 4.4 Core temperature results for steady-state runs with emissivity of 0.61

	Emissivity of 0.61	Emissivity of 0.66	Emissivity of 0.75
Coolant temperature (K) exiting fuel elements	2742.59	2739.35	2733.00
Overall coolant temperature (K) entering nozzle exhaust	1780.10	1780.04	1779.78
Rise in temperature (K) across fuel elements	2610.87	2607.70	2602.28
Pressure drop in ICC (MPa)	1.33	1.33	1.34
Pressure drop in HCC (MPa)	1.14	1.14	1.14
Pressure drop in PCC (MPa)	1.14	1.14	1.14

From Table 4.4, the temperature rise across the fuel elements decreases with increasing emissivity. However, there isn't any significant change in the pressure drop at the various emissivity levels. In Table 4.5, we present the radiation heat transfer rates between each of the fuel elements and the cold surfaces they radiate with. As expected, the radiation heat transfer from each of the fuel element channels increases with increasing emissivity.

Table 4.5 Record of radiation heat transfer from fuel elements

Particulars	Emissivity of 0.61	Emissivity of 0.66	Emissivity of 0.75
Radiation heat transfer rate between ICC and cold surfaces (W)	3.40E+06	3.68E+06	4.19E+06
Radiation heat transfer rate between HCC and cold surfaces (W)	3.51E+05	3.53E+05	3.56E+05
Radiation heat transfer rate between PCC and cold surfaces (W)	2.55E+06	2.65E+06	2.81E+06
Total radiation heat transfer rate (W)	6.29E+06	6.68E+06	7.35E+06

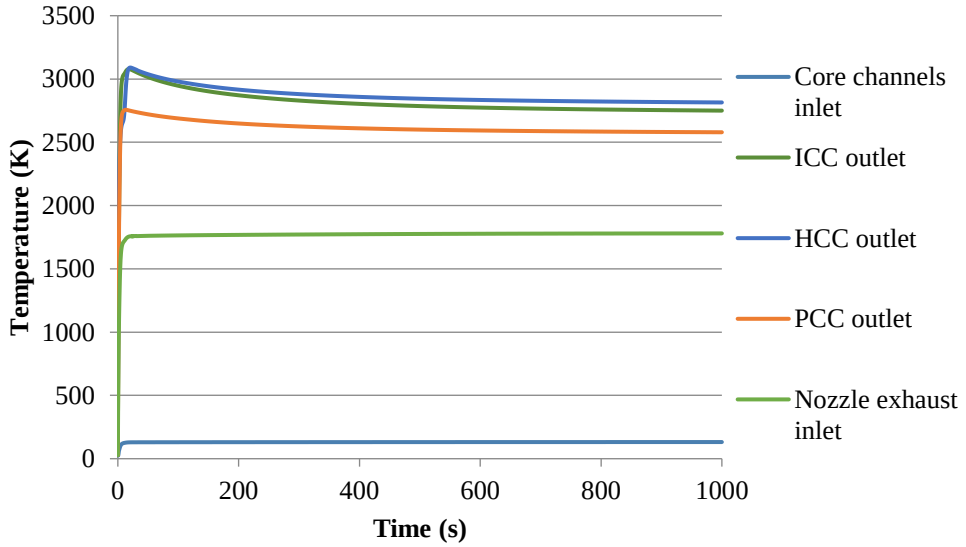

Figure 4.5 Temperatures in the Pewee steady-state model (HCC, ICC, and PCC have surface emissivity of 0.61)

CHAPTER 5: MODELING OF CORROSION-INDUCED BLOCKAGES ON RADIATION HEAT TRANSFER BY USING RELAP5-3D

5.1 Introduction

According to Akyuzlu (2015), degradation of fuel elements occurs due to significant temperatures at the fuel surface. There are several factors that contribute to the degradation of the fuel element. Examples of these factors include: "(i) melting of the fuel, (ii) vaporization/ sublimation, (iii) creep of material cracks, (iv) corrosion, and (v) structural degradation" (Akyuzlu, 2015). At present, work concerning the use of RELAP5 for modeling and testing transients on NTRs is limited. Experiments or simulations that test corrosion-induced blockages on fuel element coolant channels are also limited. The purpose of this chapter is to model corrosion-induced blockages on the NTR. As mentioned in chapter 3, the Pewee experiments showed that the peripheral fuel elements had suffered extensive corrosion. Hence, in this chapter, we are investigating transients where the PCC undergo flow area reduction due to corrosion-induced blockages. The blockages were assumed to occur at the start of the fuel element. Blockages are being studied because they can cause fuel elements to exceed the melting point temperature.

5.2 Modeling of the corrosion-induced blockages

The transient runs were done on the completed steady-state runs presented in section 4.5 (see Table 4.4, Table 4.5, and Figure 4.5) with the various emissivity coefficients. In order to do a transient run in RELAP5, a RESTART problem is initiated and the simulation starts from the end-time of the steady-state run. In most cases, the RESTART problem can be run at the same time step as the steady-state run. In order to model the blockages, a motor valve (see Figure 5.1) was added at the start of the PCC (HV 432 in Figure 4.2) and the opening percentage was defined. For example, a valve 10% open refers to a 90% blockage. Here, the RESTART problems were run for 3000 seconds each. Table 5.1 presents several cases of transients that were investigated.

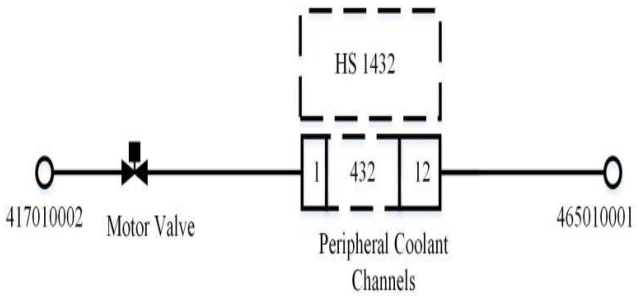

Figure 5.1 Motor valve attached in front of PCC

Table 5.1 Summary of transient cases considered

Case ID	Emissivity	Valve opening (%)	Blockage (%)	Description of case
1 (a)	0.61	10	90	Fresh surface with extremely high blockage
1 (b)	0.61	15	85	Fresh surface with very high blockage
1 (c)	0.61	30	70	Fresh surface with high blockage
1 (d)	0.61	100	0	Fresh surface with no blockage
2 (a)	0.66	10	90	Corroded surface with extremely high blockage
2 (b)	0.66	15	85	Corroded surface with very high blockage
2 (c)	0.66	30	70	Corroded surface with high blockage
2 (d)	0.66	100	0	Corroded surface with no blockage
3 (a)	0.75	10	90	More corroded surface with extremely high blockage
3 (b)	0.75	15	85	More corroded surface with very high blockage
3 (c)	0.75	30	70	More corroded surface with high blockage
3 (d)	0.75	100	0	More corroded surface with no blockage

Upon completion of the runs, data concerning the temperatures and pressures were noted. Figures 5.2 show the coolant temperatures exiting PCC for each of the cases. As expected for each of the transient cases, the temperature of the coolant exiting PCC is greatest for Case 1(a), Case 2(a), and Case 3(a)-all of these have blockage ratios of 90%. Notice that all the curves can be arranged in groups of Case (a)s, Case (b)s, and Case (c)s. When comparing the exiting temperatures, all the Cases 3(a)-3(d) have a set of lower temperature curves due to their higher surface emissivity

coefficients. In addition, Case 1(a)-1(d) have a set of higher temperature curves due to their lower surface emissivity coefficients.

Table 5.2 presents a summary of the temperature rise and pressure drop for each of the cases. In Table 5.2, the temperature rise across the PCC is greatest for Case 1(a), Case 2(a), and Case 3(a). However, with higher levels of corrosion (i.e. higher emissivity coefficients) and at the same blockage ratio, the temperature rise is less. For example, Case 3(a) (emissivity of 0.75 and blockage of 90%) has a temperature rise of 2591.49 K as opposed to 2624.34 K of Case 2(a) (emissivity of 0.66 and blockage of 90%). The pressure drop in PCC for Case 1(a), Case 2(a), and Case 3(a) is the greatest and is also the same for each of these three cases. Hence, we can concur that there is minimal difference in the pressure drop due to the emissivity coefficients. Instead, the differences in pressure drop for all the cases are due to the blockage ratio.

Table 5.2 Temperature rise and pressure drop from transient cases

Case ID	Temperature rise across PCC (K)	Pressure drop across PCC (MPa)
1 (a)	2644.71	1.19
1 (b)	2530.76	1.17
1 (c)	2447.35	1.16
1 (d)	2424.35	1.16
2 (a)	2624.34	1.19
2 (b)	2513.29	1.17
2 (c)	2431.92	1.16
2 (d)	2409.83	1.16
3 (a)	2591.49	1.19
3 (b)	2484.95	1.18
3 (c)	2406.70	1.16
3 (d)	2386.07	1.16

Table 5.3 presents the radiation heat transfer rates from a few of the selected cases. In Table 5.3, the ICC and HCC didn't undergo blockages. It is noted that the radiation heat transfer rate between these channels and the nearby cold surfaces is less when PCC is undergoing a blockage (i.e. compare Case 3(d) to Case 3 (a), Case 2(d) to Case 2(a), Case 1(d) to Case 1(a), etc). However, at each of the emissivity coefficients, the radiation heat transfer from PCC is greatest when PCC is undergoing a blockage. In particular, Case 3(a) (emissivity of 0.75 and blockage ratio of 90%) shows the highest radiation heat transfer rate between PCC and neighboring cold surfaces. This shows that the blockage of PCC impacts the radiation heat transfer of itself and the neighboring unblocked channels. Overall, the total radiation heat transfer from all fuel element coolant channels (ICC, HCC, PCC) is greatest for Case 3(a).

Table 5.3 Radiation heat transfer rates from transient cases

Case ID	Radiation heat transfer rate between ICC and cold surfaces (W)	Radiation heat transfer rate between PCC and cold surfaces (W)	Radiation heat transfer rate between HCC and cold surfaces (W)	Total radiation heat transfer between fuel elements and cold surfaces (W)
1(a)	3058417.8	3514919	347237	6920574
1(d)	3177064.4	2453913	348572	5979549
2(a)	3323085.9	3635361	349337	7307784
2(d)	3447302.8	2552037	350580	6349920
3(a)	3784119.7	3830869	352604	7967593
3(d)	3925168	2713027	353665	6991860

Figure 5.3 presents the final coolant temperature exiting PCC with respect to blockage ratio. This figure is an alternative representation of Figure 5.2. In either case, it shows the differences in temperature results caused by the emissivity coefficients. The cases with the lower emissivity of 0.61 have higher temperatures than those with higher emissivity coefficients.

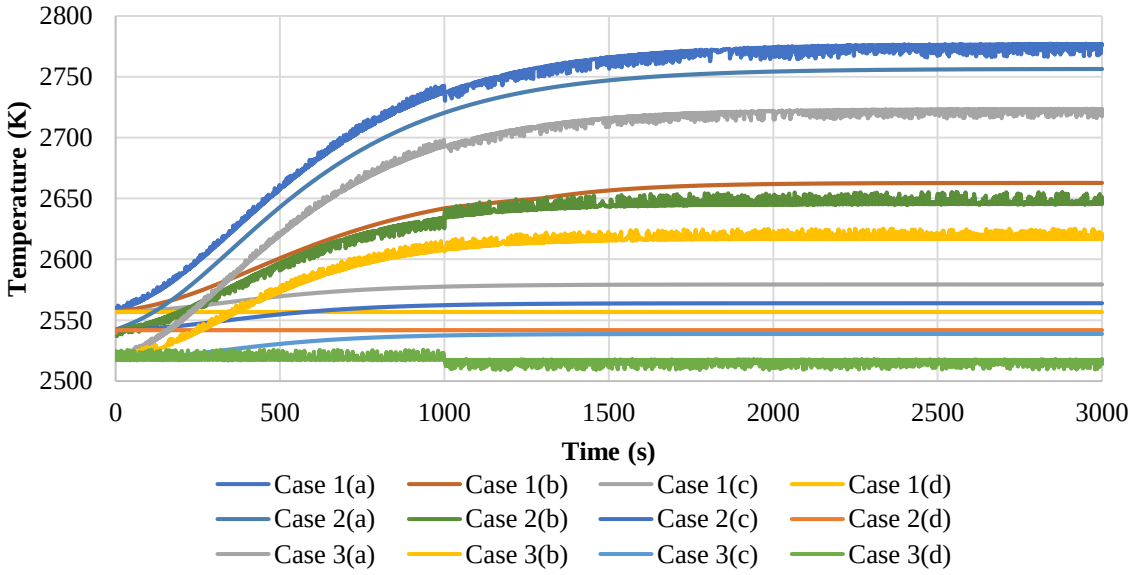

Figure 5.2 Coolant temperature exiting PCC (all surface emissivity coefficients)

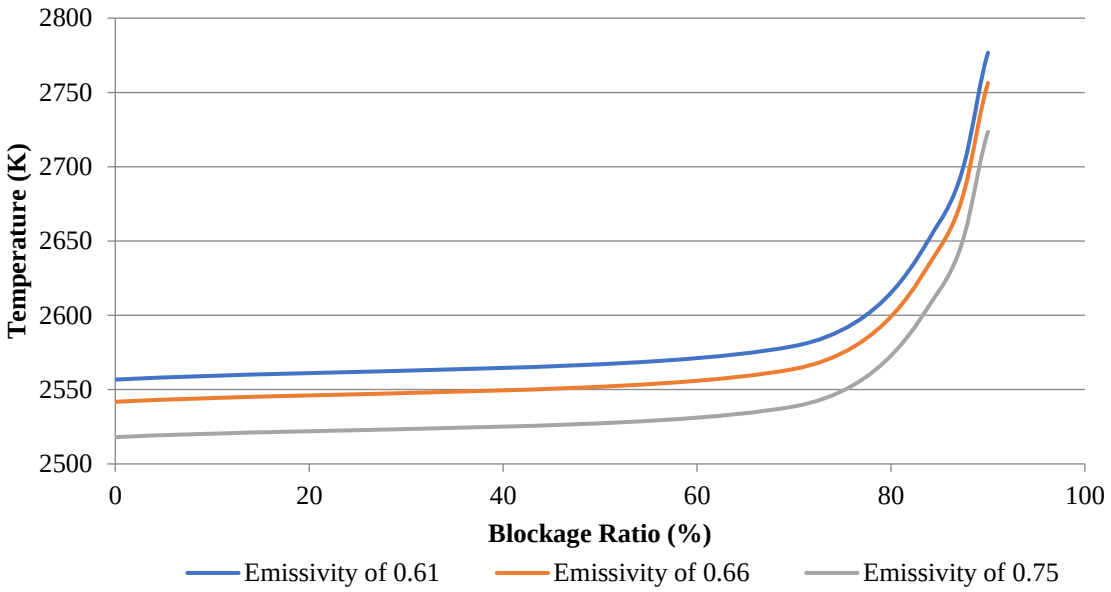

Figure 5.3 Coolant temperature exiting PCC vs blockage ratio

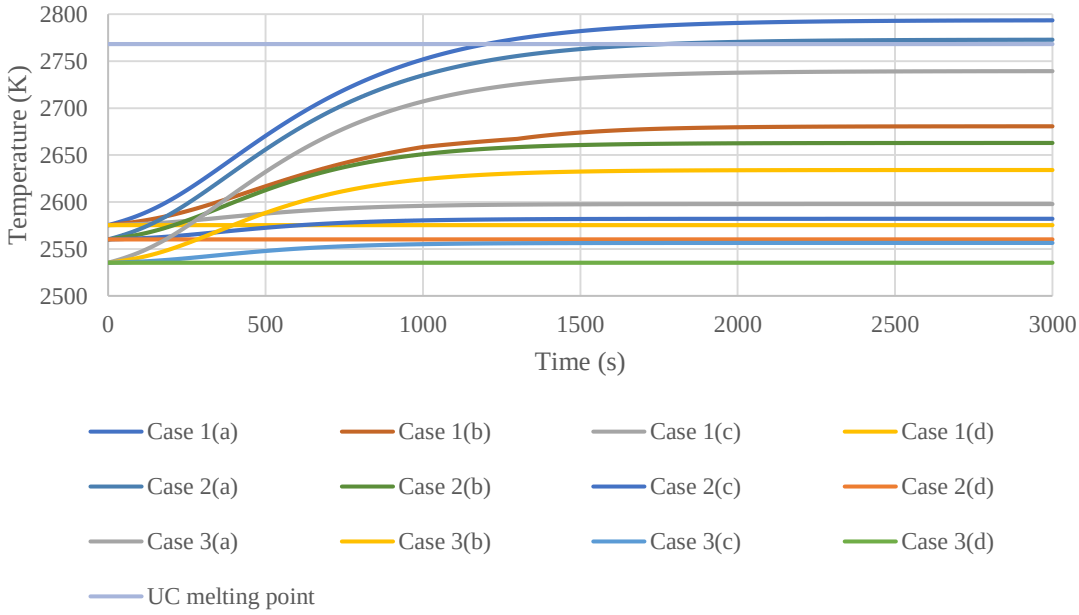

Figure 5.4 PCC fuel element temperature

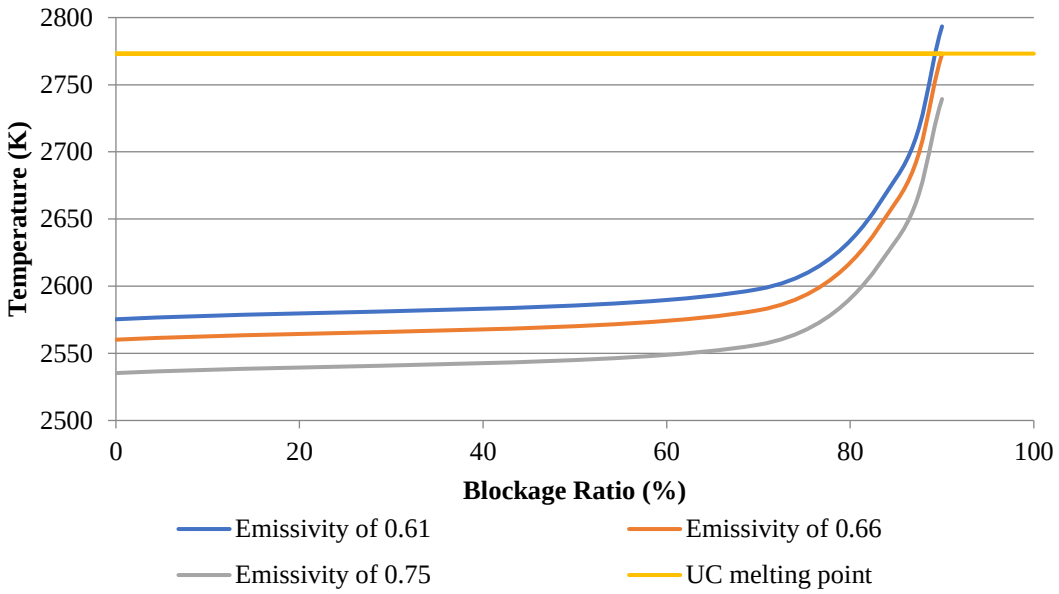

Figure 5.5 PCC fuel element temperature vs blockage ratio

Figure 5.4 presents the fuel element temperature of PCC with respect to time. Figure 5.5 presents the fuel element temperatures of PCC with respect to blockage ratio and compares them to the melting point of UC. As per expectation, these curves show the same trends as those visible in Figures 5.2-5.3. Figures 5.4-5.5 demonstrate that the fuel element temperature is gradually rising and will at some point exceed the melting point of UC, which is 2768.15 K (Jones & Crosthwaite, 1973). The melting points of graphite, NbC and ZrC are 3773.15 K (Entegris, 2013), 3795.15 K (Woydt & Mohrbacher, 2014) and 3303-3530 K (AZO Materials, 2016), respectively. The NASA Mars missions, proposed for the 2030s, require an NTR operation time of 2 hours when operated at full power (Nam et al, 2015). The longest engine burn time is 50 minutes (Nam et al, 2015). The approximate travel time between Earth and Mars is 100 days (Zolfagharifard, 2016). However, the reactor will not operate for 100 days continuously. Instead, the reactor will operate momentarily for 2 hours, such that the rocket gains speed and coasts naturally in space. Every time the rocket needs to pick up more speed or change directions, the reactor will operate again. Hence, assuming the Pewee I is operating at full power and deployed for the NASA Mars mission, the action necessary to counteract corrosion-induced blockages needs to be defined. From Figure 5.5, blockages on the PCC of 90% will cause the fuel element temperatures to eventually exceed the melting point. This calls for the need of a detection system that will notify the crew when fuel elements temperatures are nearing the melting point. Provided the pump is providing the required mass flow rate, such a situation may be averted by ramping the power down. The rocket may operate at a lower thermal power, but still enough to provide a sufficient thrust. A means to reduce the probability of corrosion-

induced blockages in the PCC is to redesign the fuel elements. Perhaps, the PCC holes can be redesigned with a greater flow area, hence reducing the probability of blockages. Alternatively, fuel elements made from materials instead of UC could also be investigated.

5.3 Conclusions

In this chapter, corrosion-induced blockages in the Pewee fuel elements were modeled using RELAP5-3D. The blockages were assumed to occur at the inlet of the peripheral coolant channels. Transients with blockages of 90%, 85%, 70%, and 0% with different emissivity coefficients were considered. For the most severe blockage considered (90% blockage), both the temperature rise and the pressure drop through the peripheral coolant channels were the greatest at each of the emissivity coefficients. With higher emissivity coefficients, the temperature rise through the peripheral coolant channels decreases and so does the coolant temperature exiting these same channels. When peripheral coolant channels undergo blockages, its radiation heat transfer increases while the radiation heat transfer of other fuel element channels (hot coolant channels and inner coolant channels) decreases. In general, more corrosion corresponds to greater emissivity, which yields higher radiation heat transfer rates. Increasing radiation heat transfer decreases the temperature of the fuel elements and the coolant.

CHAPTER 6: MODELING LOSS-OF-FLOW-ACCIDENTS AND THEIR IMPACT ON RADIATION HEAT TRANSFER

6.1 Introduction

The purpose of this chapter is to investigate the impact of loss-of-flow-accident (LOFA) on the radiation heat transfer in the core. As demonstrated in the introduction, this is a behavior that hasn't been studied. In addition, the impact on the fuel element temperature and the pressure profile in the core will also be noted. Here, it is assumed that the LOFA has occurred due to the reactor pump failure.

6.2 System response of Pewee due to loss-of-flow-accidents

The transient runs were initiated on the completed steady-state runs presented in chapter 4 (see Table 4.4, Table 4.5, and Figure 4.5). As mentioned in chapter 5, transient runs in RELAP5 require a RESTART problem to be resumed from the end-time of the steady-state run. At a time of 501 seconds from the start of the RESTART problem, the mass flow rate going through the system was decreased. The simulation was run for a total of 3501 seconds. A summary of the events is provided in Table 6.1. Table 6.2 presents a summary of the transient cases. In Table 6.2, an emissivity coefficient of 0.61 is designated for a fresh surface with no corrosion (see chapter 4 where Equation (3.7) is used to calculate this). Emissivity coefficients of 0.66 and 0.75 have corrosion (see Table 3.3). Basically, Case 1(a), Case 2(a), and Case 3 (a) are cases with a complete LOFA and Case 1(d), Case 2(d), and Case 3(d) are cases with no LOFA. Cases (b) and (c) have partial LOFAs.

Table 6.1 Events scheduled for the RESTART problem

Time (s)	Event
0	RESTART problem resumes
501	Flow rate throughout system is decreased
3501	RESTART problem ends

Figure 6.1 presents the mass flow rates resulting from the LOFAs. Figure 6.2 presents the average pressure in the core for Cases 1(a)-1(d). From Figure 6.1, the rapid change in mass flow rate is noticed. Figure 6.2 shows a similar shape to Figure 6.1. Table 6.3 presents the average pressure in the core for all these cases. Here, the average pressure level in the core for Cases 1(a)-1(d) shows similarities to Cases 2(a)-2(d) and Cases 3(a)-3(d).

Table 6.2 Summary of transient cases considered

Case ID	FE channel emissivity	Flow rate (%) of original	Description of case
1 (a)	0.61	0	Fresh surface, complete LOFA
1 (b)	0.61	75	Fresh surface, 2nd partial LOFA
1 (c)	0.61	90	Fresh surface, 1st partial LOFA
1 (d)	0.61	100	Fresh surface, No LOFA
2 (a)	0.66	0	Corroded surface, complete LOFA
2 (b)	0.66	75	Corroded surface, 2nd partial LOFA
2 (c)	0.66	90	Corroded surface, 1st partial LOFA
2 (d)	0.66	100	Corroded surface, No LOFA
3 (a)	0.75	0	Very corroded surface, complete LOFA
3 (b)	0.75	75	Very corroded surface, 2nd partial LOFA
3 (c)	0.75	90	Very corroded surface, 1st partial LOFA
3 (d)	0.75	100	Very corroded surface, No LOFA

.

Table 6.3 Average pressure level in the core

Case ID	Average pressure in core (Pa)
1 (a)	3190060
1 (b)	4502540
1 (c)	4750665
1 (d)	4890275
2 (a)	3190155
2 (b)	4503350
2 (c)	4750360
2 (d)	4889500
3 (a)	3190395
3 (b)	4504370
3 (c)	4749755
3 (d)	4888835

Figure 6.3 presents the temperature of the fuel elements and Figure 6.4 presents the material temperature of PCC. In both Figures 6.3-6.4, the melting point of UC, which is 2768.15 K, is included in the plots (Jones & Crosthwaite, 1973). Figure 6.3 shows that many of the curves overlap with each other. In particular, all the Case (a)s are clumped together, all the Case (b)s are clumped together, all the Case (c)s are clumped together, and all the Case (d)s are clumped together. Table 6.4 presents the radiation heat transfer from the fuel elements to the cold surfaces. Generally, the radiation heat transfer rate increases as the flow rate through the reactor system is decreased. This trend is noted in the results of the Case (b)s, Case (c)s, and Case (d)s. However, the radiation heat transfer rate drops when there is a complete LOFA, as witnessed in the results of all Case (a)s. This is due to the fact that the higher fuel element temperatures are also heating up the cold structures adjacent to them. This reduces the $\left(T_{hot}^4 - T_{cold}^4\right)$ difference between the hot and cold surfaces, which then leads to reduced radiation heat transfer rates.

Figure 6.4 very clearly shows the differences caused by the emissivity coefficients on the PCC material temperatures, more so than Figure 6.3. The top 3 curves in Figure 6.4 belong to Case 1(a), Case 2(a), and Case 3(a). Since Case 3(a) has the highest emissivity among the three, the temperature here is less. Case 1(a) has the lowest emissivity among the three and therefore has the highest temperature.

Table 6.4 Radiation heat transfer rates from transient cases

Case ID	Radiation heat transfer rate between fuel elements and cold surfaces (W)	Radiation heat transfer rate as percentage of power generated in fuel elements
1 (a)	6.63E+6	1.44
1 (b)	3.45E+7	7.47
1 (c)	2.06E+7	4.47
1 (d)	1.51E+7	3.27
2 (a)	6.76E+6	1.46
2 (b)	3.66E+7	7.92
2 (c)	2.19E+7	4.75
2 (d)	1.60E+7	3.48
3 (a)	6.94E+6	1.50
3 (b)	4.01E+7	8.68
3 (c)	2.42E+7	5.24
3 (d)	1.77E+7	3.84

From Table 6.5, the radiation heat transfer in the PCC increases with decreasing flow rate. Contrary to Table 6.4, the radiation heat transfer rate in the Case (a)s is greater than Case (d)s. Comparing the radiation heat transfer between identical cases in Table 6.4 and Table 6.5, the Case (a)s have almost the same radiation heat transfer rate. This shows that when there is a complete LOFA, the PCC handles the majority of the radiation heat transfer.

Table 6.5 Radiation heat transfer rates from PCC to cold surfaces

Case ID	Radiation heat transfer rate between PCC and cold surfaces (W)	Radiation heat transfer rate as percentage of power generated in PCC
1 (a)	6.62E+06	28.49
1 (b)	6.25E+06	26.90
1 (c)	4.51E+06	19.42
1 (d)	3.66E+06	15.76
2 (a)	6.75E+06	29.03
2 (b)	6.41E+06	27.55
2 (c)	4.65E+06	20.01
2 (d)	3.79E+06	16.31
3 (a)	6.93E+06	29.82
3 (b)	6.65E+06	28.60
3 (c)	4.90E+06	21.07
3 (d)	4.00E+06	17.18

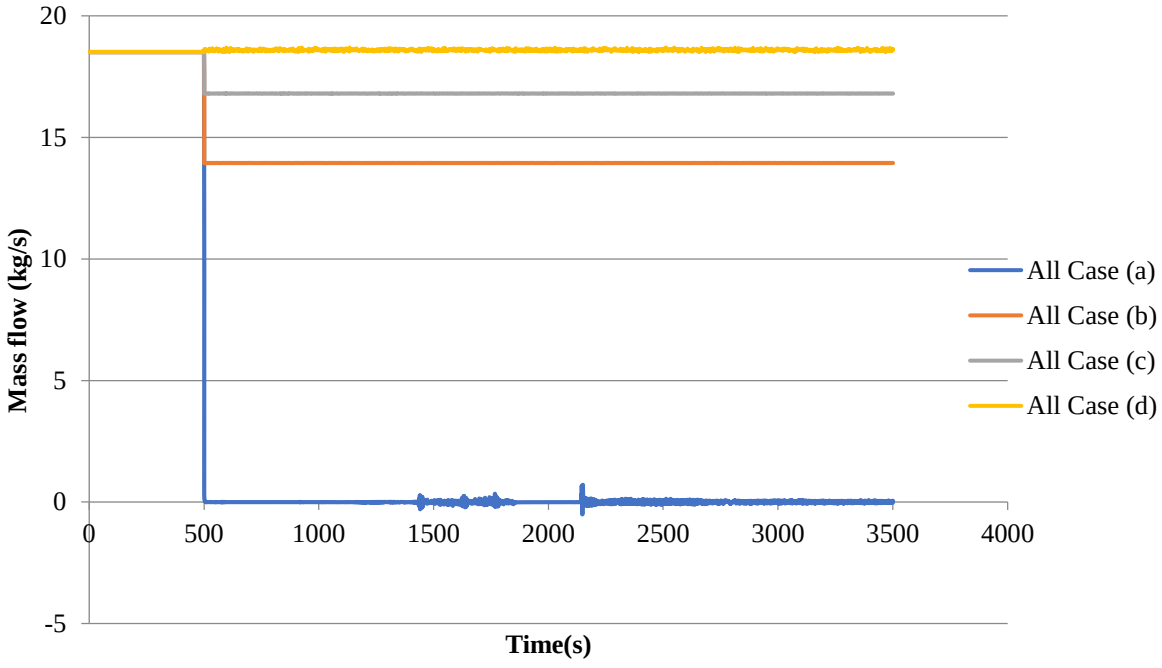

Figure 6.1 Mass flow rates resulting from the LOFAs

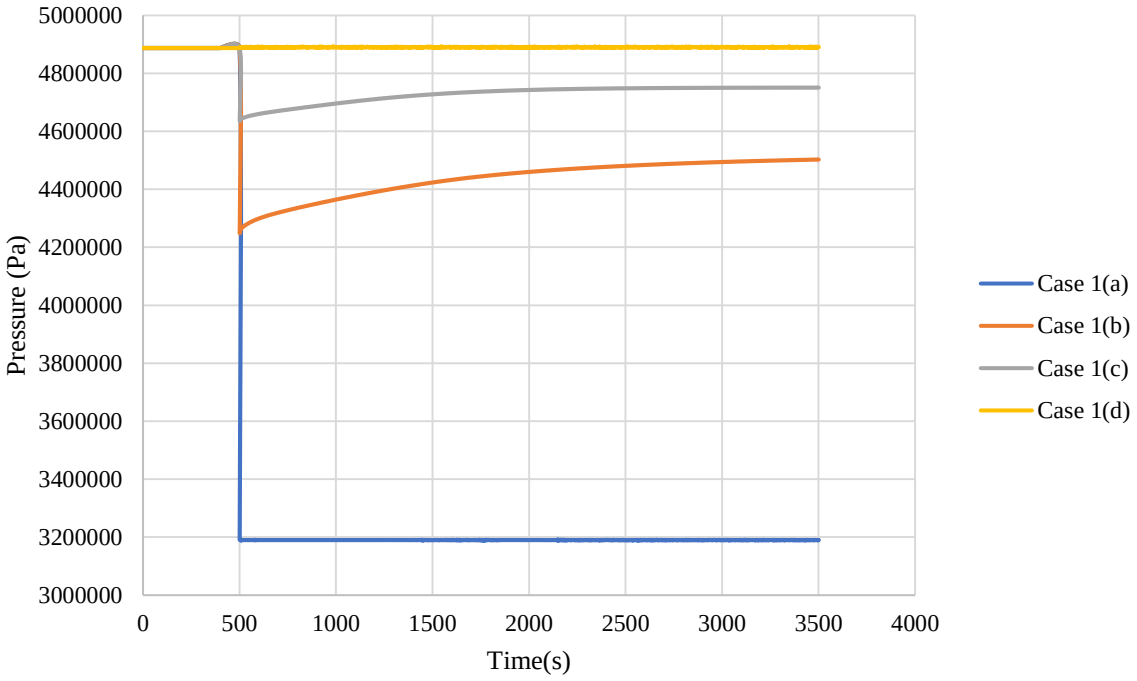

Figure 6.2 Average pressure in the core

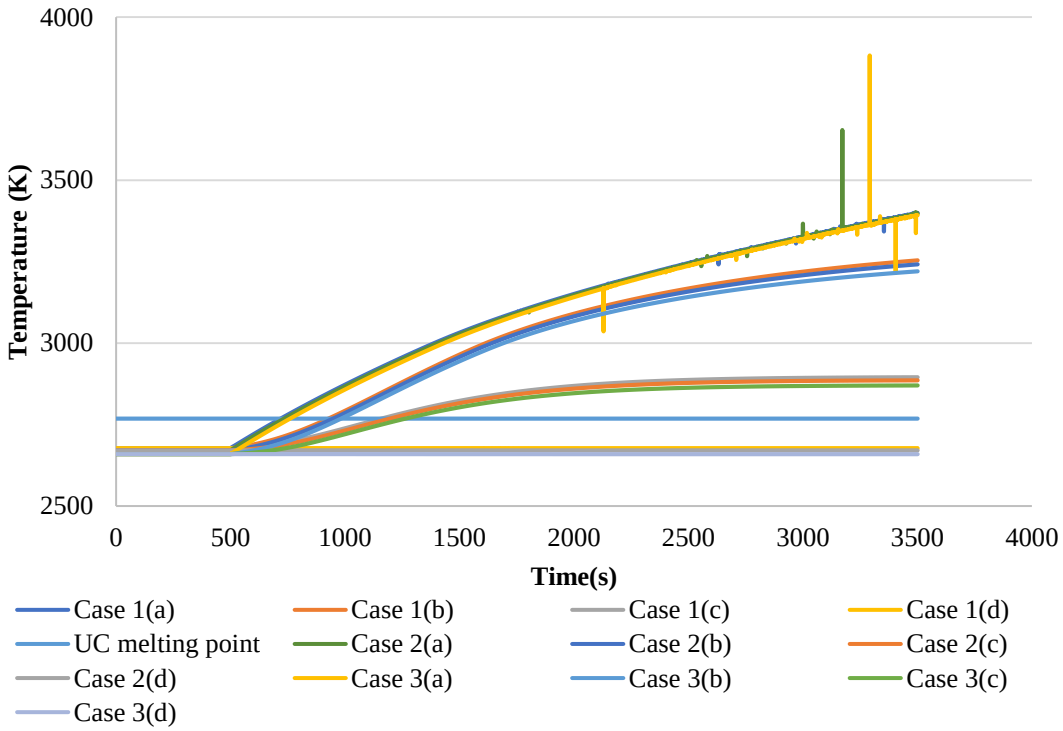

Figure 6.3 Temperature of fuel elements

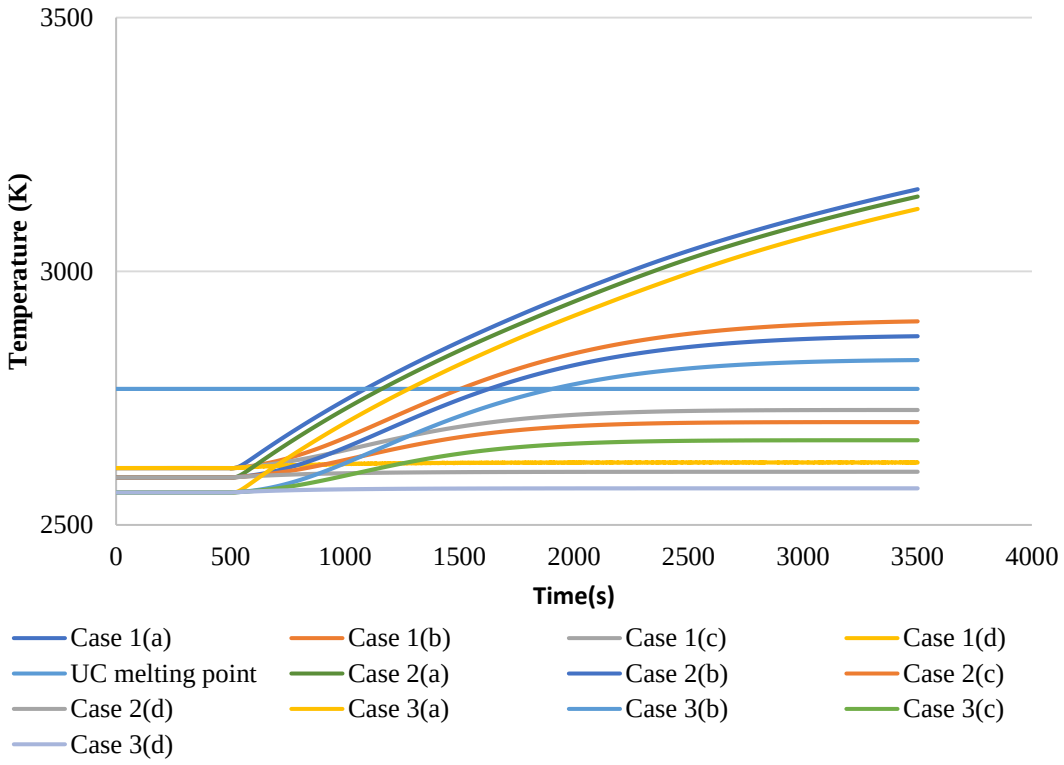

Figure 6.4 Material temperature of PCC

From Figure 6.3, even a flow rate drop by 25% from the original is sufficient to cause the fuel element temperature to exceed the melting point of UC. Also from Figure 6.3, the melting point of UC is also exceeded when the total flow rate drops by 10% from the original. Eventually, the melting points of graphite, NbC, and ZrC will be exceeded. Recall from section 5 that the melting points of graphite, NbC and ZrC are 3773.15 K (Entegris, 2013), 3795.15 K (Woydt & Mohrbacher, 2014) and 3303-3530 K (AZO Materials, 2016), respectively. Assuming the Pewee I is operating at full power and deployed for the NASA Mars mission, an action to counteract LOFA would need to be defined. LOFA can be counteracted by scramming the reactor and then by passing an emergency system coolant to remove the decay heat. This emergency system coolant could operate actively/passively in an open or closed loop.

6.3 Conclusions

The LOFA in the Pewee rocket system has been modeled using RELAP5-3D. First, a steady-state model, presented in chapter 4, was developed to achieve steady-state conditions for the main thermal-hydraulic parameters. Then, transients were done on the steady-state model such that LOFAs were assumed. It was assumed the flow rate dropped by 0%, 10%, 25%, and 100%. The average pressure level in the core decreases as the flow through the reactor is decreased. As expected, a partial or complete LOFA causes the temperature of the fuel elements to become greater

than normal. Even for a flow rate that has been reduced by 10%, the temperature of the fuel elements exceeds the UC melting point. A complete LOFA causes the radiation heat transfer rate between the fuel elements and the cold surfaces to decrease. This is due to the temperatures of the cold surfaces increasing simultaneously with the fuel element temperatures. In addition, the radiation heat transfer between the fuel elements and the cold surfaces during a complete LOFA is governed primarily by the PCC. A safety system will be needed to counteract the decay heat resulting from scamming the reactor post-LOFA.

CHAPTER 7: DESIGN OF A PASSIVE SAFETY SYSTEM FOR THE PEWEE I

7.1 Introduction

Nuclear reactors, especially terrestrial nuclear reactors, have active and passive safety systems. Active safety systems are those that require electric/mechanical inputs or human intervention to operate. Passive safety systems are those that depend on natural processes such as gravity or natural circulation and don't need human intervention or electric/mechanical inputs to run. Modern day boiling water reactors and pressurized water reactors have mostly active safety systems. Many of the proposed Generation III+ reactors, for example, the Westinghouse Advanced Passive 1000 (AP1000), General Electric Economically Simplified Boiling Water Reactor (ESBWR), Molten Salt Reactor (MSR), European Lead-cooled System (ELSY) reactor, High Temperature Gas Reactor (HTGR), and Sodium Advanced Fast Reactor (SAFR) have new passive safety systems. Safety systems that operate in response to an accident have not been designed for nuclear space vehicles. In this chapter, we present the design and testing of a safety system to go with the Pewee I Test Reactor. We have assumed the safety system will act in response to a design basis accident such as a LOFA. In this chapter, the following will be presented: (i) a literature review of safety systems in space nuclear reactors, (ii) a literature review of non-forced circulation systems in space, (iii) a presentation of the safety system design, (iv) modeling of Pewee with safety system in RELAP5, (v) operation of the Pewee I with secondary system in steady-state mode, (vi) operation of the Pewee I with secondary system in response to a transient, and (vii) conclusions to summarize the findings in this chapter.

7.2 Literature review of safety systems in space nuclear reactors

NASA came up with a Mars Design Reference Architecture (DRA) 5.0 study (Borowski, McCurdy, & Packard, 2009). This study investigated the mission, payload, and transportation system requirements for a civilian expedition to Mars, scheduled for the 2030s. In this particular study, they considered a rocket with three NERVA-derived NTR engines, each with a resulting thrust of 111.21 KN (like the Pewee design). The fuel in the core is NERVA-derived/UC-ZrC in graphite "composite". The propellant of this rocket is liquid hydrogen. The core has a propellant exit temperature of 2650-2700 K. The engine chamber pressure is 1000 psi. The nozzle area ratio is 300:1 to 500:1 and the specific impulse is 900-910 seconds. The length of the engine is 7.01 m. The safety system in this spacecraft is not for the purpose of responding to accidents. Rather, it is for the purpose of preventing abnormalities. The safety systems associated with this design involve the multilayer insulation (MLI) that surrounds the liquid hydrogen tanks for passive thermal protection.

The cryogenic tanks are manufactured using aluminum/lithium and have a diameter of 8.2-8.9 m. Typical insulation consists of 1" spray on foam insulation (SOFI) (0.78 kg/m^2) plus 60 layers of MLI (0.90 kg/m^2). The active zero-boiloff (ZBO) cryocooler is used to limit/eradicate boil-off when the propellant tank is exposed to the climate of the planet. The cryocooler is powered by photovoltaic array (PVA) primary power system.

Similar to the design presented by Borowski, McCurdy, and Packard (2009); Christie and Plachta (2006) presented a bimodal NTR (BNTR) design. In addition to thrust, BNTRs also provide electricity for instruments and other systems of the spacecraft. This BNTR design has liquid hydrogen stored in the core stage tank, in-line tank, and four drop tanks. These tanks each have a diameter of 7.5 m. The core stage tank has a length of 20 m, whereas the in-line tanks and drop tanks are each 10 m long. The truss structure, which is composed of 24 struts, connects the walls of the core stage and in-line tanks to the rest of the vehicle. The transhab is an air-inflatable habitat for the crew members to board in during the mission.

The safety systems in this BNTR are similar to those presented by Borowski, McCurdy, and Packard (2009). Here, all the hydrogen storage tanks are surrounded by multilayer insulation (MLI), flexible optical solar reflector (FSOR), and spray-on foam insulation (SOFI). In order of appearance, SOFI is covered by MLI and then covered by FSOR. There are two cryocoolers assigned for the core stage tank and two cryocoolers for the in-line tank. The purpose again is to keep the hydrogen in its liquid state during inter-planetary missions.

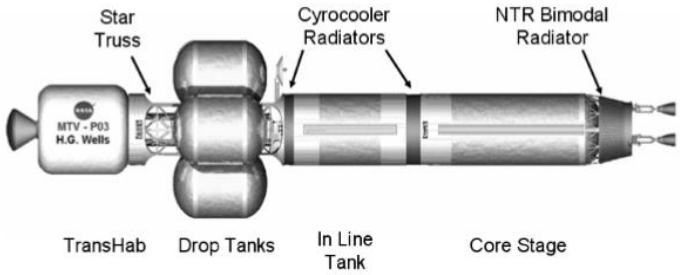

Figure 7.1 Bimodal NTR spacecraft (Christie & Plachta, 2006)

Malloy (1994) designed a passive cooling system for an open cycle nuclear reactor, like those found in nuclear rockets (see Figure 7.2). In this particular design, there are passive coolant tanks, flow rate regulators, and checks valves. During normal operation, propellant flows to the reactor and also to the coolant tanks. When the reactor and pump are shut down, the pressures at each passive coolant tank are greater than the pressure at the reactor inlet. Hence, the coolant is able to flow naturally from the tanks to the reactor inlet. The flow rate regulator determines the flow rate based on decay heat needs.

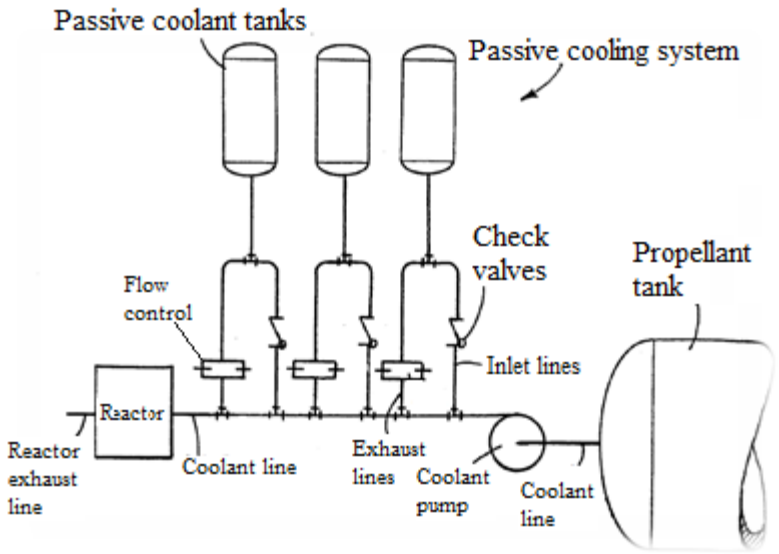

Figure 7.2 Decay heat removal system of open cycle reactor (Malloy, 1994)

The Pellet Bed Reactor (PeBR) is a design that was initiated at the University of New Mexico's Institute for Space Nuclear Power Studies (ISNPS) and is deemed sufficient for both thermal and electric propulsion missions. Concepts of the PeBR build-up on previous designs such as the pebble bed reactor, high temperature gas-cooled reactors for space propulsion, and NERVA reactors. The PeBR is a hydrogen-cooled reactor with an annular core and with (U-Nb)C microspheres with ZrC spherical fuel pellets. Figure 7.3 presents the microsphere design of the spherical fuel pellet. Figure 7.4 presents the cross-sectional view of the fuel pellet design.

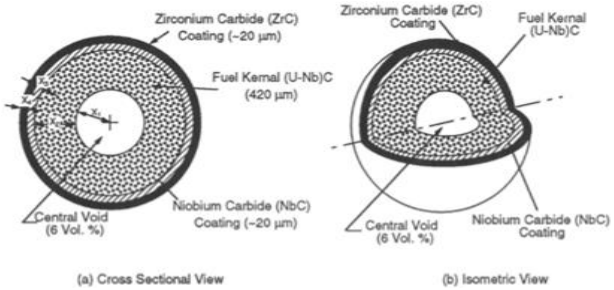

Figure 7.3 PeBR fuel pellet Microsphere design (Morley & El-Genk, 1992)

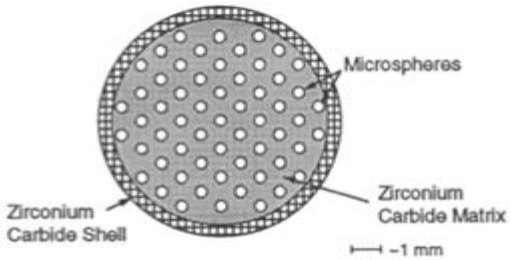

Figure 7.4 Cross-section view of PeBR fuel pellet design (Morley & El-Genk, 1992)

The PeBR fuel pellets are surrounded by inner frits, which are hot; and outer porous frits, which are cold. Normal operation of the PeBR involves the propellant entering the core radially by first entering the outer frit at 120-200 K and then leaving the inner frit at a temperature of almost 3000 K. From the inner frit, the propellant continues to the central channel. The propellant then travels via the rocket expansion nozzle, hence exiting the reactor. There is no need for an internal core structure, support structure, or guide tubes since the fuel pellets are self-supported. Figure 7.5 shows the layout of a PeBR reactor within a nuclear thermal rocket.

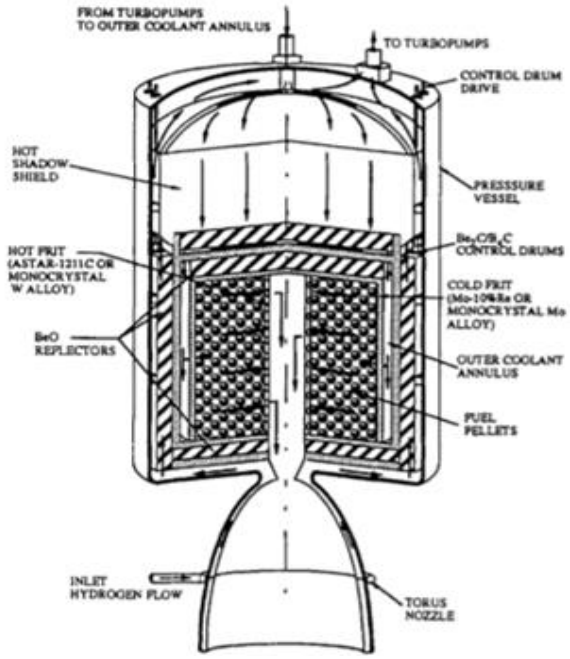

Figure 7.5 Layout of PeBR within nuclear thermal rocket (Morley & El-Genk, 1992)

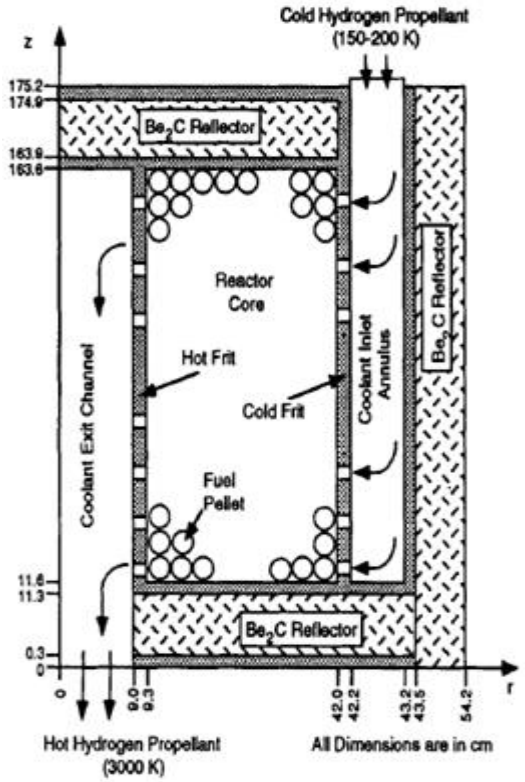

Figure 7.6 Cross-sectional layout of the PeBR with fuel pellets (Morley & El-Genk, 1992)

The PeBR design has both active and passive safety systems that operate after the reactor has been shut down. These safety systems are needed in order to remove the decay heat. Active safety systems involve passing the propellant through the core. However, the drawback here is that additional propellant inventory is needed in order to cool down the reactor post-shutdown. Passive safety system here involves the reactor core cooling down naturally via conduction/radiation, where the decay heat is gradually rejected to the surroundings. Morley and El-Genk (1992) did a multi-dimensional transient heat conduction/radiation model of the PeBR core and surrounding structures. Their analysis shows that total passive cooling of the reactor core isn't possible for decay heat removal. Instead, using active cooling for 600-1000 s from shut down, followed by passive cooling is sufficient to remove the decay heat.

Another design of the PeBR is known as the bimodal PeBR (BM-PeBR). Like the PeBR design, the BM-PeBR uses UC as fuel and hydrogen as propellant. Distinct from the PeBR, this utilizes a helium-xenon (He-Xe) closed Brayton cycle (CBC) engine and has structural materials consisting of super-alloys, and hydrogen Among the objectives of the BM-PeBR are: (i) ability to deliver electric power and thermal propulsion needs, (ii) have an annular reactor core design and several CBC engines as back-up components, (iii) maintain a maximum fuel temperature less than 1600 K

(applicable for power generation and propulsion modes), (iv) have fuel pellets that retain the fission products, (v) have two independent reactor control systems that support each other, (vi) facilitate passive decay heat removal , (vii) have a negative temperature reactivity feedback to assist with stable reactor operation and safety , (viii) have a high specific impulse (650-750 s) and (ix) obtain specific power densities of 11.0 -21.9 We/kg that are feasible at power ranges of 10-40 kWe. The potential uses of the BM-PeBR include powering surveillance satellites for planetary exploration, world-wide air traffic control, and to transport payloads to higher orbits for preservation of launch cost to geosynchronous orbits.

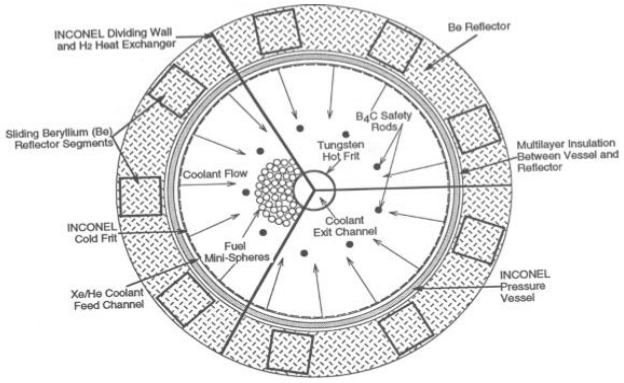

Figure 7.7 Cross-sectional view of the BM-PeBR core (El-Genk, Liscum-Powell, & Pelaccio, 1994)

As for reactor control, the BM-PeBR has two control systems that support each other. The first system involves nine sliding reflector segments that are spaced equally within the Beryllium reflector (see Figure 7.7). When the reactor is undergoing shutdown, the segments are left open. The second system involves nine B4C safety rods, arranged in three groups of three, and are located at a 0.08 radius from the center of the core. Each of these safety rods have a diameter of 35 mm.

The reactor vessel is surrounded by a radial reflector, which is thermally insulated and utilizes multi-foil insulation to avert greater than normal temperatures in the reflector by the hot He-Xe working fluid. There is a sodium heat pipe radiator that is coupled to the reactor vessel via conduction and is suited for passive decay heat removal (see Figure 7.8). Similar to the PeBR, the BM-PeBR has a large height-to-diameter ratio. The radial heat transfer path and large outer surface area of the reactor make passive cooling and decay heat removal possible.

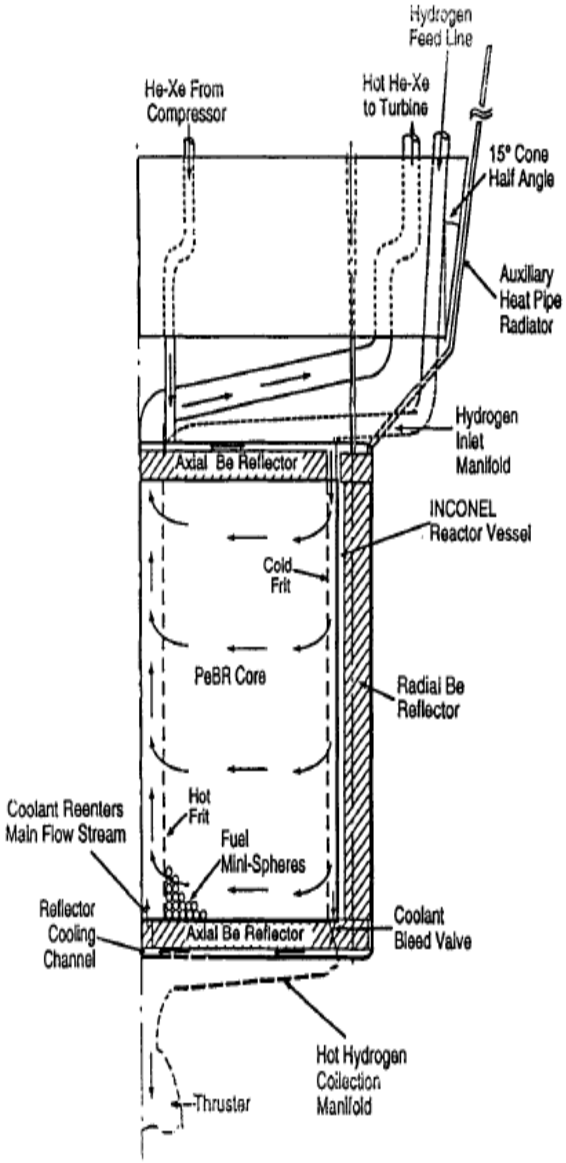

Figure 7.8 Axial cross-sectional view of BM-PeBR with external radiator (El-Genk, Liscum-Powell, & Pelaccio, 1994)

7.3 Literature review of non-forced circulation systems in space

As mentioned in section 7.1, passive safety systems have been devised for terrestrial reactors. Many of these passive safety systems depend on natural circulation. Natural circulation is achieved due to fluid density differences or phase differences in the heat source and heat sink. Among the benefits of natural circulation include simplicity of design, less maintenance needed, no risk of pump/compressor related accidents, and the flow rate increases with power (especially, two-phase flow). One of the drawbacks of natural circulation is the low flow head. Due to the low flow head,

the size of the closed loop must be increased or the flow resistance in the loop must be decreased, in order to maximize the flow rate (IAEA, 2005).

It is generally accepted that natural circulation doesn't work without gravity. However, non-forced circulation systems for use in space have been devised. In particular, heat pipes have been used (see Figure 7.9). A heat pipe has closed ends and allows two-phase flow to transpire between a heat source and a heat sink. The heat source is at one end of the pipe and evaporates the fluid. The vapor flows to the condenser on the opposite end of the pipe. The condensed fluid returns to the evaporator via a wick structure using capillary motion.

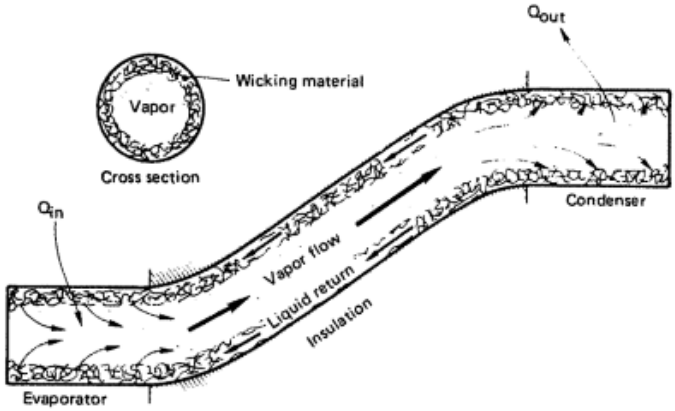

Figure 7.9 Simple diagram of a heat pipe (Lienhard IV & Lienhard V, 2016)

Hall and Doster (1986) report that heat pipes have been used in order to transfer heat in space reactor designs for civilian/military needs. In such heat pipes, lithium is the coolant since it transitions from liquid to vapor at the preferred operating temperature. In addition, heat pipe reactors have been proposed for in-space electrical power production and planetary electrical power (Wright et al (2005); Elliot, Lipinski, & Poston, 2003; Houts et al, 2003; El-Genk & Tournier, 2004)). There are several benefits to utilizing heat pipe reactors: (i) no need for pumps/compressors due to fluid motion driven by vaporization, condensation, and wicking processes; and (ii) heat pipes can deal with the freezing and thawing in the absence of gravity.

Walker, Tarau, and Anderson (2013) have designed and tested high-temperature alkali metal heat pipes for space fission power. In particular, they designed a self-venting arterial heat pipe and a grooved heat pipe. A self-venting arterial pipe contains a screen artery. Inside this screen artery are small venting pores in the evaporator section that permit trapped vapor or non-condensable gas to escape. Grooved heat pipes are designated for spacecraft thermal control since non-condensable gas in grooves can easily escape.

El-Genk and Tournier (2004) came up with a conceptual design of a heat pipe-segmented thermoelectric module converters space reactor power system that can deliver a net power of 110

KWe. This particular reactor has a hexagonal core with 126 heat pipe modules and uses uranium nitride fuel pins with rhenium cladding. This design is part of NASA's goals to develop designs of space reactor power systems (SRPSs) for future missions to planets. Ideally, these SRPSs provide 50 to 300 KWe for the purpose of operating multiple units of electric thrust engines.

According to Shukla (2015), plenty of heat pipes have been designated for space applications. The following are examples of heat pipes: (i) variable conductance heat pipe (VCHP), (ii) cryogenic heat pipe, (iii) vapor chamber heat pipe, and (iv) loop heat pipe. The VCHP is a capillary driven heat pipe that utilizes a non-condensable gas in addition to the default coolant. Communication technology satellites are one area where VCHPs are favored (Mock, Marcus, & Edelman, 1975). Cryogenic heat pipes have been favored for use in thermal control of charge-coupled device (CCD) cameras, which are utilized for the NASA-space interferometry mission (Bugby, Cepeda-Rizo, & Rodriguez, 2011). A vapor chamber heat pipe is a flat-plate heat pipe with a small aspect ratio. Vapor chamber heat pipes are used in flight sensitive applications, for example, avionics packages, computers, and surface mount circuit board cores. Loop heat pipes are currently favored to serve as thermal control devices for high powered telecommunication satellites (Shukla, 2015).

7.4 Design of secondary system loop

In this section, we describe the design of the secondary system loop shown in Figure 7.10. This secondary loop is connected to the tie rods in the core. By default, the inlet of the tie rod tubes is connected to a manifold at the entrance. This manifold receives part of the propellant from the propellant tank (see Figure 2.1). The original system doesn't have manifolds at the exit. In Figure 7.10, we have added manifolds at the exit and this will send the coolant to the radiator. The check valve is located after the tie rod exit manifold and is needed to make sure the secondary system coolant will flow in just one direction. Checks valves depend on flow in order keep them open or closed. The internal disc inside the check valves permits coolant to pass through it in the forward direction, hence opening the valve. The internal disc starts to close as the flow rate declines or the flow moves in the opposite direction (Johnson, 2006). There are various kinds of check valves: (i) ball check valve, (ii) dual plate valve, (iii) in-line check valve, (iv) piston check valve, and (v) swing check valve. Without the check valve, there will be conflicting flow. Check valves are available in the market for aerospace applications. For example, Valcor Engineering Corporation manufactures check valves that can be used in the spacecraft's reaction control systems or altitude control systems (Valcor Engineering Corporation, 2017). CIRCOR Aerospace also manufactures check valves for space applications (CIRCOR Aerospace, 2017). The hydrogen from the propellant tank will no longer flow through the tie tubes. Instead, the hydrogen will all be sent through the main propellant

line in Figure 7.10. However, the total flow of 18.59 kg/s going through the rocket is still the same as before.

This secondary circuit needs to be operated such that the melting points of the tie rod tube materials aren't exceeded. In particular, the melting points are presented in Table 7.1. We don't have the melting point of ZrH, but the melting point of zirconium(II) hydride (ZrH_2) is available. Hence, we are assuming the melting point of ZrH is comparable to ZrH_2.

Table 7.1Tie rod tube materials melting points

Material	Melting point (K)	Reference
ZrC	3795.15	AZO Materials, 2016
Graphite	3773.15	Entegris, 2013
Zirconium(II) hydride (ZrH_2)	1073.15	US Nano, ND

Table 7.1 shows that 1073.15 K is the maximum temperature constraint of the secondary system loop. The other temperature constraint is the freezing point of hydrogen, which is 14.01 K. Given that the tie rods are scattered around the core, it is important to pass coolant through them during normal operation. Hence, this secondary system should cool the ZrH moderator in normal steady-state operation and remove decay heat in a post-LOFA accident.

In designing the secondary loop, the dimensions of the tie rod tubes and the tie rod manifolds will be kept the same as the default design. We are left to determine the dimensions of the radiator and the outside pipes. Such will be discussed in the proceeding section. The radiator will be assumed to be a collection of tubes rather than just a single tank. In this way, the radiator will have better heat transfer with the surroundings due to its high HTSA.

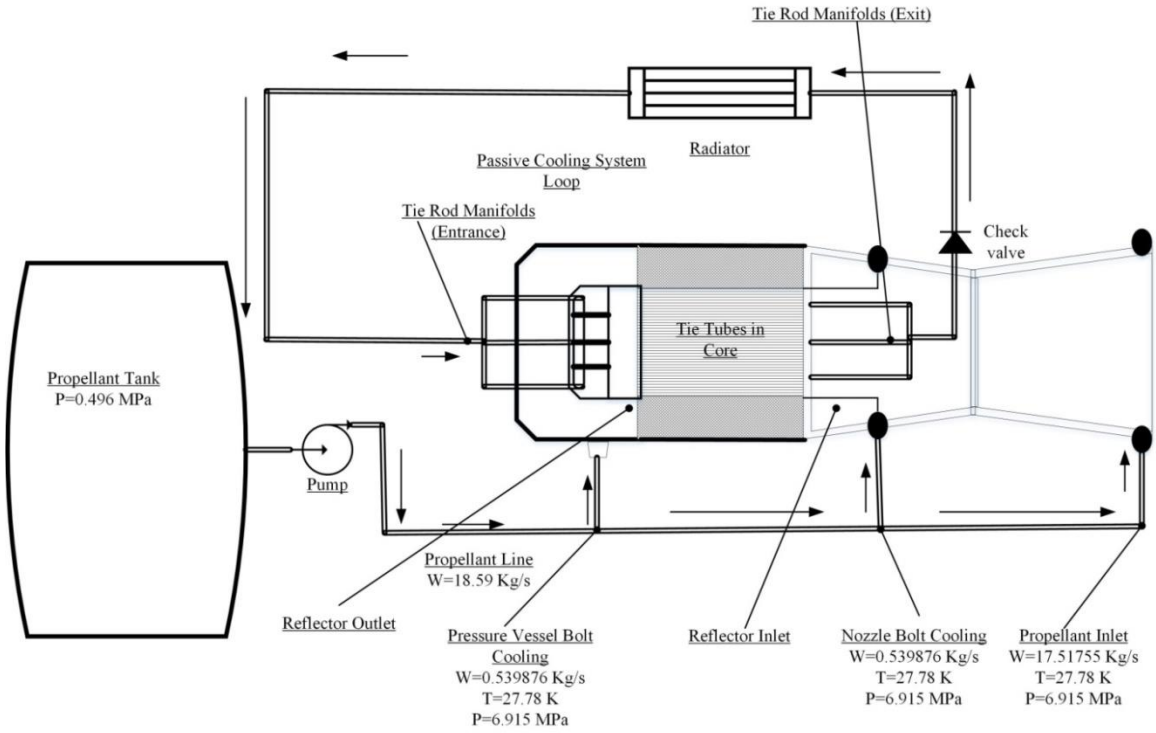

Figure 7.10 Diagram of proposed safety system

7.5 System modeling of Pewee I with secondary system

Here, the Pewee RELAP5 model presented in Figures 4.1-4.3 has been modified. With modeling the secondary system in Figure 7.11, the HV 520 and HV 530 are retained from the original RELAP model (Figure 4.1). We have added HV 540 (tie rod manifold exit), the check valve, HV 550 (pipe between tie rod manifold exit and radiator inlet tubes), HV 560 (radiator inlet tubes), HV 570 (radiator tubes), HV 580 (radiator exit tubes) and HV 590 (pipe between radiator exit tubes and tie rod manifold entrance). In this secondary loop design, HV 530 is the main heat source and HV 570 is the main heat sink. Aside from these, there are other structures that handle heat transfer: (i) HV 520 and HV 540 as minor heat sources, and (ii) HV 560 and HV 580 as minor heat sinks. In reality, the minor heat source HV 520 will absorb some heat via convection with the main propellant. In the same manner, the minor heat source HV 580 will absorb some heat via convection with the propellant entering the nozzle inlet. The following heat sinks have a temperature boundary condition, where the outside is held at a constant temperature: HV 560, HV 570, and HV 580.

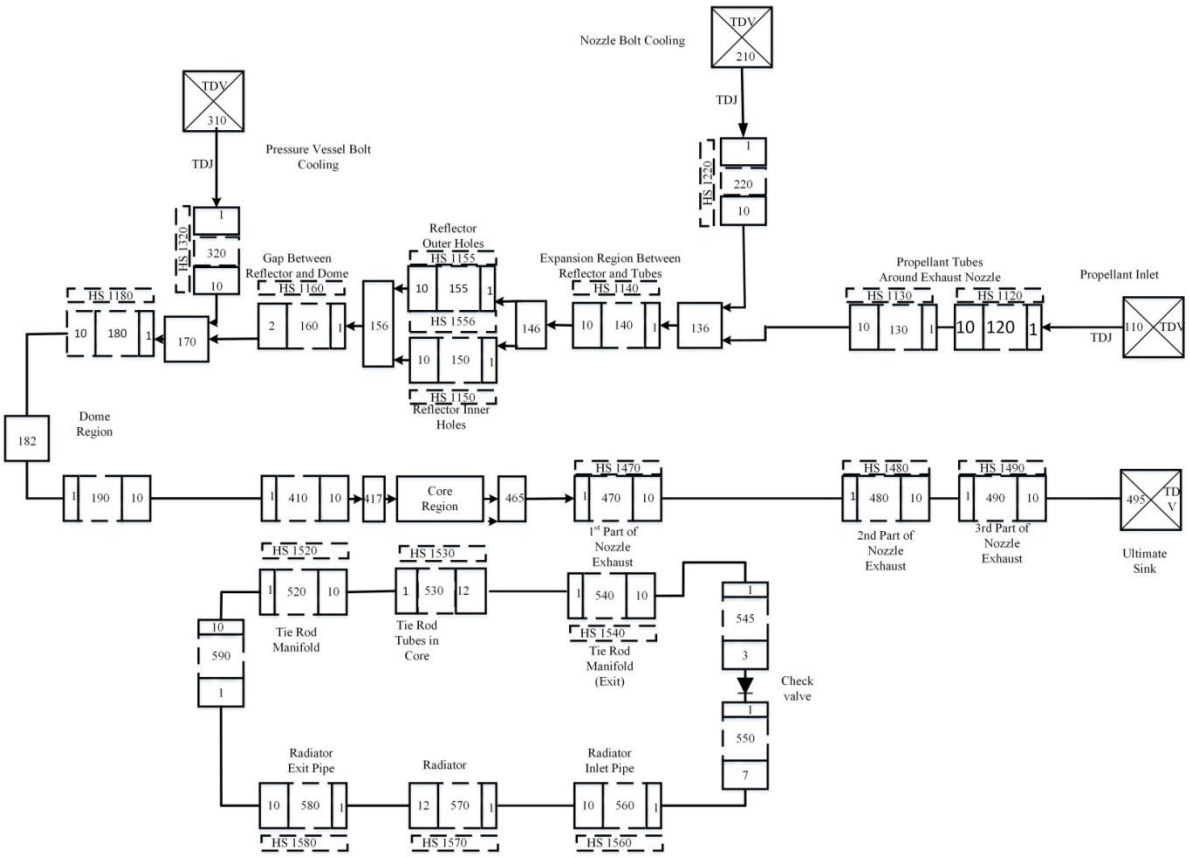

Figure 7.11 Overall RELAP5 nodalization diagram of the Pewee I with secondary system

7.6 Testing of secondary system during steady-state operation

As mentioned earlier, the secondary system has to be operated during steady-state operation in order to keep the tie rods cooled. The dimensions of HV 570 (radiator), HV 560 (radiator inlet), and HV 580 (radiator outlet), were adjusted to keep the tie rod temperatures from melting and achieve natural circulation. We can't adjust the dimensions of the tie rod tubes (HV 530) and the tie rod manifolds (HV 520 and HV 540) as these are fixed. The main quantity that will be adjusted is the HTSA of HV 560, HV 570, and HV 580. In RELAP5, this is easily done by increasing the total heat transfer length of that particular hydrodynamic volume in the corresponding heat structure.

Table 7.2 presents a summary of cases that were considered. Table 7.3 presents sample dimensions and materials used in the RELAP model. As with the total flow areas of the tie rod tubes (HV 530) and tie rod manifolds (HV 520 and HV 540), the default values were retained. The materials and dimensions of HV 545, HV 550, HV 560, HV 570, HV 580, and HV 590 were freely decided. For the following hydrodynamic volumes, graphite was selected as the material: HV 545, HV 550, HV 560, HV 570, HV 580, and HV 590. Graphite has a very low service temperature of 0 K and a high melting point of 3773.15 K. This temperature range makes it suitable for operation in

space, where temperatures are as low as 3 K. In addition, the M1 elements and the slat tubes were manufactured from graphite in the original Pewee design.

Table 7.2 Sample cases to run

Case ID	Heat transfer surface area of heat sinks
1	2*(HTSA of secondary loop heat sources)
2	4*(HTSA of secondary loop heat sources)
3	6*(HTSA of secondary loop heat sources)
4	8*(HTSA of secondary loop heat sources)
5	10*(HTSA of secondary loop heat sources)

Table 7.3 Sample dimensions used in RELAP model for Case 1

HV #	Flow area (m^2)	Length (m)	Materials
520	7.09e-3	1.34	Graphite
530	8.44e-3	1.32	Default as shown in Figure 2.5
540	7.09e-3	1.34	Graphite
545	7.09e-3	4.02e-1	Graphite
550	7.09e-3	9.38e-1	Graphite
560	7.09e-3	1.34	Graphite
570	8.44e-3	1.32	Graphite
580	7.09e-3	1.34	Graphite
590	7.09e-3	1.34	Graphite

Figure 7.12 presents the temperatures from Case 1. Here, the coolant exiting the tie rods is at a temperature of 247.95 K. Note that this temperature is below the original temperature of 260 K shown in Figure 2.1. The temperature leaving the radiator is at 15.67 K. The temperature leaving the fuel elements is at 2026.44 K. Note that this temperature is less than the fuel element temperature shown in Figure 2.1. This is because more coolant is being sent through the fuel elements. The overall temperature of the hydrogen coolant entering the nozzle is 1739.87 K. This temperature is almost 15 K less than the temperature of 1755.23 K shown in Figure 2.1.

Figure 7.13 presents the mass flow rates from Case 1. As expected, the mass flow rates through the fuel elements, M1 elements, slat, and annulus are greater than normal. This time, the mass flow rate through the tie rod tubes is 4.67 kg/s. This flow rate is almost close to the original flow rate of 4.54 kg/s as shown in Figure 2.1.

Figure 7.14 shows that the heat sinks are able to remove the heat generated by the heat sources in the secondary system. Figure 7.15 presents the temperatures from Case 2. There is a major difference in the tie rod tube exit temperatures as compared to Case 1. Here, the coolant exiting the tie rod tubes is at a reduced temperature of 87.92 K. The coolant exiting the radiator is at a temperature of 16.62 K. Figure 7.16 presents the mass flow rates from Case 2. As expected, there is minimal difference in the mass flow rates in the fuel elements, M1, slat, and annulus as compared to Case 1. However, the mass flow rate through the tie rod tubes is now 32.56 kg/s as opposed to 4.67 kg/s. Figure 7.17 also shows a 1-to-1 correlation between heat generated and heat removed.

Figure 7.18 presents the temperatures from Case 3. Here, the coolant exiting the tie rod is at a temperature of 85.84 K. The coolant exiting the radiator is at a temperature of 16.16 K. There is not a major change in the temperature profile of the tie rod, despite having increased the HTSA. The tie rod tube mass flow rate in Figure 29 is at 31.34 kg/s. This also is not a major change from Case 2.

In Table 7.4, we summarize the temperatures obtained from these steady-state cases. In Table 7.5, we summarize the mass flow rates from these steady-state cases.

Table 7.4 Temperature results from steady-state cases

Case ID	Temperature (K)			
	Fuel elements exit	Nozzle inlet **(value from original design)**	Tie rod tubes exit **(value from original design)**	Radiator exit
1	2026.44	1739.87 **(1755.28)**	247.95 **(260.56)**	15.67
2	2018.46	1738.20 **(1755.28)**	87.92 **(260.56)**	16.61
3	2015.08	1739.39 **(1755.28)**	85.83 **(260.56)**	16.16
4	2018.44	1738.21 **(1755.28)**	86.71 **(260.56)**	15.96
5	2015.21	1739.71 **(1755.28)**	86.75 **(260.56)**	15.69

Table 7.5 Mass flow rates from steady-state cases

Case ID	Mass flow (kg/s)				
	Mass Fuel elements	Mass M1 elements	Mass Slats	Mass Annulus	Mass Tie rod tubes **(value from original design)**
1	15.73	0.20	1.99	0.67	4.67 **(4.54)**
2	15.77	0.20	1.98	0.65	32.56 **(4.54)**
3	15.80	0.20	1.97	0.63	31.34 **(4.54)**
4	15.77	0.20	1.98	0.65	34.68 **(4.54)**
5	15.80	0.20	1.96	0.63	34.18 **(4.54)**

From Tables 7.4 and 7.5, we can see that the performance of the secondary system doesn't improve drastically from Case 2 and beyond, as the temperatures and mass flow rates have minor differences.

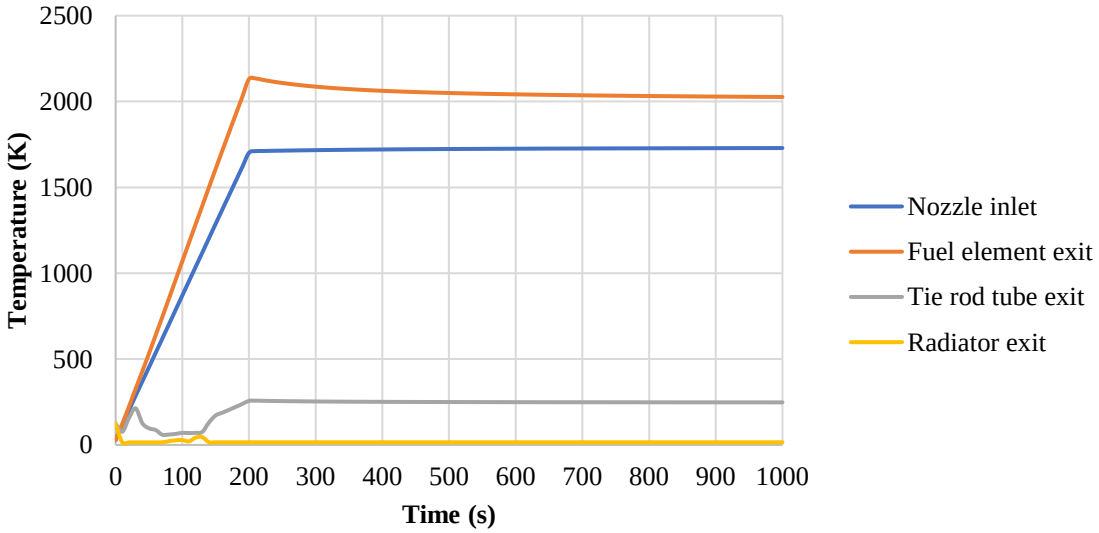

Figure 7.12 Steady-state temperatures for Case 1

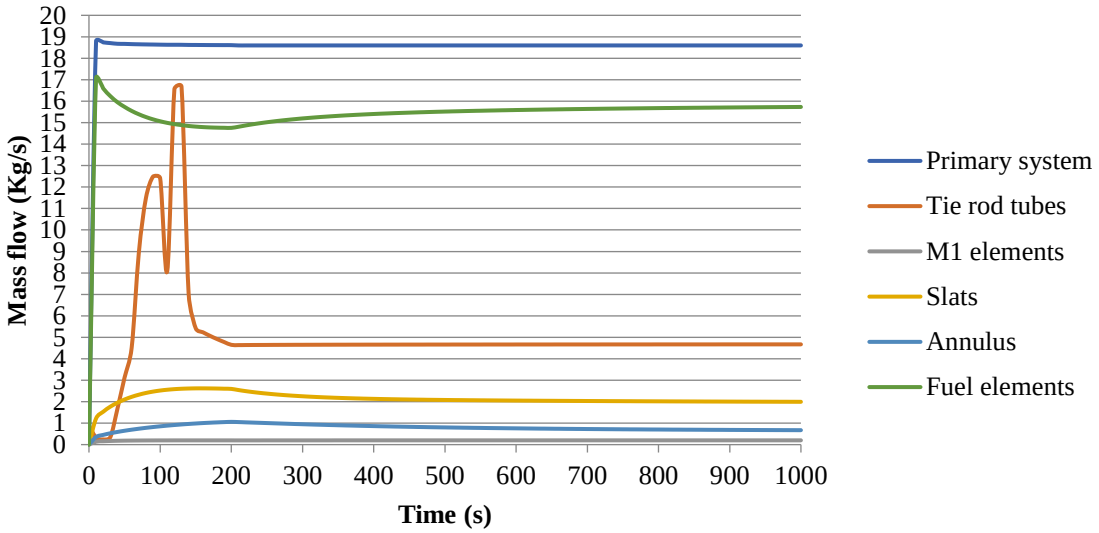

Figure 7.13 Steady-state mass flow rates for Case 1

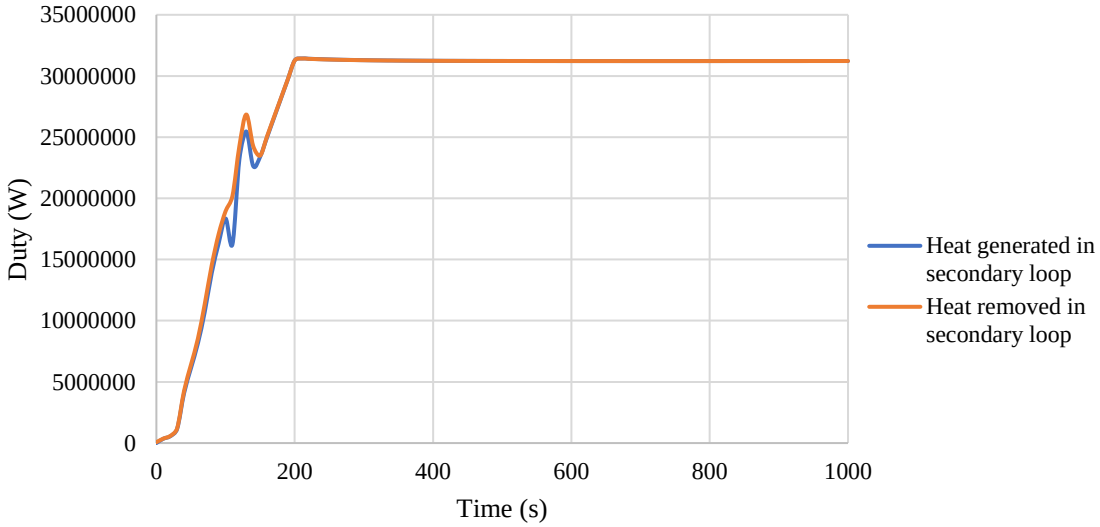

Figure 7.14 Comparison of heat source and heat sink duty for Case 1

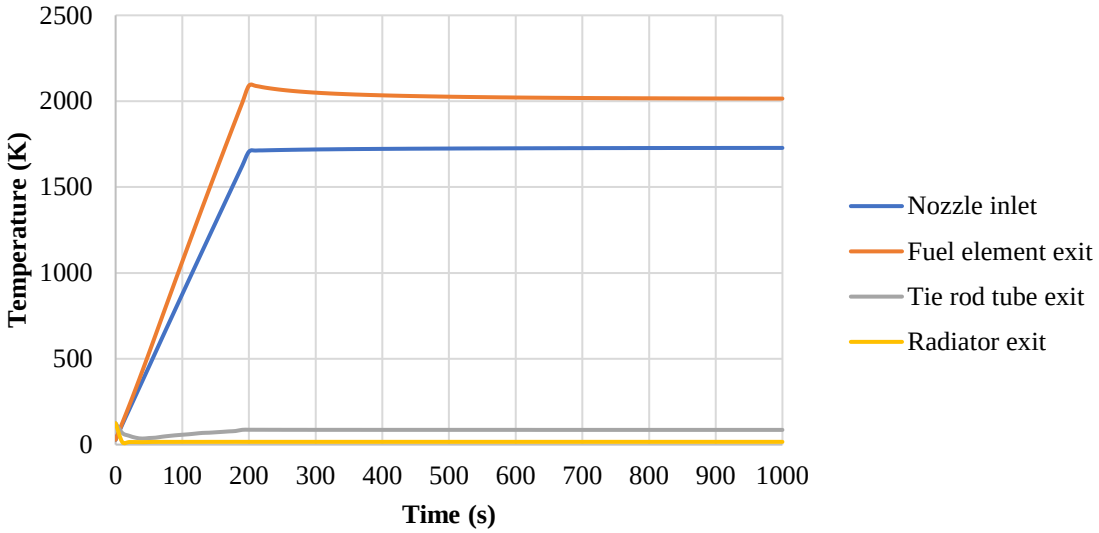

Figure 7.15 Steady-state temperatures for Case 2

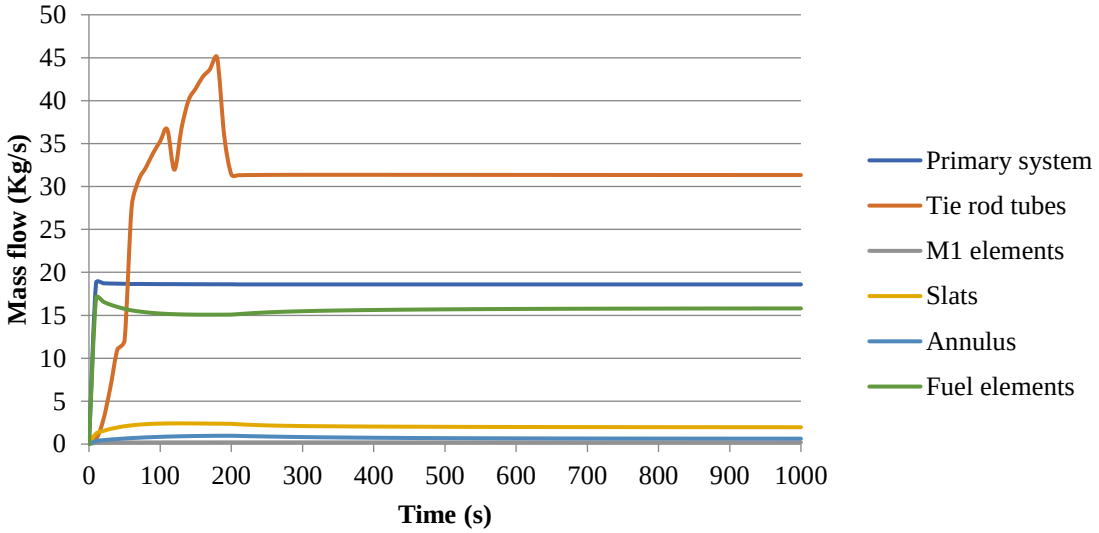

Figure 7.16 Steady-state mass flow rates for Case 2

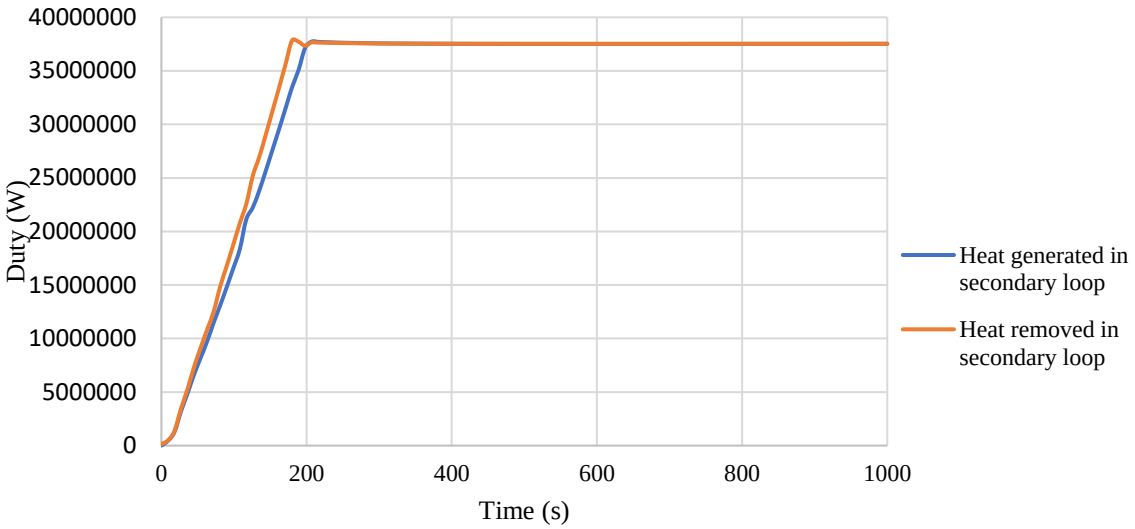

Figure 7.17 Comparison of heat source and heat sink duty for Case 2

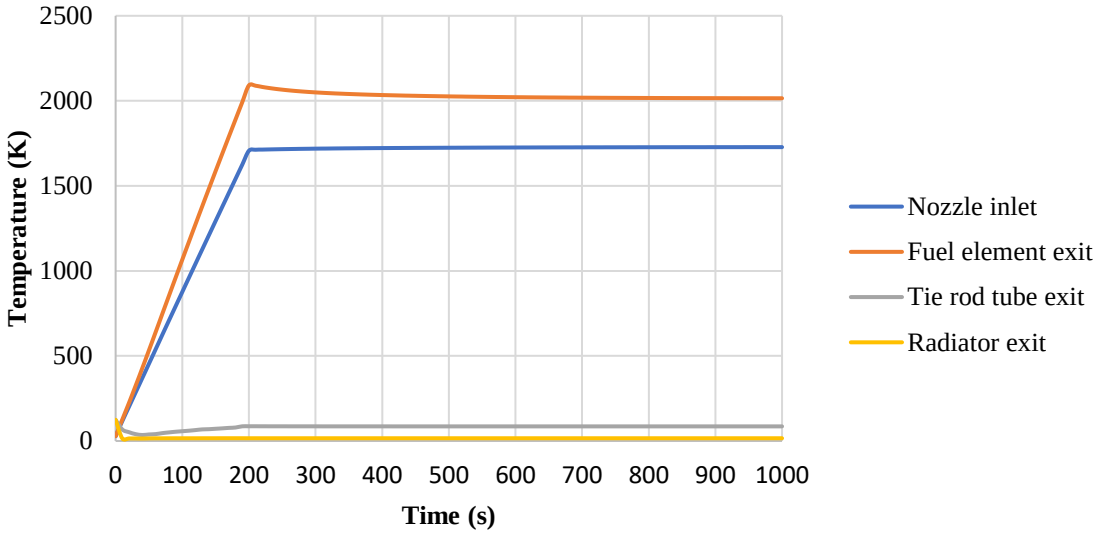

Figure 7.18 Steady-state temperatures for Case 3

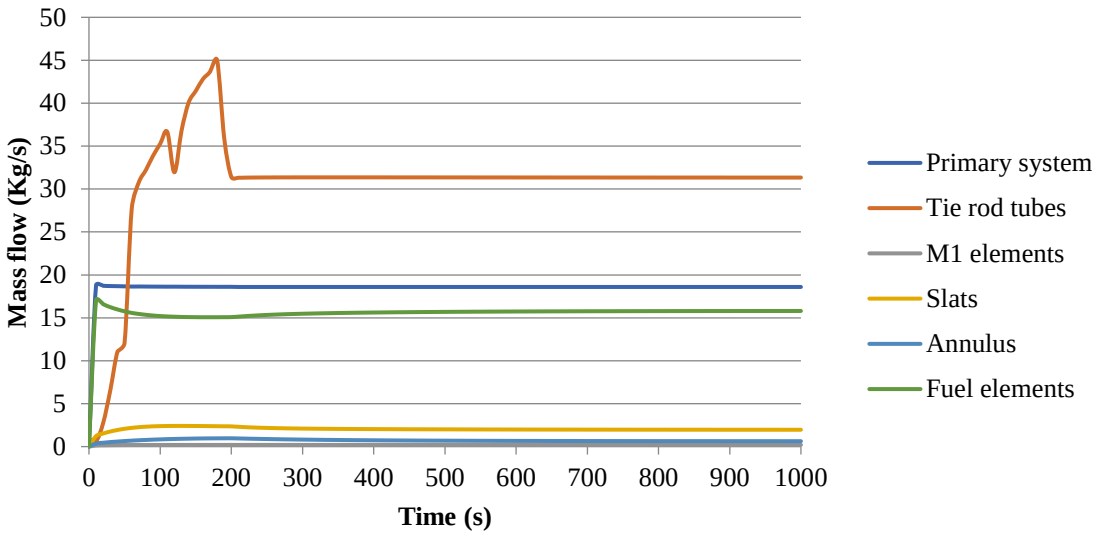

Figure 7.19 Steady-state mass flow rates for Case 3

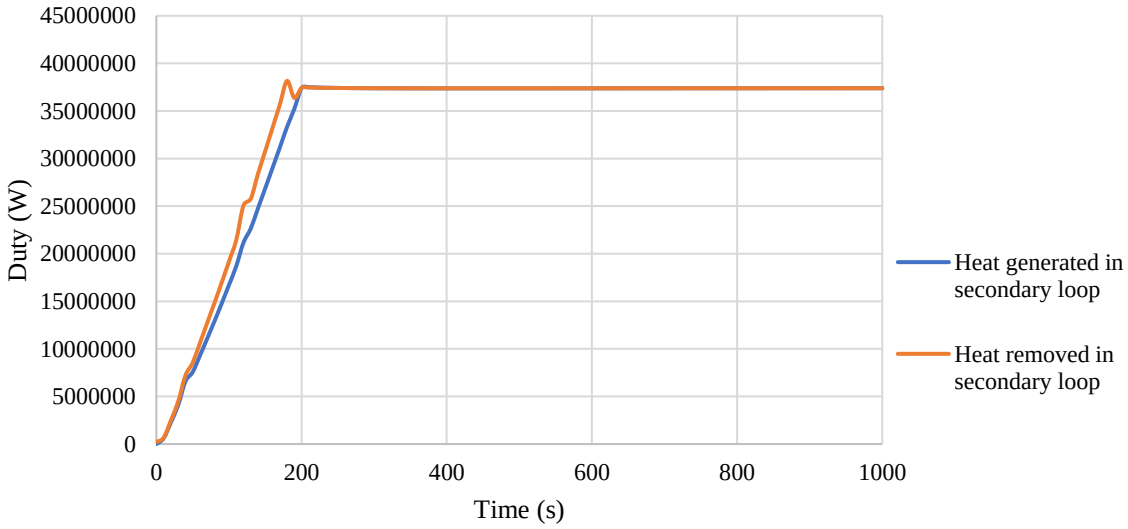

Figure 7.20 Comparison of heat source and heat sink duty for Case 3

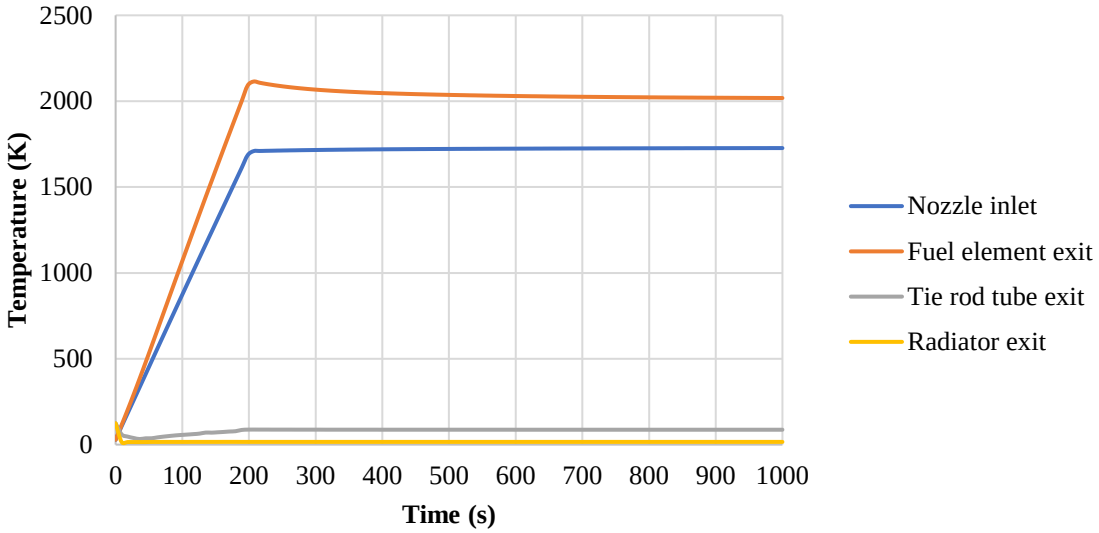

Figure 7.21 Steady-state temperatures for Case 4

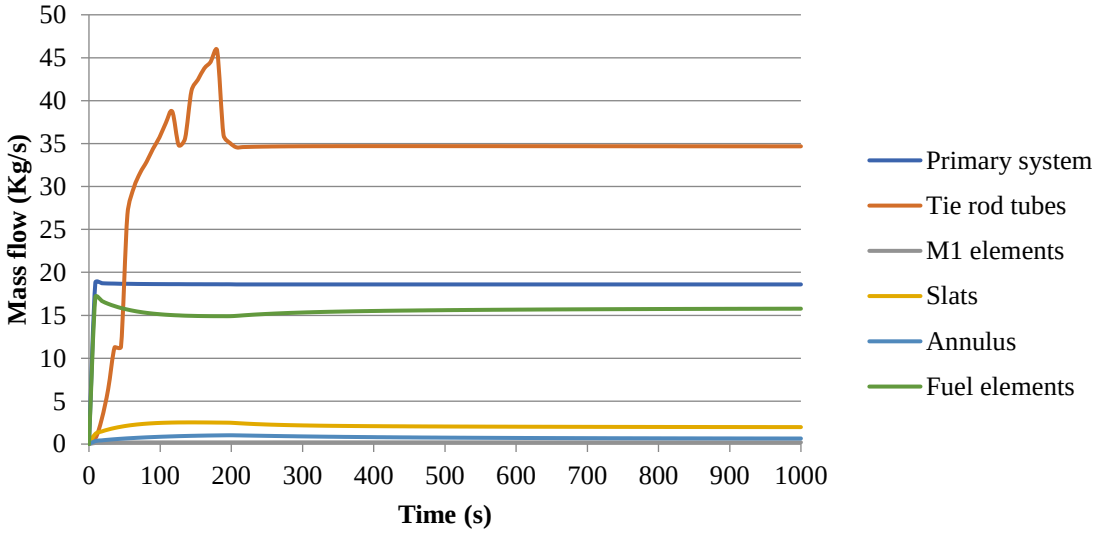

Figure 7.22 Steady-state mass flow rates for Case 4

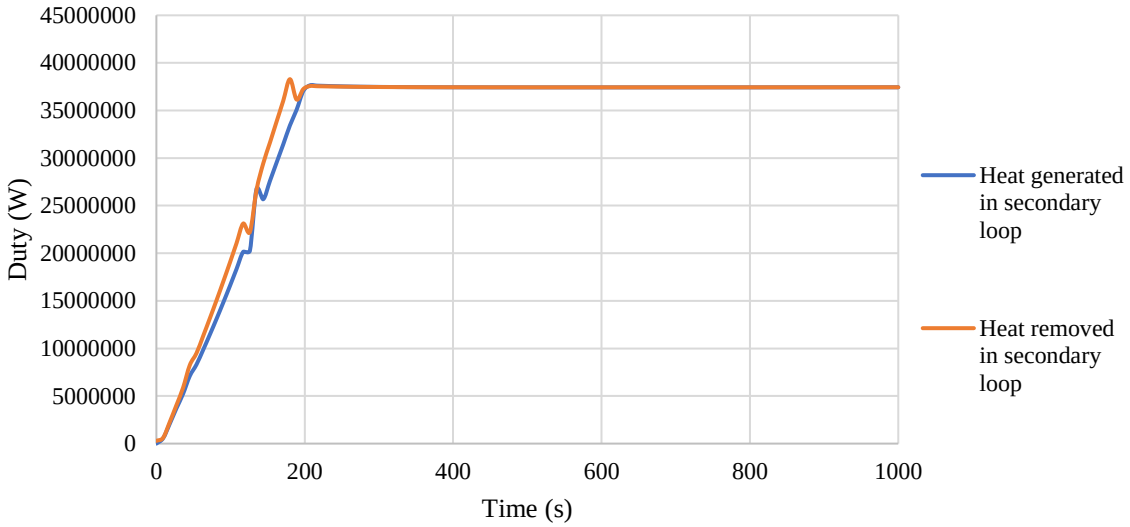

Figure 7.23 Comparison of heat source and heat sink duty for Case 4

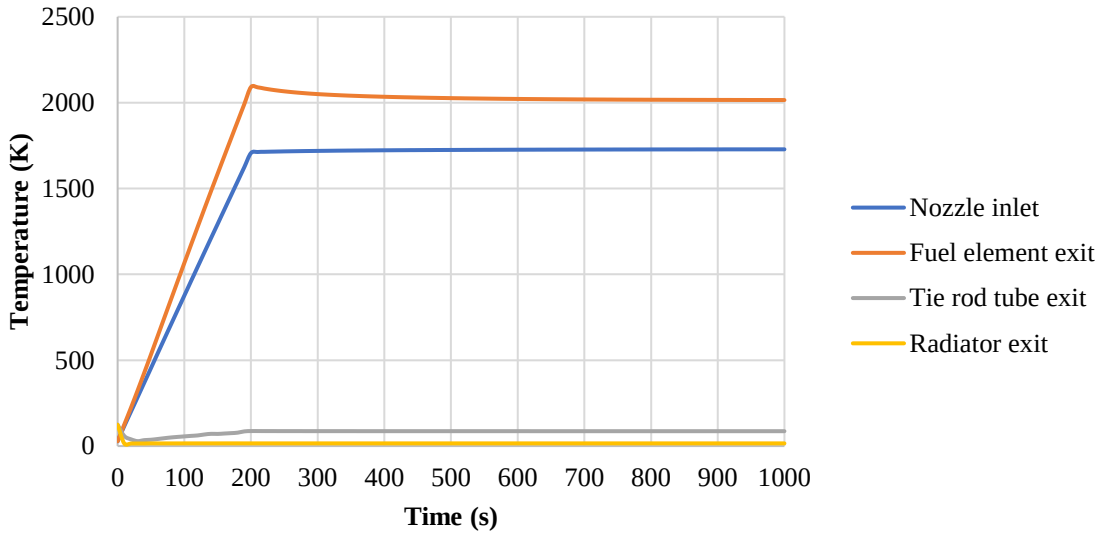

Figure 7.24 Steady-state temperatures for Case 5

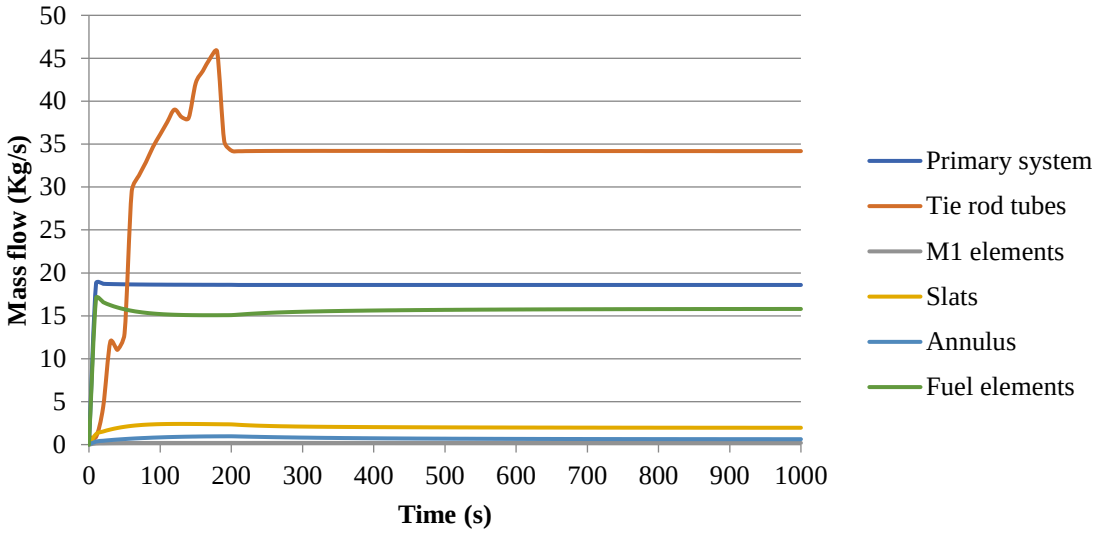

Figure 7.25 Steady-state mass flow rates for Case 5

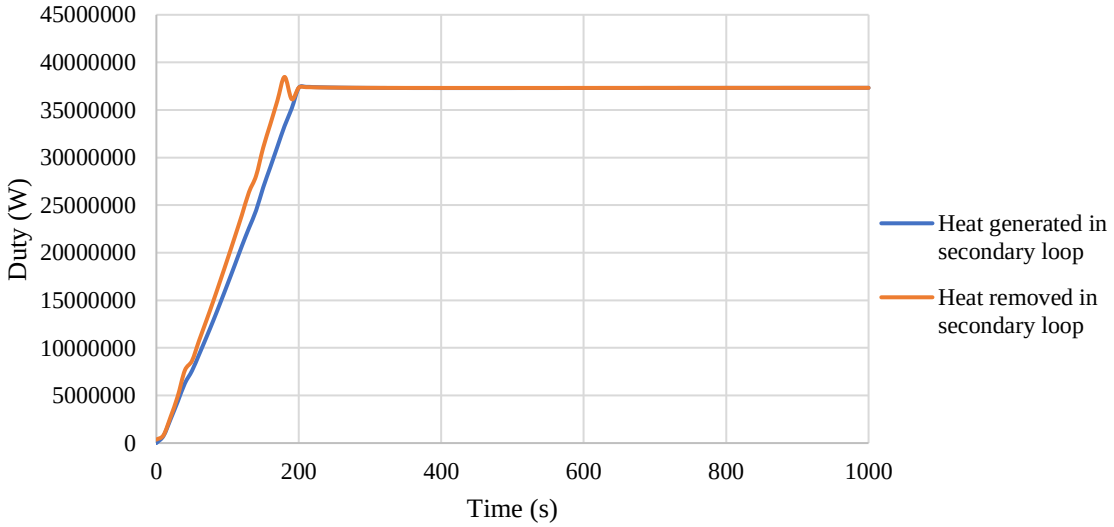

Figure 7.26 Comparison of heat source and heat sink duty for Case 5

7.7 Testing of LOFA and SCRAM on secondary system

The transient runs were initiated on the completed steady-state runs. Transient runs in RELAP5 require a RESTART problem to be resumed from the end-time of the steady-state run. Figures 7.27-7.42 present the graphs resulting from these runs. These figures are a continuation of the steady-state cases presented in Figures 7.12-7.26. In these Figures, the LOFA occurs at a time of 500 seconds. At a time of 560 seconds, the scram is initiated. Part of the steady-state data is presented in these

transient runs to show the change from steady-state to transient. Table 7.6 shows a summary of the events relevant to Figures 7.27-7.42.

Table 7.6 Events scheduled for the RESTART problem

Time (s)	Event
0	Steady-state operation
500	Flow rate throughout system is cut off
560	Scram is initiated
1600	Transient run ends

The decay heat profile used for these transients was calculated using the following relation provided by Glasstone and Sesonske (2010). The decay heat is given by the relation

$$\frac{P}{P_0} \approx 5\times10^{-3} a\left[t_s^{-b} - \left(t_0 + t_s\right)^{-b}\right] \tag{7.1}$$

with the time-dependent values of a and b presented in Table 7.7.

Please note that P_0 is the power prior to shutdown, P is the time-dependent power, t_s is the time since shutdown, and t_0 is the time prior to shutdown.

Table 7.7 Decay heat equation constants

Time after shutdown (s)	a	b
0.1 to 10	12.05	6.39e-2
10 to 150	15.31	18.07e-2
150 to 8×10^8	27.43	29.62e-2

Figure 7.27 shows a graph of the calculated decay heat with the RELAP decay heat. In this work, it was assumed the reactor was in operation for 50 minutes.

We start by looking at the Case 1 results. Looking at Figure 7.28, the temperature of the coolant exiting the tie rod tubes decreases when the LOFA occurs. Referring to Figure 7.29, the mass flow rate in the secondary system has increased while the mass flow rate in the primary system has decreased. The maximum flow rate in the secondary system has reached 40.52 kg/s. From Figure 7.30, the heat sink is removing all of the heat in the heat source in response to the LOFA.

The trends noted in Figures 7.28-7.30 are seen in Figures 7.31-7.42. However, the temperature drop in the tie rods is not as significant as compared to Case 1. Based on observations from both the steady-state and transient runs, Case 1 has the minimum radiator HTSA area needed in order to

prevent the tie rod tubes from melting and to insure a suitable natural circulation.

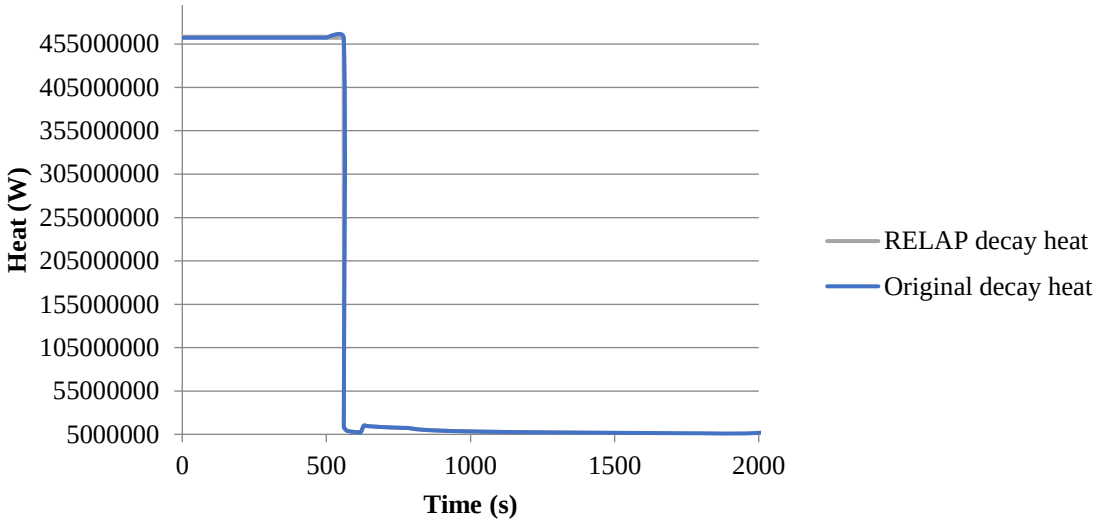

Figure 7.27 Decay heat curve

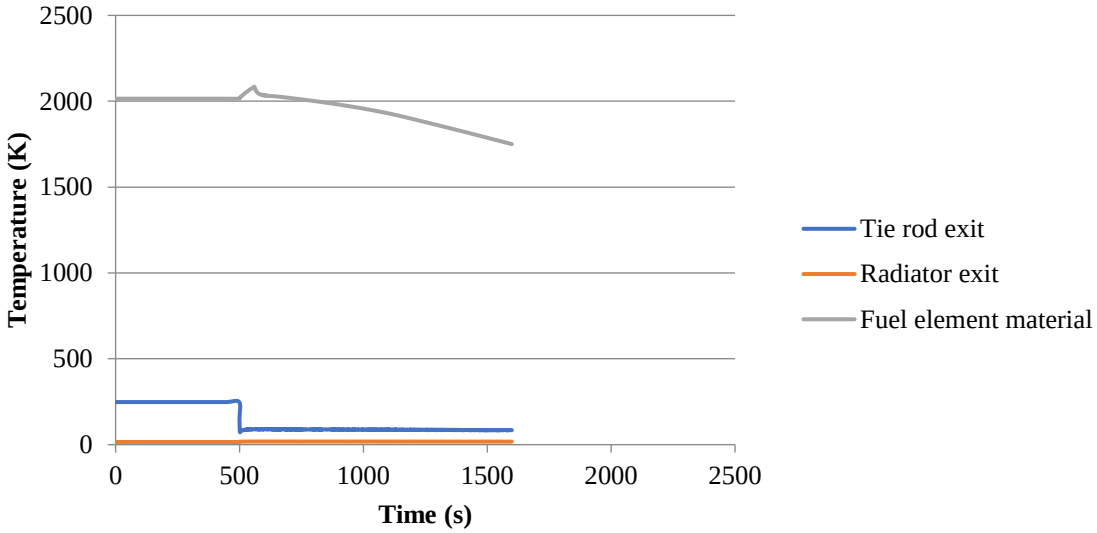

Figure 7.28 Transient temperatures for Case 1

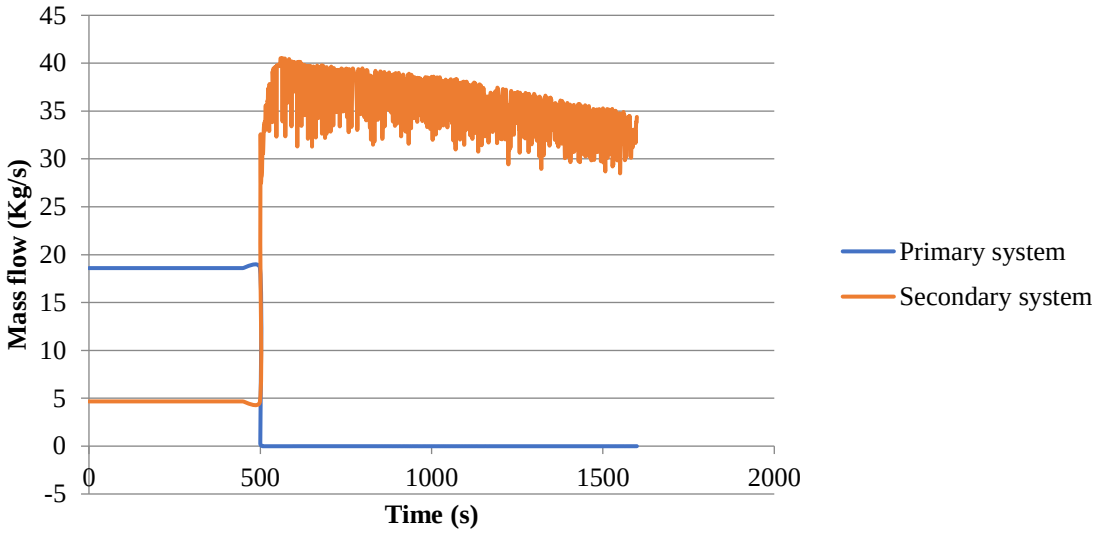

Figure 7.29 Transient mass flow rates for Case 1

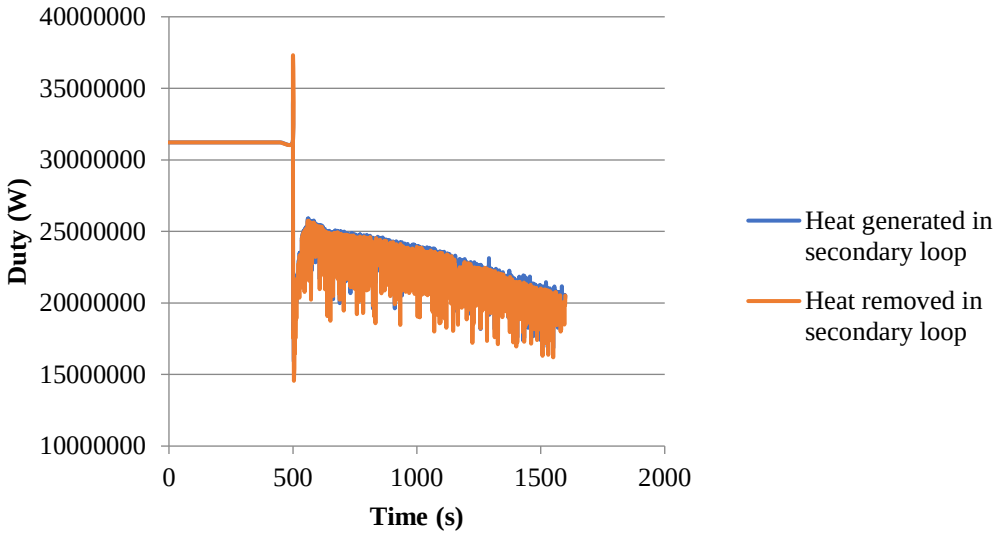

Figure 7.30 Comparison of heat source and heat sink for Case 1

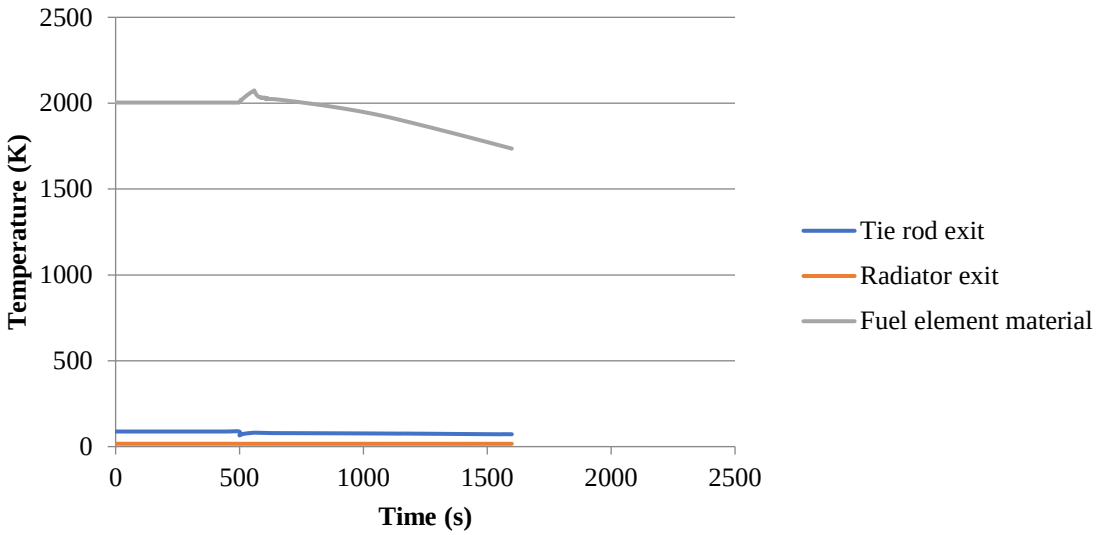

Figure 7.31 Transient temperatures for Case 2

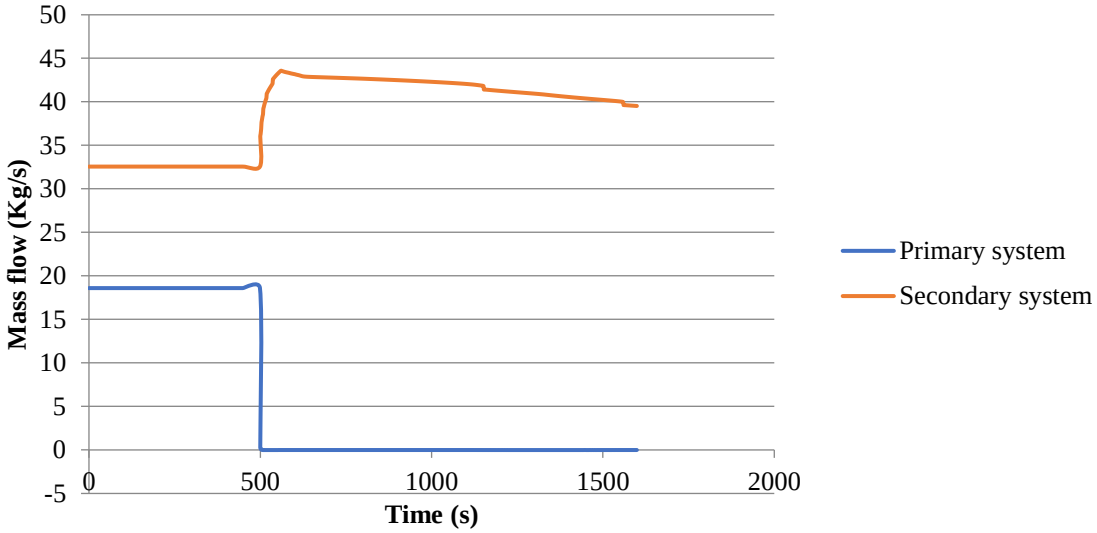

Figure 7.32 Transient mass flow rates for Case 2

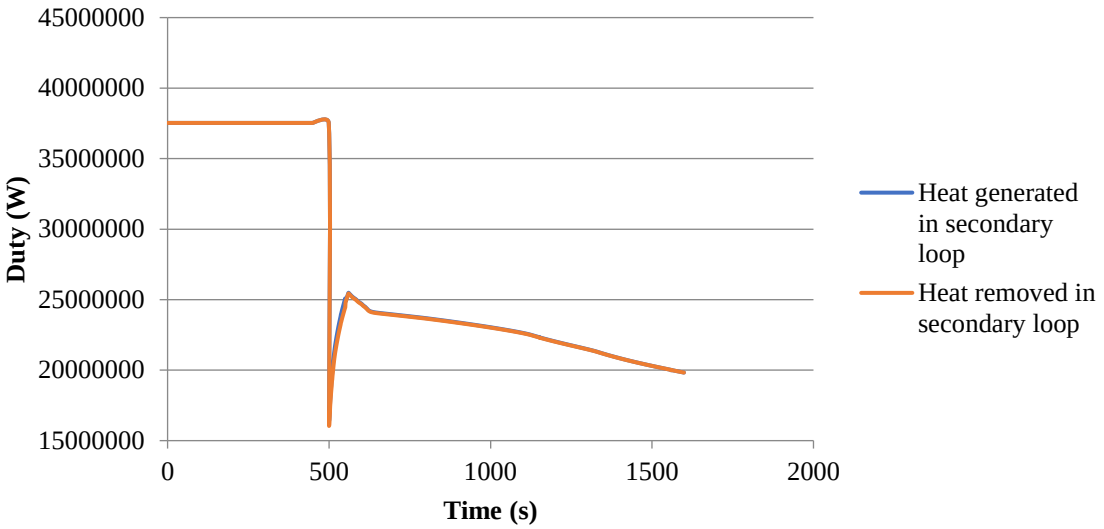

Figure 7.33 Comparison of heat source and heat sink for Case 2

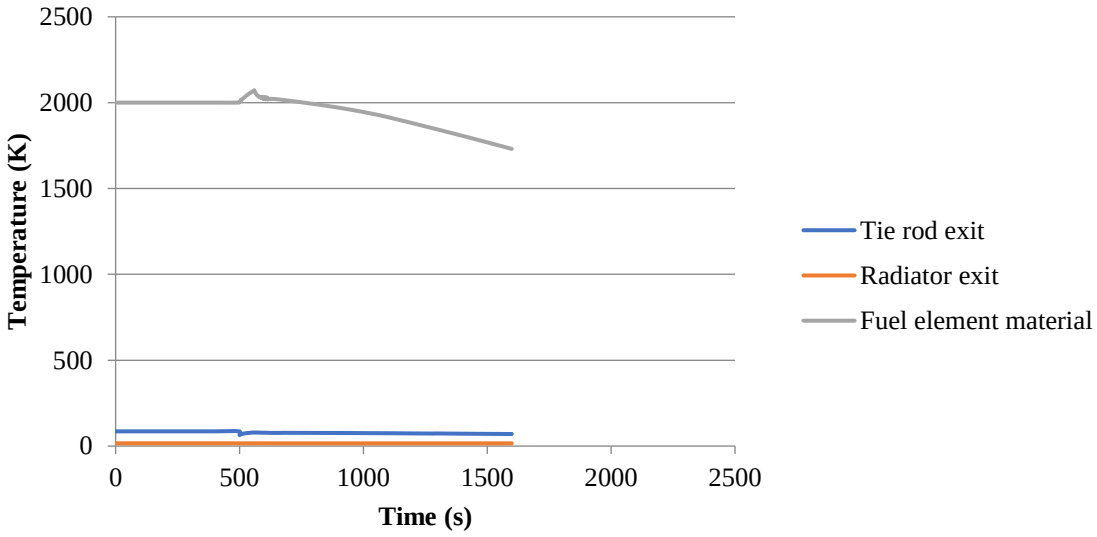

Figure 7.34 Transient temperatures for Case 3

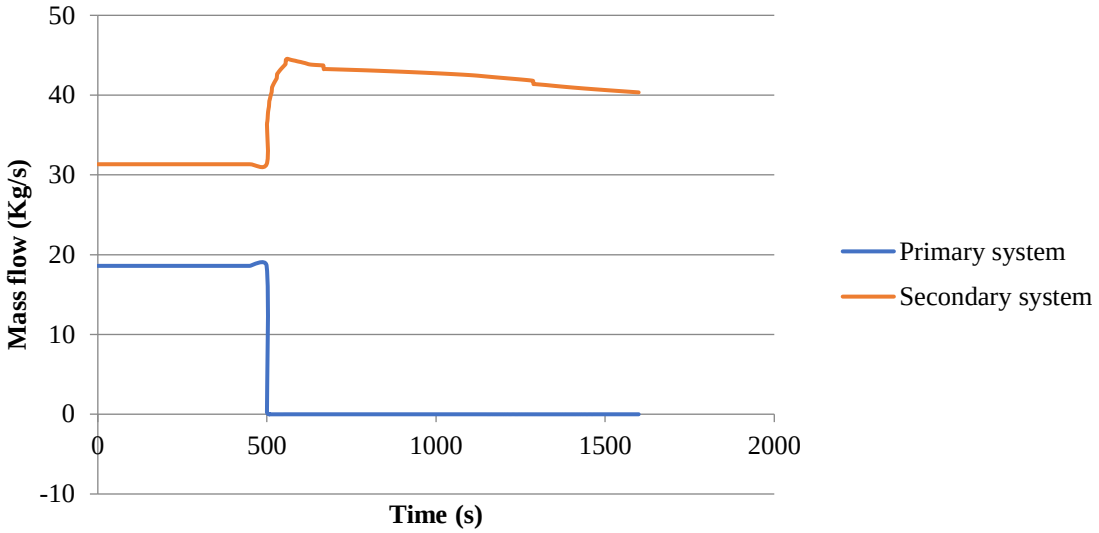

Figure 7.35 Transient mass flow rates for Case 3

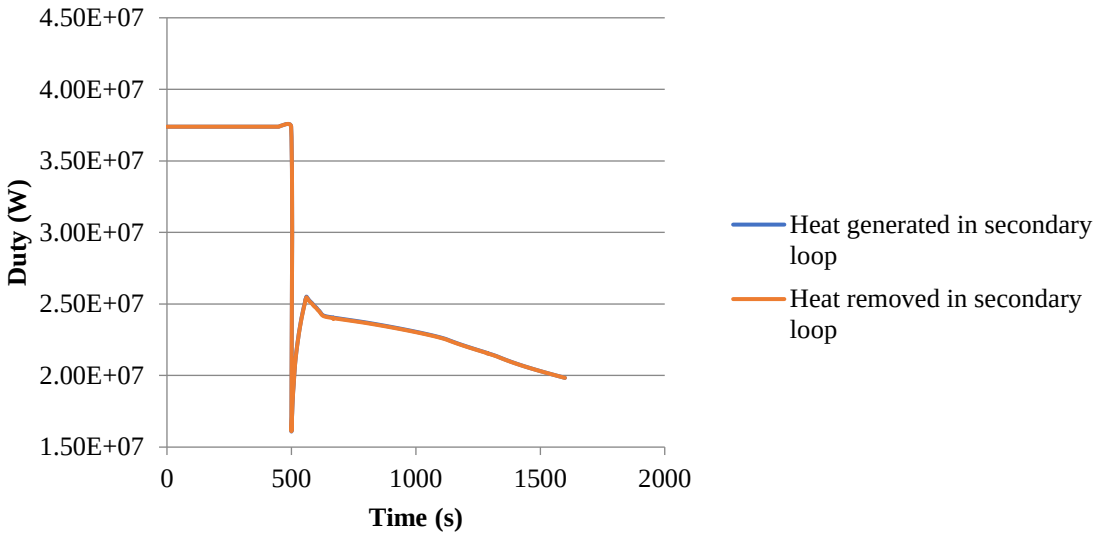

Figure 7.36 Comparison of heat source and heat sink for Case 3

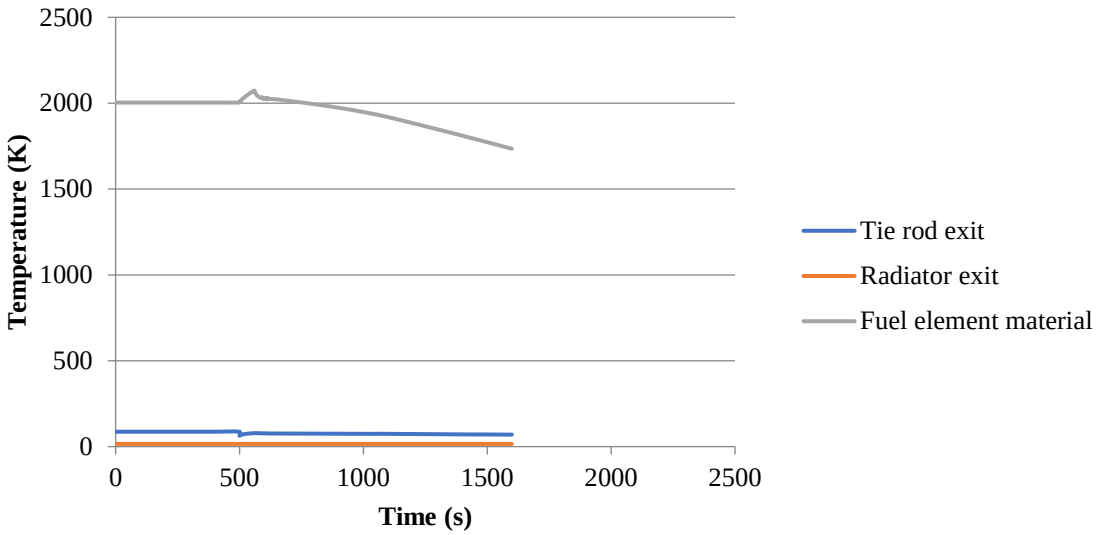

Figure 7.37 Transient temperatures for Case 4

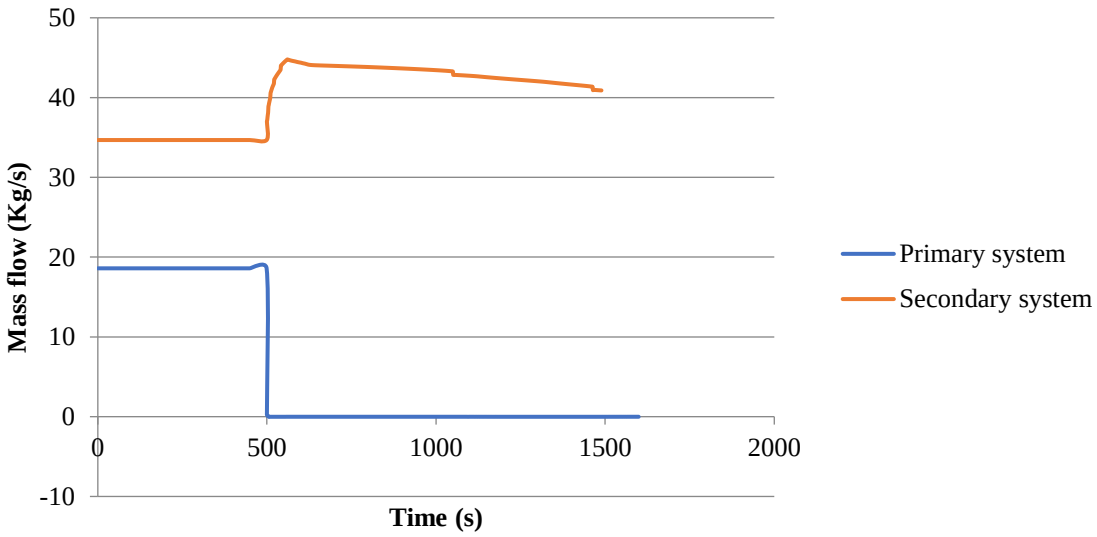

Figure 7.38 Transient mass flow rates for Case 4

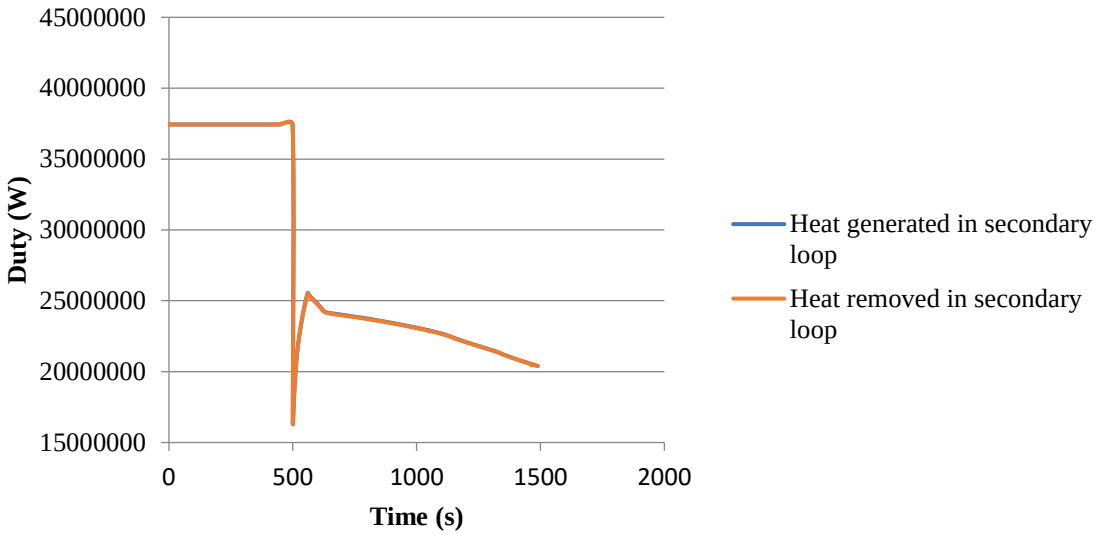

Figure 7.39 Comparison of heat source and heat sink for Case 4

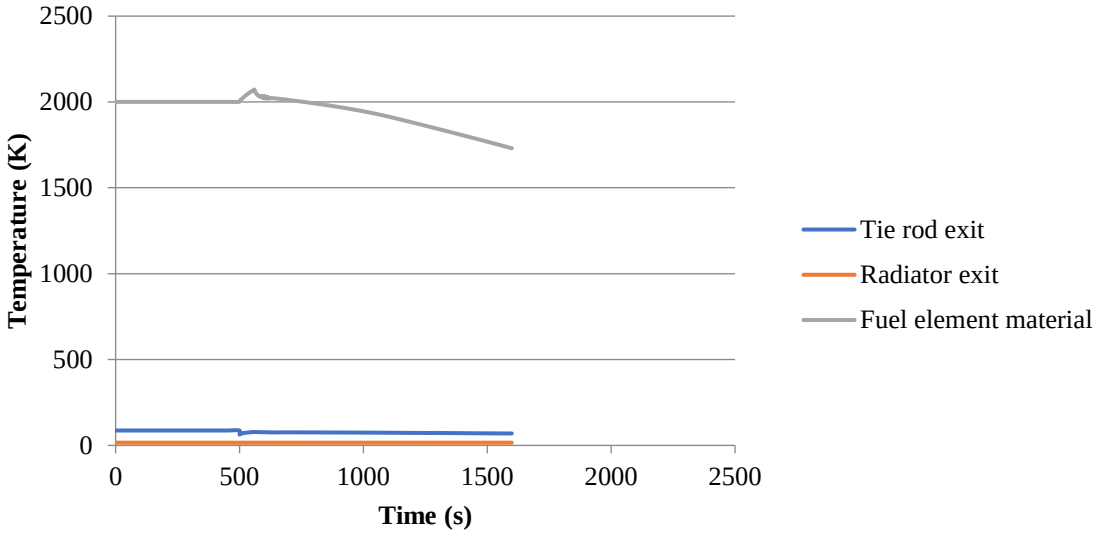

Figure 7.40 Transient temperatures for Case 5

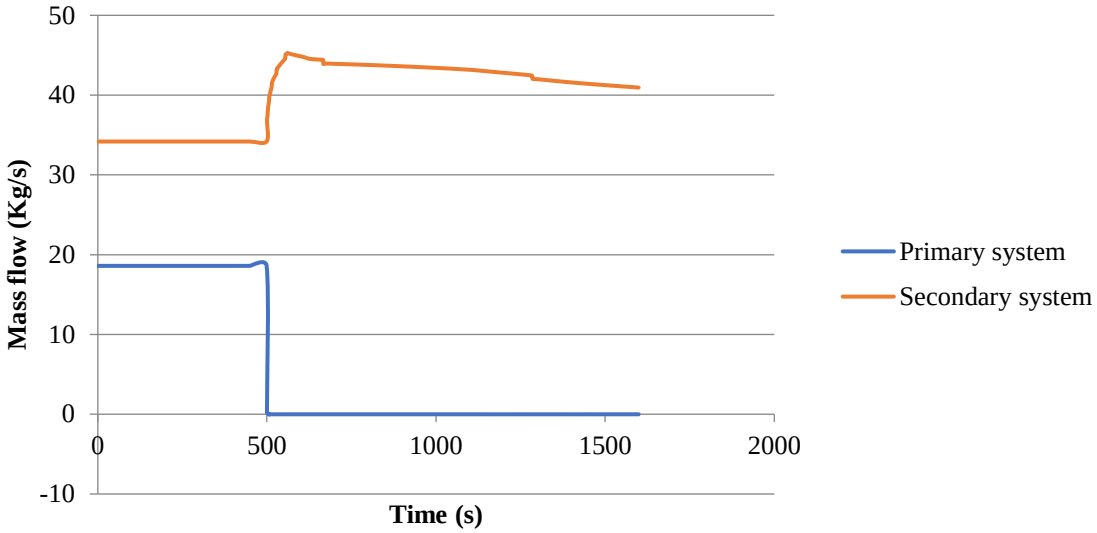

Figure 7.41 Transient mass flow rates for Case 5

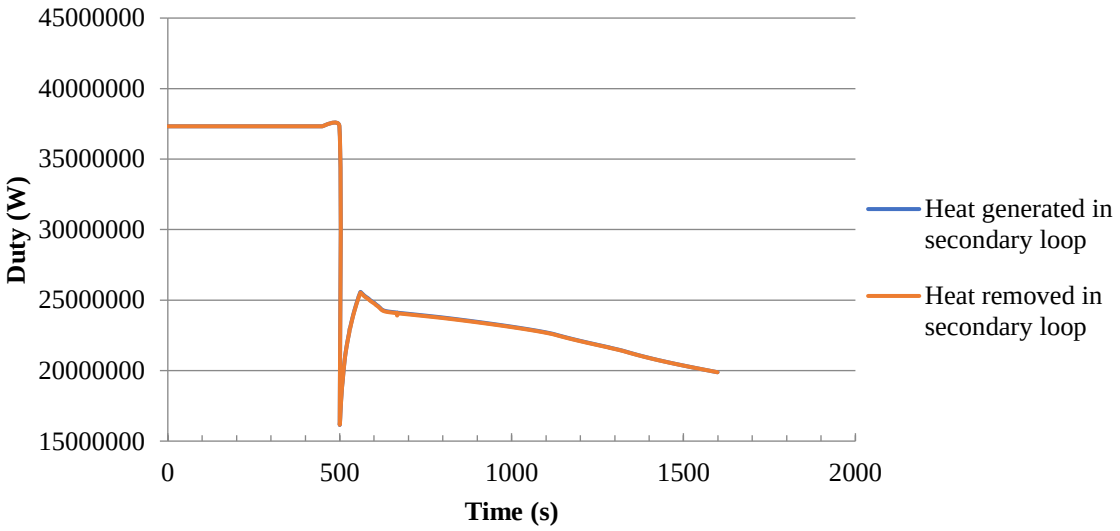

Figure 7.42 Comparison of heat source and heat sink for Case 5

7.8 Conclusions

The secondary system in the Pewee design was designed and tested using RELAP5. This secondary system keeps the moderator cool during normal operation and acts as a passive decay heat removal system in an emergency situation such as a LOFA. The design assumes the radiator consists of several tubes rather than just a single pipe. The dimensions of the tie rod tubes were left unchanged, whereas the dimensions of the radiator tubes were increased. In particular, the heat transfer surface area of the radiator was increased each time. At minimum, the radiator tubes must

have twice the heat transfer surface area as the tie rod tubes. This is necessary to keep the tie rod temperatures less than 1073.15 K (melting point of zirconium hydride) and also have a decent flow rate through the secondary system. Upon receiving the steady-state results, a LOFA transient was run by cutting off the mass flow rate of the propellant. Then, the reactor was scrammed. The results show that the secondary system is able to remove the decay heat.

CHAPTER 8: FINAL CONCLUSIONS

In this dissertation, the following work was done: (i) modeling the Pewee Test Reactor in RELAP5 for a steady-state representation, (ii) modeling corrosion-induced blockages and their impact on radiation heat transfer in the Pewee core, (iii) modeling LOFA and their impact on radiation heat transfer in the Pewee core, and (iv) design and testing of a passive decay heat removal loop for the Pewee that operates in response to a LOFA. For part (i), the RELAP5 model of the Pewee was tuned using the conduction models and by adjusting the fouling factors in order to best match the temperature profile provided in the literature. Similarly, the pressure profile was tuned by adjusting the roughness coefficients and the Reynolds forward/reverse loss coefficients. For part (ii), corrosion-induced blockages were assumed to occur at the inlet of the coolant channels of the peripheral fuel elements. While the blockages caused the temperature change in the blocked channels to increase, the radiation heat transfer between the blocked channels and the cold surfaces increased. At the same time, the radiation heat transfer between the unblocked channels and the cold surfaces decreased. In general, more corrosion corresponds to greater emissivity, which yields higher radiation heat transfer rates. For part (iii), a partial or complete LOFA causes the temperature of the fuel elements to become greater than normal, and in some cases, exceed the melting point of UC. In general, reducing the flow rate through the rocket system increases the radiation heat transfer rate in the core. However, results show that a complete LOFA causes the radiation heat transfer rate to decrease. In such a situation, it is the peripheral coolant channels that handle the majority of the radiation heat transfer. For part (iv), the passive decay removal loop is able to remove the decay heat in response to a LOFA. During both steady-state and post-LOFA operation of the secondary system, the tie rod temperatures are kept below the melting points. Natural circulation is also achieved in the secondary system. Further work could involve performing normal start-up and shut-down transients on the Pewee rocket with secondary system using RELAP5. In addition, research could be focused on studying nuclear rocket fuels

REFERENCES

1. Akyuzlu, K. M. (2015). Numerical Study of High-Temperature and High-Velocity Gaseous Hydrogen Flow in a Cooling Channel of a Nuclear Thermal Rocket Core. *Journal of Nuclear Engineering and Radiation Science, 1*(4), 041006. from https://nuclearengineering.asmedigitalcollection.asme.org/data/journals/ajneb7/934493/ners_1_4_041006.pdf
2. Akyuzlu, K. M., & Coote, D. (2013). Numerical Simulations of Thermal Hydrodynamic Transients in the Cooling Channels of a Nuclear Thermal Propulsion Engine. In *49th AIAA Jet Propulsion Conference*.
3. AZO Materials. (2016). Zirconium Carbide. Retrieved August 27, 2016, from AZO Materials website: http://www.azom.com/properties.aspx?ArticleID=261
4. Borowski, S. K., McCurdy, D. R., & Packard, T. W. (2012). Nuclear Thermal Propulsion (NTP): A Proven Growth Technology for Human NEO/Mars Exploration Missions. In *Aerospace Conference, 2012 IEEE* (pp. 1-20). IEEE.
5. Borowski, S. K., McCurdy, D. R., & Packard, T. W. (2009, June). Nuclear Thermal Rocket/Vehicle Characteristics and Sensitivity Trades for NASA's Mars Design Reference Architecture (DRA) 5.0 study. In *Proceedings of Nuclear and Emerging Technologies for Space 2009*.
6. Buden, D. (1970). Operational Characteristics of Nuclear Rockets. *Journal of Spacecraft and Rockets, 7*(7), 832-836
7. Bugby, D. C., Cepeda-Rizo, J., & Rodriguez, J. I. (2011). Thermal switching cryogenic heat pipe. Georgia Institute of Technology.
8. Christie, R. J., & Plachta, D. W. (2006, January). Zero Boil-Off System Design and Thermal Analysis of the Bimodal Thermal Nuclear Rocket. In M. S. El-Genk (Ed.), *AIP Conference Proceedings* (Vol. 813, No. 1, pp. 494-501). AIP.
9. CIRCOR Aerospace. (2017.). Check valves. Retrieved April 1, 2017, from CIRCOR Aerospace website: http://www.circoraerospace.com/products-check-valves.asp
10. Damerval, F., & Durkee, W. (1970). Nuclear Rocket Experimental Engine Test Results. *Journal of Spacecraft and Rockets,* 7(12), 1397-1402

11. De Grandis, S., Finzi, E., Lombardi, C., Mandelli, D., Padovani, E., Passoni, M., ... & Summerer, L. A feasibility study of an integral PWR for space applications. In *Proceedings of the ICAPP* (Vol. 4). from http://s3.amazonaws.com/academia.edu.documents/3427049/ACT-RPR-NRG-2004-IACPP-Feasibility_of_PWR_for_Space_Applications.pdf?AWSAccessKeyId=AKIAIWOWYYGZ2Y53UL3A&Expires=1491514477&Signature=796A0DcRlsS2i6XxzoBiEmyDMJI%3D&response-content-disposition=inline%3B%20filename%3DA_feasibility_study_of_an_integral_PWR_f.pdf
12. El-Genk, M. S., Liscum-Powell, J., & Pelaccio, D. G. (1994, July). Bimodal, low power pellet bed reactor system design concept. In M. S. El-Genk, & M. D. Hoover (Eds.), *AIP Conference Proceedings* (Vol. 301, No. 1, pp. 1535-1548). AIP.
13. El-Genk, M. S., & Tournier, J. M. (2004, February). Conceptual Design of HP-STMCs Space Reactor Power System for 110 kWe. In M. S. El-Genk, & M. J. Bragg (Eds.), *AIP Conference Proceedings* (Vol. 699, No. 1, pp. 658-672). AIP.
14. Elliot, J. O., Lipinski, R. J., & Poston, D. I. (2003). Design concept for a nuclear reactor-powered Mars Rover.
15. Entegris. (2013). Properties and Characteristics of Graphite. Retrieved August 27, 2016, from Entegris website: https://www.entegris.com/resources/assets/6205-7329-0513.pdf
16. Finseth, J. (1991). Overview of Rover Engine Tests. *Final Report, Sverdrup Corporation for NASA MSFC*.
17. Finzi, E., Lombardi, C. V., & Summerer, L. (2007). An integrated PWR for planetary exploration. In *Proceedings of the ICAPP* (Vol. 7). http://www.esa.int/gsp/ACT/doc/POW/ACT-RPR-NRG-2007-FinziLombardiSummerer-ICAPP07-An-Integrated-PWR-for-planetary-exploration-7012.pdf
18. Fishbine, B., Hanrahan, R., Howe, S., Malenfant, R., Scherer, C., Sheinberg, H., & Ramos, O. (2014.). Nuclear Rockets: To Mars and Beyond. Retrieved December 19, 2014, from http://www.lanl.gov/science/NSS/issue1_2011/story4full.shtml
19. Fittje, J., & Schnitzler, B. (2008, July). Evaluation of Recent Upgrades to the NESS (Nuclear Engine System Simulation) Code. In *44th AIAA/ASME/SAE/ASEE Joint Propulsion Conference & Exhibit* (p. 4951). from https://ntrs.nasa.gov/archive/nasa/casi.ntrs.nasa.gov/20090004441.pdf
20. Gunn, S. (2001). Nuclear Propulsion—A Historical Perspective. *Space Policy*, 17(4), 291-298.

21. Glasstone, S., & Sesonske, A. (1994). Nuclear Reactor Engineering: Reactor Design Basics. Volume One.
22. Glasstone, S., & Sesonske, A. (2010). *Nuclear reactor engineering: Reactor systems engineering*. (3rd ed., pp. 78). XanEdu Publishing, Inc.
23. Grabke, H. J., Krajak, R., & Muller-Lorenz, E. M. (1993). Metal Dusting of High Temperature Alloys. *Werkstoffe und Korrosion*. 44. 89-97
24. Hall, M. L., & Doster, J. M. (1986). Transient modeling of the thermohydraulic behavior of high temperature heat pipes for space reactor applications.
25. Heath, B. K., & Aydogan, F. (2016). Radiation Heat Transfer in the Fuel of a Nuclear Rocket. *Journal of Thermal Engineering*. 2 (2). 786-793
26. Houts, M. (2014). Space Fission Power and Propulsion. Retrieved January 30, 2017, from https://ntrs.nasa.gov/archive/nasa/casi.ntrs.nasa.gov/20150002600.pdf
27. Houts, M., Van Dyke, M., Godfroy, T., Martin, J., Bragg-Sitton, S., Dickens, R., ... & Carter, R. (2003, January). Hardware Based Technology Assessment in Support of Near-Term Space Fission Missions. In *AIP Conference Proceedings* (Vol. 654, No. 1, pp. 784-789). AIP.
28. Iuchi, T., Furukawa, T., & Wada, S. (2003). Emissivity Modeling of Metals during the Growth of Oxide Film and Comparison of the Model with Experimental Results. *Applied Optics*. 42 (13). 2317-2326
29. Johnson, M. (2006). The Misunderstood check valve. *Valve Magazine*, 28-34
30. Jones, R. W., & Crosthwaite, J. L. (1973). Uranium Carbide Fuel for Organic Cooled Reactors. *Atomic Energy of Canada Limited, Report AECL-4443*.
31. Kruger, G. (1991). A Cermet Fuel Reactor for Nuclear Thermal Propulsion (Rep. No. N92-11096).
32. Lienhard, J. H., VI, & Lienhard, J. H., V. (2016). *A Heat Transfer Textbook* (4th ed.). Cambridge, MA: Phlogiston Press.
33. Los Alamos National Laboratory. (1969). Pewee I Reactor Test Report (pp. 1-122, Rep. No. LA-4217-MS)
34. Malloy III, J. D. (1994). *U.S. Patent No. 5,329,564*. Washington, DC: U.S. Patent and Trademark Office.
35. Mock, P. R., Marcus, D. B., & Edelman, E. A. (1975). Communications Technology Satellite: a variable conductance heat pipe application. *Journal of Spacecraft and Rockets*, *12*(12), 750-753.

36. Morley, N. J., & El-Genk, M. S. (1992, January). Passive decay heat removal in the PeBR concept for nuclear thermal propulsion. In *AIP Conference Proceedings* (Vol. 246, No. 1, pp. 955-966). AIP.
37. Nam, S. H., Venneri, P., Kim, Y., Lee, J. I., Chang, S. H., & Jeong, Y. H. (2015). Innovative Concept for an Ultra-Small Nuclear Thermal Rocket Utilizing a New Moderated Reactor. *Nuclear Engineering and Technology*, *47*(6), 678-699.
38. NASA. (2016, November 1). Space Flight System Glenn Research System. Retrieved April 26, 2017, from https://spaceflightsystems.grc.nasa.gov/
39. NASA Jet Propulsion Laboratory. (ND). Ion Propulsion. Retrieved April 26, 2017, from https://dawn.jpl.nasa.gov/mission/ion_prop.asp/
40. Pelaccio, D. G., El-Genk, M. S., & Butt, D. P. (1994). A Review of Carbide Fuel Corrosion for Nuclear Thermal Propulsion Applications. In *Space Nuclear Power and Propulsion: Eleventh Symposium* (Vol. 301, No. 1, pp. 905-918). AIP Publishing
41. Peoples, J. A. (1970). Malfunction Analysis of a Conceptual Space Power Fast-Spectrum Reactor (No. N--71-12568; NASA-TM-X--2057; E--5690). National Aeronautics and Space Administration, Cleveland, Ohio. Lewis Research Center
42. Robbins, W.H., & Finger, H.B. (1991). An Historical Perspective of the NERVA Nuclear Rocket Engine Technology Program (Rep. No. AIAA-91-3451). Brook Park, Ohio: NASA Lewis Research Center. from https://ntrs.nasa.gov/archive/nasa/casi.ntrs.nasa.gov/19910017902.pdf
43. Russon, M. (2015). NASA Cutting Mars Travel Time in Half Using Solar-Electric Engines and Nuclear Rockets. *International Business Times*. Retrieved August 27, 2016, from http://www.ibtimes.co.uk/nasa-cutting-mars-travel-time-half-using-solar-electric-engines-nuclear-rockets-1504450
44. Schmidt, E., Lazareth, O., & Ludewig, H. (1993, January). Kinetic—a system code for analyzing nuclear thermal propulsion rocket engine transients. In M. S. El-Genk, & M. D. Hoover (Eds.), *AIP Conference Proceedings* (Vol. 271, No. 3, pp. 1303-1308). AIP. from http://aip.scitation.org/doi/pdf/10.1063/1.43091
45. Schweitzer, P. A. (2009). Fundamentals of Corrosion: Mechanisms, Causes, and Preventative Methods. CRC Press.
46. Seo, S. K., Roh, J. S., Kim, E. S., Chi, S. H., Kim, S. H., & Lee, S. W. (2009). Thermal Emissivity of Nuclear Graphite as a Function of Its Oxidation Degree (1)-Effects of Density, Porosity, and Microstructure. *Carbon letters*, *10*(3), 225-229

47. Shukla, K. N. (2015). Heat Pipe for Aerospace Applications—An Overview. *Journal of Electronics Cooling and Thermal Control*, *5*(01), 1.
48. Simmons, C. R. (1969). Performance of WANL Supplied Fuel Elements in PEWEE-1 (No. WANL-TME--1937). Westinghouse Electric Corp., Pittsburgh, Pa.(USA). Astronuclear Lab
49. Summerer, L., & Stephenson, K. (2011). Nuclear Power Sources: a Key Enabling Technology for Planetary Exploration. *Proceedings of the Institution of Mechanical Engineers, Part G: Journal of Aerospace Engineering*, *225*(2), 129-143.
50. Todreas, N. E., & Kazimi, M. S. (2012). Nuclear Systems Volume 1: Thermal Hydraulic Fundamentals. Boca Raton, Florida: CRC Press
51. Turney, G. E., Kieffer, A. W., & Petrik, E. J. (1971). Operating Characteristics of the Primary Flow Loop of a Conceptual Nuclear Brayton Space Power Plant(No. N--71-18866; NASA-TM-X--2161). National Aeronautics and Space Administration, Cleveland, Ohio. Lewis Research Center
52. Valcor Engineering Corporation. (2017.). Aerospace check valves. Retrieved April 1, 2017, from Valcor Engineering Corporation website: http://www.valcor.com/missiles-and-aerospace/aerospace-check-valves/
53. Walker, K. L., Tarau, C., & Anderson, W. G. (2013). Alkali metal heat pipes for space fission power. *Nuclear and Emerging Technologies for Space (NETS-2013), Albuquerque, NM*.
54. Was, G. S. (2007). Fundamentals of Radiation Materials Science: Metals and Alloys. Springer.
55. Wright, S. A., Lipinski, R. J., Pandya, T., & Peters, C. (2005, February). Proposed design and operation of a heat pipe reactor using the Sandia National Laboratories annular core test facility and existing UZrH fuel pins. In *AIP Conference Proceedings* (Vol. 746, No. 1, pp. 449-460). AIP.
56. Woydt, M., & Mohrbacher, H. (2014). The Tribological and Mechanical Properties of Niobium Carbides (NbC) Bonded with Cobalt or Fe3Al. *Wear*, *321*, 1-7
57. Zolfagharifard, E. (2016). NASA Wants to Use Nuclear Rockets to Get to Mars. *Daily Mail*. Retrieved November 1, 2016, from http://www.dailymail.co.uk/sciencetech/article-3499441/Nasa-wants-use-nuclear-rockets-Mars-Space-agency-claims-technique-effective-way-reaching-red-planet.html